Effect of Pretreatment on Metal Dispersion in Carbon and Oxide Supported Catalysts

BY

MANUEL A. NIETO
B.S., University of Houston, 2002

THESIS

Submitted as partial fulfillment of the requirements
for the degree of Master of Science in Chemical Engineering
in the Graduate College of the
University of Illinois at Chicago, 2012

Chicago, Illinois

Defense Committee:

John Regalbuto, Chair and Advisor
Randall Meyer
Ke-Bin Low

ACKNOWLEDGEMENTS

This thesis is hardly the work of a single person; it is merely a compilation of the valuable contributions of numerous people, each of whom played a fundamental role in making this research possible. I would like to first and foremost thank my research advisor Dr. John Regalbuto for his valuable instruction, guidance, and encouragement. I truly feel honored to have worked with him.

I am particularly grateful for the assistance given by my students Jeff Tyska, Helena Bliss, Rami Qafisheh, Brian Mottel, Alex Magarychev, Bryan Isles, Chris Starrick, Eleftherios (Larry) Avtzis and Mariam Buari, who through several semesters of research helped me with innumerable hours of work on experimentation and XRD data acquisition, as well as dedication to counting tenths of thousands of particles from STEM images.

I would like to offer my special thanks to Dr. Ke-Bin Low and Dr. Alan Nicholls from the UIC Research and Resources Center for their instruction, patience and continuous help in STEM imaging.

I wish to express my appreciation to all my colleagues and ex-colleagues at the department of chemical engineering for their teachings, support and friendship.

Finally, yet importantly, I would like to express my heartfelt thanks to my family and friends back home for their constant support through the duration of my studies.

MAN

TABLE OF CONTENTS

LIST OF TABLES

LIST OF TABLES (continued)

LIST OF FIGURES

LIST OF FIGURES (continued)

LIST OF FIGURES (continued)

LIST OF ABBREVIATIONS

CI	Clustering Index
CPA	Chloroplatinic Acid
DI	Dry Impregnation
EM	Electron Microscopy
EXAFS	Extended X-Ray Absorption Fine Structure
FCC	Face Centered Cubic
FTIR	Fourier Transform Infra-Red
GLC	Gas-Liquid Chromatography
HAADF	High-Angle Annular Dark Field
HRTEM	High Resolution Transmission Electron Microscopy
IW	Incipient Wetness
OR	Ostwald Ripening
PdTA	Palladium Tetraammine
PdTC	Palladium Tetrachloride
PMC	Particle Migration and Coalescence
PTA	Platinum Tetraammine
PZC	Point of Zero Charge
SEA	Strong Electrostatic Adsorption
SEM	Scanning Electron Microscopy
STEM	Scanning Transmission Electron Microscopy
STM	Scanning Tunneling Microscopy
TEM	Transmission Electron Microscopy

LIST OF ABBREVIATIONS (continued)

TPR	Temperature Programmed Reduction
WI	Wet Impregnation
XANES	X-Ray Absorption Near Edge Spectroscopy
XPS	X-Ray Photoelectron Spectroscopy
XRD	X-Ray Diffraction

SUMMARY

The purpose of this thesis is to determine the influence that pretreatment conditions have over the metal particle size of heterogeneous catalysts. Since the gas phase reacts with the metal atoms at the surface of the particles, a high level of dispersion is critical to maximize the amount of surface atoms. The correlation between pretreatment conditions and metal particle size has been indirectly investigated by various studies, but hasn't been systematically examined.

Chapter 1 provides a brief introduction to the purposes and importance of this research. Important theoretical concepts about the preparation of catalysts and pretreatment methods, sintering mechanisms, the utilized characterization methods (XRD and STEM), and a literature review are revised in **Chapter 2**

The design of the experimentation is explained in **Chapter 3.** The metals selected for this research are platinum and palladium. The catalysts where prepared by two methods, dry impregnation and strong electrostatic adsorption. The metals where deposited on three low-PZC supports: oxidized carbon, silica, and titania; and two high-PZC supports: alumina and carbon. The catalysts were reduced in continuous flow of hydrogen gas with heating rates of 0.5^{o}C/min, 2.5^{o}C/min and 5.0^{o}C/min and final reduction temperatures of 200^{o}C and 500^{o}C. In additional trials, helium was introduced into the hydrogen stream to test the influence of increased evacuation of gases produced during reduction. For another trial, the hydrogen was bubbled through water to introduce water vapor into the stream and examine the influence of humidity over metal sintering.

The results together with the discussion are thoroughly explained in **Chapter 4**. The analysis for each catalyst system is exhibited individually by support. The general conclusions for these results are presented in **Chapter 5** together with recommendations for future work.

Humidity showed to be the most important metal particles sintering factor, especially for catalysts prepared by DI. Particle size distributions show how PMC is the main sintering mechanism taking place, particularly for the samples with low levels of dispersion. Additional results from STEM imaging however show evidence that the OR sintering mechanism must be happening as well. General results show low levels of dispersion for most of the DI prepared catalysts. Higher reduction temperatures and heating rates, as well as the presence of water vapor, promoted particle sintering. Finally, moderate heating rates showed to yield slightly smaller average particle sizes than high or low heating rates.

The possibility of seeing individual metal atoms along the support's surface in the new STEM instrument opened new doors for, in the future, determining the exact sintering behavior of metal particles.

1. INTRODUCTION

It is estimated about 90% of all chemical products manufactured worldwide comprise at least one catalytic process. Hence, the importance of catalysts in people's everyday activities cannot be undermined. Catalysts take part in almost everything, from the manufacture of food and clothing, to the production of fuels for cars and machinery, making all these practices cleaner and more efficient. They make chemical processes require less energy input, and play a crucial role in pollution control by minimizing the production of waste and undesired byproducts. Most wonderful is one of catalysts' basic properties; they remain unconsumed at the end of the chemical reaction they were used for, ready to be used again and again, which makes them immensely more beneficial. The ideal use assigned to the wide variety of catalysts available is determined by certain characteristics, like their physical phase, mechanical and chemical properties, selectivity, stability, regeneration, and cost, to name a few [1].

Typical heterogeneous catalysts (where the reactants are found in a different phase than the catalyst) consist of a transition metal supported on an inert, porous material. These catalysts are very widely used because the reaction products can easily be separated from the catalyst. Through a variety of preparation methods, the catalyst is impregnated into the support in the form of small particles. The reaction of a gaseous phase with a solid metal catalyst can only occur on the metal atoms exposed to the reactant gases. These atoms are at the surface of the particle only. This means that of any given particle the atoms on the center remain shielded from the gaseous phase. Based on this premise, and noting that metal catalysts are quite expensive, it is easy to conclude that in order to maximize the number of atoms exposed for reaction the metal particles deposited on the support must be as small as possible [2]. As a

general benchmark, metal particles measuring 1 nm in diameter are considered to have all of their atoms exposed and accessible for chemical reactions [3].

The size of the catalyst particles is determined, among other things, by its preparation method and pretreatment conditions. After the metal precursor has been adsorbed or impregnated onto the support, the catalyst must be reduced under a flow of H_2 gas under certain heating conditions. It is these pretreatment conditions which play a huge role on the extent of sintering which tends to affect the final effectiveness of the catalyst [2].

The metal catalysts chosen for this thesis are platinum and palladium, not only because of their similar reductive potential, but also because of the wide use they are given in a great variety of industrial processes like: hydrogen-deuterium exchange, hydrogenation of alkenes, hydrogenation of aromatics, deuterium-aromatic exchange, skeletal isomerization of hydrocarbons, hydrogenolysis of C-O bonds, hydrogenation of carbonyl group, hydrogenation of nitrogen oxides, ammonia decomposition, dehydrogenation of hydrocarbons, decomposition of formic acid, oxidation of hydrogen, oxidation of carbon monoxide, oxidation of ammonia, oxidation of sulfur dioxide, oxidation of alcohols, oxidation of aldehydes and oxidation of methane with steam [11].

Even though some researchers have indirectly touched this subject, the effect of pretreatment conditions on metal particle size sintering has never been systematically examined. *This thesis deals with surveying the influence that temperature, heating rate, and humidity, during pretreatment reduction, have on platinum and palladium particle size deposited onto a variety of supports: carbon, alumina, silica and titania.* The supports where chosen based on their assorted surface areas and surface electrostatic characteristics.

2. THEORETICAL BACKGROUND

2.1 Catalyst Preparation

Even though there are a wide variety of preparation methods that have been developed by a very diverse and demanding industry, three methods still predominate as the most important and extensively used: impregnation, adsorption and precipitation. For this research, catalysts will be synthesized by impregnation and adsorption. Preparation is then followed by drying, calcination (not always necessary), and the very important process of reduction, which has pronounced influence over the final metal particle size [4].

2.1.1 Impregnation

Impregnation is arguably the simplest and least expensive catalyst preparation method. The metal precursor solution is diluted in a water volume equal to the support's pore volume. The solution is added drop-wise with constant mixing until the pore volume of the support is filled with liquid. The resulting slurry needs to be dried to obtain the support impregnated with metal precursor. This method is known as dry impregnation (DI) or incipient wetness (IW). This technique is very simple since no attention has to be paid to the pH of the solution, no precursor is wasted in any kind of filtering, and very accurate metal loadings can be achieved [3]. It is, nonetheless, also a very "rough" technique. Despite the best efforts on the use of this method, it is very hard to get an even distribution of the metal precursor throughout the whole support. Also, the metal precursor doesn't have a strong interaction with the support sites. For these reasons, the later calcination or reduction procedures generally yield very mobile metal complexes which tend to sinter and hence, increase particle size. This implies that important quantities of the metal catalyst are being wasted.

There are other types of impregnations, called "wet" impregnations (WI). Here the precursor solution considerably exceeds the pore volume of the support. The amount of solution added depends on the surface area of the support and a parameter defined by the user, the surface loading (SL), which is a measure how much support's surface area is exposed to a unit of solution volume; hence its units are m^2/L. The terms are related by the following equation:

$$SurfaceLoading\left[m^2/L\right] = \frac{MassOfSupport[g] \times SurfaceArea\left[m^2/g\right]}{VolumeOfSolution[L]} \qquad (2.1)$$

High surface loading values (low volume of solution) implies the system is approaching dry impregnation conditions. The advantage of this method is a very homogeneous distribution of the metal precursor along the support's surface can be achieved [5]. On the other hand, it's unfavorable that a filtering process is required, where some precursor in the solution might get wasted. Therefore, it's hard to reach an accurate metal loading. To prevent this, continuous heating and stirring might be required to evaporate the water from the solution and ensure all metal precursor remains in the support [6]. Then again, there is no strong interaction between the precursor and the support, which will generate larger particles after the pertinent pretreatments are performed.

2.1.2 Adsorption

While adsorption is in principle an impregnation method, it is distinguished by the essence of its mechanism, which is to create a strong electrostatic interaction between the ionic metal precursor and the support's hydroxyl groups. This interaction creates a monolayer of metal precursor strongly adsorbed on the support's surface, ultimately resulting in very small particles nearing 100% dispersion.

To perform a Strong Electrostatic Adsorption (SEA), it is necessary first to find the point of zero charge (PZC) of the support. The surface of the support contains hydroxyl groups which, depending of the pH of the precursor solution they are in contact with, gain or release protons. Figure 2.1 gives a representation of this phenomenon. The pH at which the hydroxyl groups are neutral is known as the PZC [3]. At pH values above the support's PZC, the surface can absorb anionic metal precursors and the opposite is true for cationic precursors. The PZC is different for every support and it could be acidic or basic. Acidic PZC indicates an anionic surface, which is ideal to match with cationic precursors, such as platinum tetraammine (PTA) $[Pt(NH_3)_4]^{+2}$, or palladium tetraammine (PdTA) $[Pd(NH_3)_4]^{+2}$. By the same principle, a basic PZC support has a cationic surface, so it has to be matched with an anionic precursor like chloroplatinic acid (CPA) $[PtCl_6]^{-2}$ or palladium tetrachloride (PdTC) $[PdCl_4]^{-2}$.

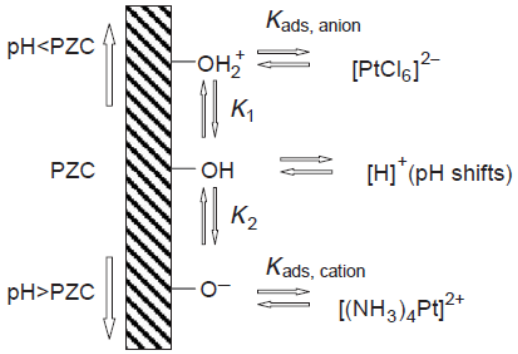

Figure 2.1 Representation of the proton exchange happening for CPA and PTA [8].

The PZC of the support can be found by plotting the pH shifts of the solution after contact with the support at high surface loadings, or even at incipient wetness [7]. The plot will reveal a buffer zone (plateau) as Figure 2.2 shows; this is the PZC of the support. With this information the support can be matched with an appropriate precursor.

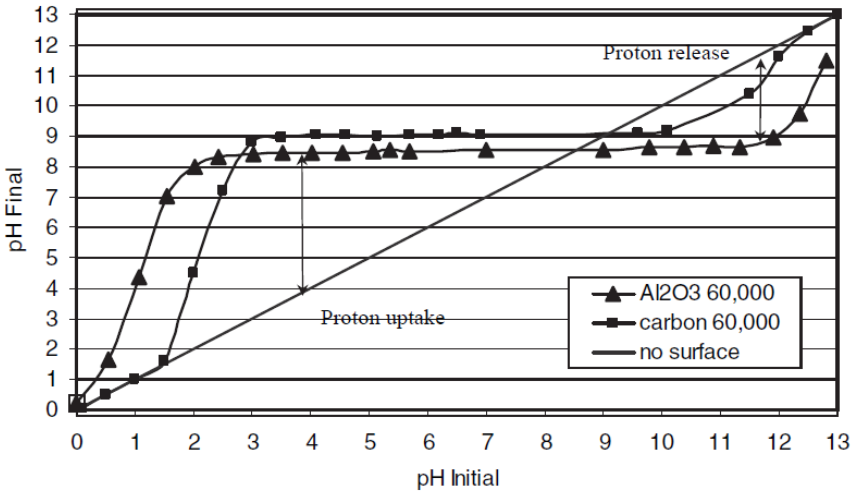

Figure 2.2 PZC determination for an alumina and a carbon support [3].

An uptake survey through various pH values, of the amount of precursor adsorbed onto the support at a desired surface loading must be completed to learn the optimum precursor solution pH as exemplified in Figure 2.3. This principle of coulombic interactions between the oppositely charged metal precursor and support's surface through varying pH values is explained by the Revised Physical Adsorption (RPA) model [9, 10]. After the support has been mixed with the precursor solution for an appropriate time, filtering and drying of the wet support is required.

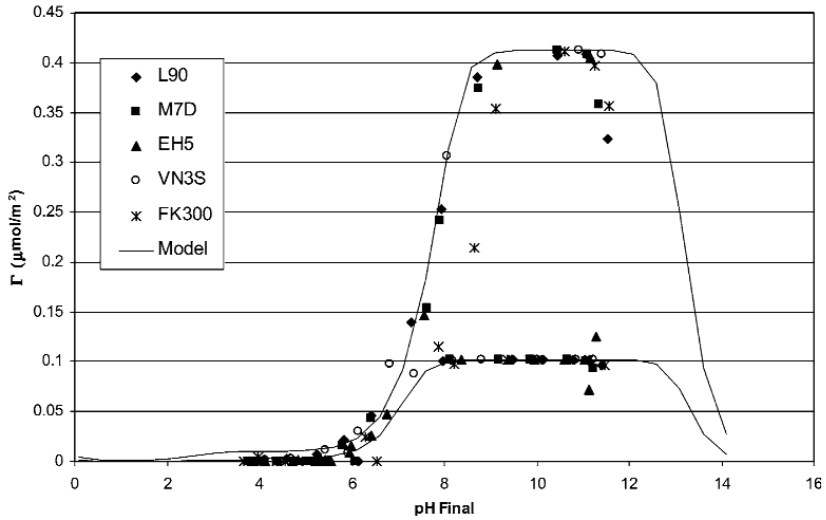

Figure 2.3 pH vs. uptake (Γ) plot for PTA on various silica supports [9].

This preparation method generally yields very high dispersions thanks to the strong interaction between the support and the metal precursor. The attraction strongly anchors the metal throughout the calcination and reduction pretreatments decreasing particle sintering [11]. Unfortunately SEA has a limit to the metal loading that can be achieved. The electrostatic attraction from the support can only deposit one monolayer of precursor onto its surface as shown in Figure 2.4. This figure also shows how the hydration sheaths around the metal set a boundary to the amount of molecules that can be positioned next to each other, limiting the maximum metal loading as well.

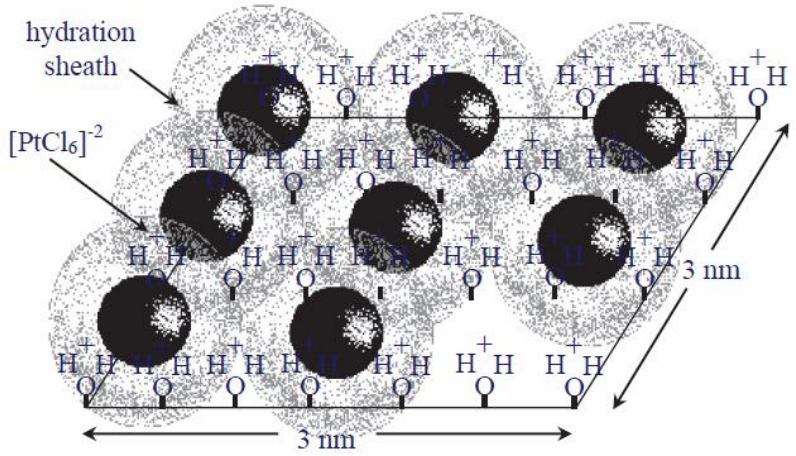

Figure 2.4 Monolayer coverage of CPA [8].

2.1.3 Reduction (Pretreatment)

The reduction stage for catalyst preparation is a critical step as it has heavy influence over the metal particle size. Incorrectly performed reductions might also prevent the catalyst from reaching metallic state. The reduction process consists of placing the dried catalyst under a steady flow of H_2 gas while heating the system at desired rate until a target temperature is reached. The sample should then be allowed to remain at this temperature for a period of time of 1 to 2 hours to ensure the entire metal is reduced and catalytically activated [12].

As temperature elevates and the metal precursor begins reducing, metal nuclei start forming during an induction period. As soon as many nuclei have accumulated, reduction proceeds rapidly as temperature escalates, which opens the window for excessive sintering [6]. For this reason, careful reduction temperatures and heating rates must be selected. Attaining a better knowledge of these pretreatment conditions is precisely one of the goals of this thesis.

Very little is known about the exact reduction mechanism. A general description for the reduction of a metal oxide MO_n is described by equation (2-2) [2]:

$$MO_n + nH_2 \rightarrow M + nH_2O \tag{2-2}$$

This equation however doesn't explain the chemistry of the reduction of more complex metal precursors like CPA or PTA and doesn't give any insight into any possible explanation for particle sintering.

Investigative work by Anderson [11] suggests a more explicit model for the reduction of PTA. Infrared spectra suggested in the case of PTA adsorbed into SiO_2 gel, when reducing the sample in H_2 at continuously increasing temperature from 47°C to 147°C, hydrogen consumption occurs simultaneously with the decomposition of the tetraammine ion. Anderson concluded that when $[Pt(NH_3)_4]^{2+}$ is reduced in hydrogen, there must exist an intermediate highly mobile species. This species must be a neutral platinum complex since if it had any kind of charge it would get electrostatically attached to the support. The following set of reactions where suggested by Dalla Betta and Boudart [13]:

$$[Pt(NH_3)_4]^{2+} + 2H_2 \rightarrow [Pt(NH_3)_2(H)_2]^o + 2NH_3 + 2H^+ \tag{2-3}$$

$$[Pt(NH_3)_2(H)_2]^o \rightarrow Pt + NH_3 + H_2 \tag{2-4}$$

The complex $[Pt(NH_3)_2(H)_2]^o$ is proposed as the species of high surface mobility. There is also a competitive set of reactions based on the direct loss of ammonia:

$$[Pt(NH_3)_4]^{2+} \rightarrow Pt^{2+} + 4NH_3 \quad (2\text{-}5)$$

$$Pt^{2+} + H_2 \rightarrow Pt + H^+ \quad (2\text{-}6)$$

In that research study it was assumed H^+ is taken up by the zeolite. Since these sets of reactions are competitive, it would seem H_2 would both fuel the creation of the mobile $[Pt(NH_3)_2(H)_2]^o$ complex through reaction (2-3), and reduced platinum through reaction (2-6). The thermodynamics of these reactions are not well understood but careful temperature control in the heating rate and final reduction temperature could likely help minimize the formation of the mobile complex. It is in this sense that through this thesis, it is intended to observe if certain heating rates and reduction temperatures yield smaller particle sizes.

Dalla Betta and Boudart also saw that for dried catalyst species, the final platinum dispersion is likewise dependent on the water vapor partial pressure during the reduction process [13]. It is plausible water might augment the mobility of Pt^{2+}, but it is more probable the effect happens before the decomposition of the tetraammine ion through the formation of another mobile neutral complex:

$$[Pt(NH_3)_4]^{2+} + 2H_2O \rightarrow [Pt(NH_3)_2(OH)_2]^o + 2NH_3 + 2H^+ \quad (2\text{-}7)$$

For this reason, in this thesis, different levels of water vapor will be added to the hydrogen stream during reduction.

Radivojevic´ et al. [14] had used thermo-gravimetric analysis (TGA) to study the decomposition of chlorine containing platinum precursors during reduction in H_2. It was found CPA reduced according to the following reaction:

$$H_2PtCl_6 \cdot H_2O + 2H_2 \rightarrow Pt + 6HCl + 6H_2O \quad (2\text{-}8)$$

Furthermore, when water vapor is a decomposition product, its speedy removal is vital for maintaining a high internal surface area in the product because of the possibility of hydrothermal sintering reactions [11].

Evidence pointing towards platinum-oxygen or platinum-chlorine complexes being mobile and tending to sinter has been found [23]. The chlorine complexes like $PtCl_x$ can be caused by poor evacuation of HCl and Cl_2 gases produced during reduction. Oxygen complexes like PtO_2 and $[Pt(OH)_4Cl_2]^{2-}$ are mostly produced when performing calcination of the sample under O_2 flow at temperatures approaching 500^oC [15].

Even less is known about the detailed chemical reactions for the reduction of palladium complexes. Since platinum and palladium have similar catalytic behaviors and the precursors used for palladium, PdTA ($[Pd(NH_3)_4]^{+2}$) and PdTC ($[PdCl_4]^{-2}$) are very similar to the platinum precursors PTA ($[Pt(NH_3)_4]^{+2}$) and CPA ($[PtCl_6]^{-2}$) respectively, it's safe to assume similar reactions and complexes take place during reduction. Similar results in sintering behavior would strengthen this assumption. Some results have been reported however, where palladium dispersion is more sensitive than platinum to temperature during reduction in H_2 [16].

2.2 Sintering Mechanisms

Theories and models have been developed to explain the sintering mechanism of catalyst metal particles but there is no concise evidence for a perfect fit to a particular theory. Historically, there had been two models which have stood-out: (i) particle migration and coalescence (Ruckenstein and Pulvermacher [17]); and (ii) emission of single atoms by small crystallites and capture of those atoms by large crystallites by Ostwald ripening (Chakraverty [18], Flynn and Wanke [19, 20], Ruckenstein and Dadyburjor [21], Lee [22]). Recently, these

models have been almost conciliated by theorizing both are possible depending on the temperature and chemical conditions the catalyst endures.

Most of these models are meant to describe the sintering process of reduced metal particles in finished catalysts, not their precursors or complexes. These mechanisms attempt to describe sintering during typical industrial and commercial processes in which catalysts participate, like automobile catalytic converters. Catalyst fouling and deactivation is a worldwide known problem after catalysts have undergone severe temperature conditions under reducing and oxidizing atmospheres for very prolonged periods of time. These sintering mechanisms will be explained in an attempt to connect them to the sintering phenomena during pretreatment reduction by analyzing the resulting metal particle size distributions, which are believed to be intimately related to these sintering models [24, 25].

Particle migration and coalescence (PMC) hypothesizes the primary mechanism of sintering is the migration of metal particles on the support and the coalescence of the particles when they come in contact with each other [26]. The speed of migration of particles is inversely proportional to its size. Furthermore, for large particles, migration can occur by effect of random metal atoms moving along the metal particle surface. If enough metal atoms migrate from one face of the particle to another, the net result would be the particle was displaced. For smaller particles (in the order of 10 atoms or less), the model states the particle must move as a whole and unperturbed unit [11].

The Ostwald ripening (OR) model states particles are immobile and sintering occurs by the migration of individual atoms from small clusters to larger clusters. The increased radius curvature of smaller particles compared to larger implies the atoms in smaller cluster's surface

have higher chemical potentials, which ultimately acts as the driving force for this atom migration theory [24].

Each sintering mechanisms model will have a distinguishing shape of the particle size distribution curve. Figure 2.5 compares the shapes for both mechanisms. The PMC model sustains particles will start merging together and smaller particles will be the first to combine since they are the most mobile, hence they disappear rapidly. As sintering advances, bigger particles start forming but are still quite uncommon since they become very immobile. For this reason the particle size distribution curve is tilted towards the left but has a thin extension to the right as bigger particles start to appear like in Figure 2.5 (a). The OR model consists of individual atom transfer from small particles to bigger ones. This infers that, as sintering progresses, the particle size distribution starts drifting towards the right. Smaller particles however continue to inevitably form because of the continuous loss of atoms some particles suffer to feed the larger ones. These small particles are represented by the long "tail" the curve shows and continues to drag along while it tilts toward bigger sizes. Figure 2.5 (b) shows a simulation of a typical OR particle size distribution.

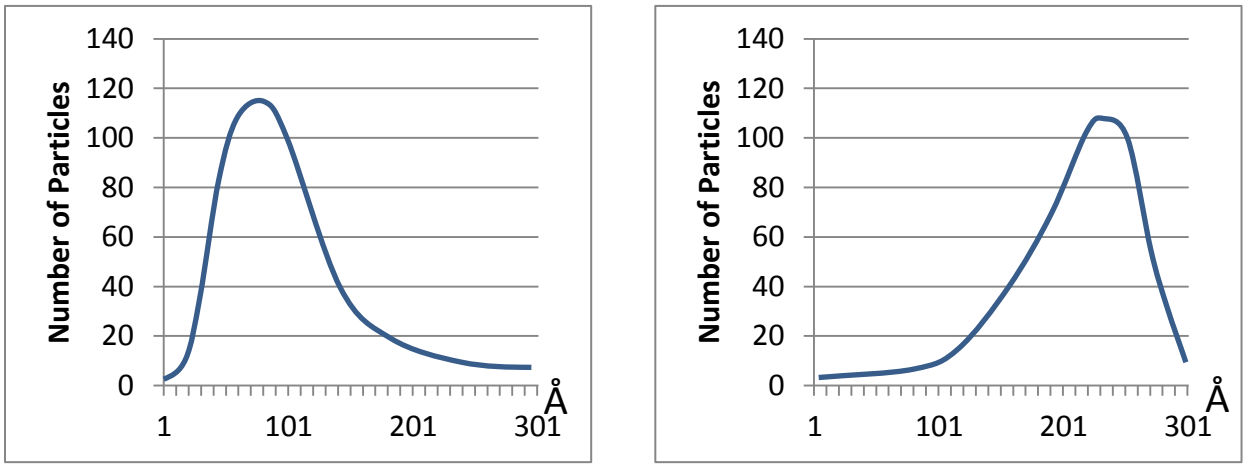

Figure 2.5 (a) Particle size distribution of the Particle Migration and Coalescence mechanism [29]. (b) Particle size distribution of the Ostwald Ripening mechanism

Detailed mathematical correlations and kinetics of the OR particle size distribution shape, given by the Lifshitz-Slyozov-Wagner theory, have been explained by Finsy [27] and Wang [28]. PMC curve obeys a log normal distribution function as explained by Stevenson [26] and Granqvist and Buhrman [25, 29].

There have been experimental limitations to determine one sintering mechanism as dominant over the other. While Granqvist and Buhrman claim PMC is a better fit for most experimental data [32], Wanke raised some objections to these conclusions [31]. Wanke argued the lack of ability to identify very small particles, under 1.5 nm in diameter by traditional TEM techniques, could hide important evidence supporting OR as the actual sintering mechanism. Also it has been argued it might take longer time than usually allowed for a system to definitely attain an OR particle size distribution shape and usually PMC is misleadingly a better fit for the initial stages of sintering. Finally, it has been widely accepted both mechanisms are possible depending on a variety of factors such as metal-support combination and interactions, surface features of the support [33], oxidizing or reducing conditions, average proximity between clusters [26], just to name a few.

In a work by Sushumna and Ruckenstein [34], a platinum on alumina catalyst was exposed to a series of heat treatment conditions in alternating hydrogen and oxygen atmospheres. The results revealed all kinds of sintering behavior: coalescence between close-by particles, migration of small (1.5 nm) and large (8 nm) particles, migration followed by coalescence, vanishing of small particles near larger particles, size reduction of large particles near smaller particles, decrease in size followed by migration (and vice versa) of particles, collision and inhibited coalescence of particles, and collision-coalescence-separation of particles. It was

suggested in this study that particles on the support perceive the presence of neighbor particles by means of interaction forces between them and migrate or release atoms towards each other.

One of the purposes of this research is attempt to match the sintering behavior of the experiments performed with one, if any, of the sintering mechanism described above. The catalyst samples were pretreated in a variety of reduction temperatures, times, and heating rates. It is not certain any particular sintering mechanism would be identified, especially since these temperatures and times are quite mild compared to the conditions used for most of the experiments these models were designed upon. Another fundamental difference is sintering experiments in this thesis initiate from unreduced samples and not commercial caliber catalysts.

2.3 Characterization Methods

After the appropriate pretreatment conditions have been applied to the catalyst samples, the particle size analysis was accomplished by two methods: X-Ray Diffraction (XRD) and Scanning Transmission Electron Microscopy (STEM).

2.3.1 X-Ray Diffraction

X-ray diffraction (XRD) is the elastic scattering of X-ray photons by atoms in a periodic lattice [2]. Because X-ray's wavelengths are in the Angstrom (Å) range, they have enough energy to penetrate solids and analyze their internal structure. When X-rays are emitted towards a catalyst surface, most of them go through un-scattered. There are certain projection angles however when X-rays hit a crystalline plane, the (111) plane for instance, from which they scatter off in an ordered constructive interference like shown if Figure 2.6. The instrument detector can sense the signals of the bounced-off X-rays, and these can be plotted versus twice the emission angle (2θ) to construct an XRD diagram such as in Figure 2.7. The peaks that are

shown correspond to the crystalline planes that are able to refract the X-rays. The location of the peaks is characteristic of the crystal structure of the metal.

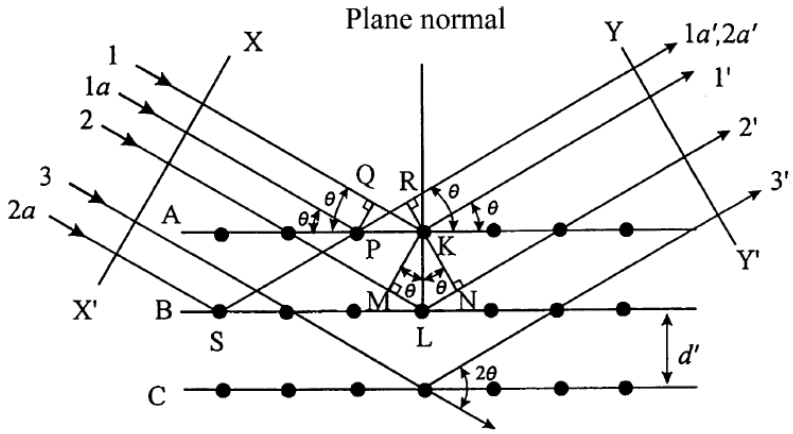

Figure 2.6 Schematic diagram of diffraction of X-rays by a crystal [35].

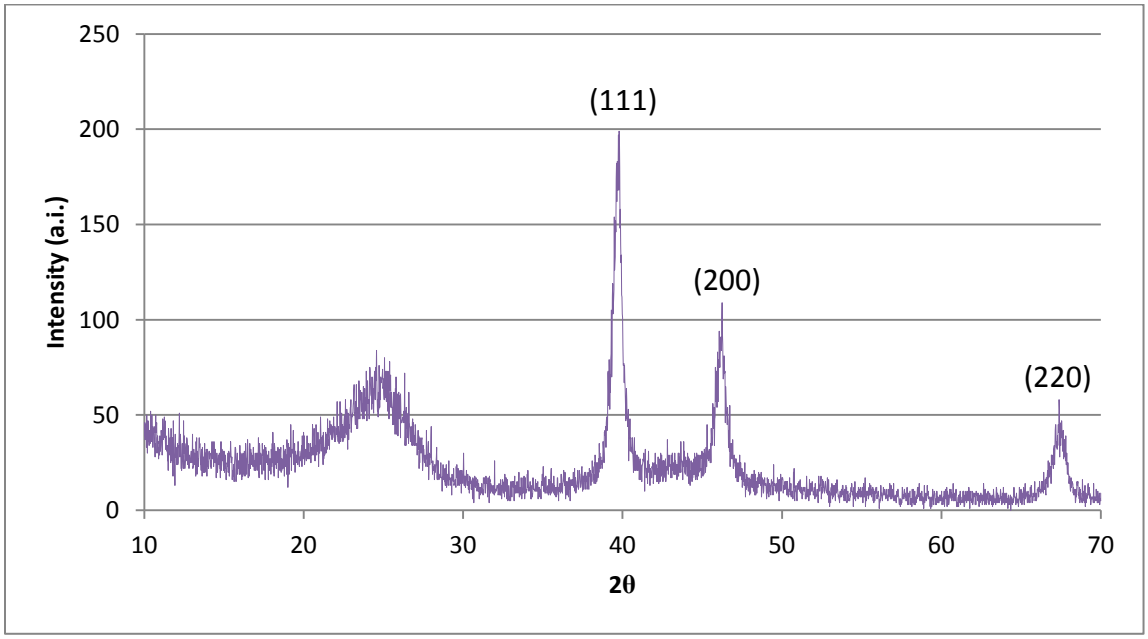

Figure 2.7 XRD diagram for platinum deposited on carbon (Vulcan XC-72).

Both metallic state platinum and palladium crystals have a Face Centered Cubic (FCC) atomic arrangement. The angle θ where a peak is expected to be found for a certain plane (*hkl*) in cubic atomic arrangements can be calculated by the following equation:

$$\frac{\sin^2\theta}{(h^2+k^2+l^2)} = \frac{\lambda^2}{4a^2} \qquad (2.9)$$

Where θ is the expected location of the peak (2θ in the XRD diagram), *h k l* are integers corresponding to the crystalline plane (*hkl*), λ is the wavelength of the X-ray source, and *a* is the lattice constant of the metal atoms (3.92 Å for platinum, 3.89 Å for palladium). One of the most common X-ray sources is Cu Kα. For this thesis the XRD instrument used has a Cu Kα wavelength of 1.541 Å.

In the 2θ range of 10^o to 70^o, three characteristic planes for FCC lattices show peaks: the (111), (200) and (220) planes at the 39.80^o, 46.28^o and 67.53^o 2θ degree locations respectively for platinum, and at the 40.12^o, 46.66^o and 68.12^o 2θ degree locations respectively for palladium. The width and location of each peak, when related to its specific plane, can provide the average diameter of the metal particles in the sample. The Scherrer formula relates crystal size to the width of the peaks:

$$t = \frac{K\lambda}{B \cos \theta_B} \tag{2.10}$$

Where *t* is the average crystal particle diameter, λ is the X-ray wavelength, *B* is the peak width in radians at half the maximum intensity of the peak, θ_B is the position of the peak at maximum intensity, and K is a constant (often given a value between 0.9 and 1). If $2\theta_1$ and $2\theta_2$ are defined as the angles at which the peak starts and finishes (Figure 2.8), and assume θ_1 and θ_2 are very close, then θ_B can be approximated to $2\theta_B = \theta_1 + \theta_2$. Also, B can be approximated to $B = (2\theta_2 - 2\theta_1) \div 2$ as shown in Figure 2.8.

XRD can also help identify the oxidation state of the metals in the catalyst. The peaks named above are exclusive of crystal lattices formed by fully reduced platinum and palladium. If another state of these metals is found, like Pt^{+4} or Pd^{+4} for instance, it could be identified by a peak in the 2θ region of 31.5^o, which is characteristic of PtO_2 or PdO_2 crystallites.

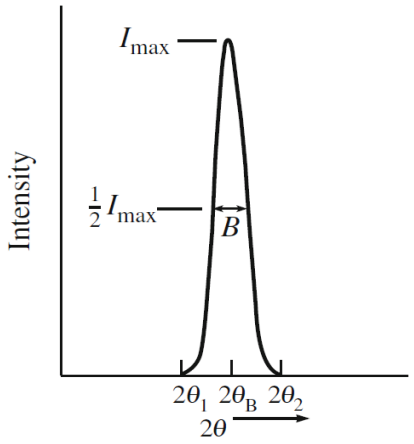

Figure 2.8 XRD peak schematic for the parameters in the Scherrer equation.

XRD is a very powerful tool to find the average particle size of metal particles in a catalyst since it is a bulk technique and large volumes of the catalyst sample can be analyzed at once. This method does have some limitations nevertheless. Only particles larger than 2 nm can be effectively identified, below this value the peaks become too wide and weak and may fade into the support's natural peaks. Another disadvantage is strong, definite XRD signals can only be attained from samples with metal loadings of approximately 2% or over. In supports with low surface areas it may be impossible to reach these loadings when preparing catalysts by SEA. Finally, XRD will only pick-up signals from the bigger particles. If a catalyst has a very wide particle size distribution, the smaller particles' signals will not be detected and the values obtained from the analysis may not be as accurate.

2.3.2 Scanning Transmission Electron Microscopy

The basic principle of Electron Microscopy consists of shooting a primary electron beam towards a sample and analyzing their interaction. Electrons can interact with atoms in the sample and emit X-rays, photons, or Auger electrons. Other types of electron beam interactions include backscattered, secondary, diffracted, loss and transmitted electrons. When all these interactions are analyzed, they provide valuable information about the sample such as imaging

of its crystal structure and morphology, oxidation states, composition, etc [3]. The field which analyzes transmitted electrons is Transmission Electron Microscopy (TEM) and it can also be operated in two more modalities, Scanning Electron Microscopy (SEM), and Scanning Transmission Electron Microscopy (STEM) which is a combination of TEM and SEM. Figure 2.9 shows a schematic set-up of these three modes.

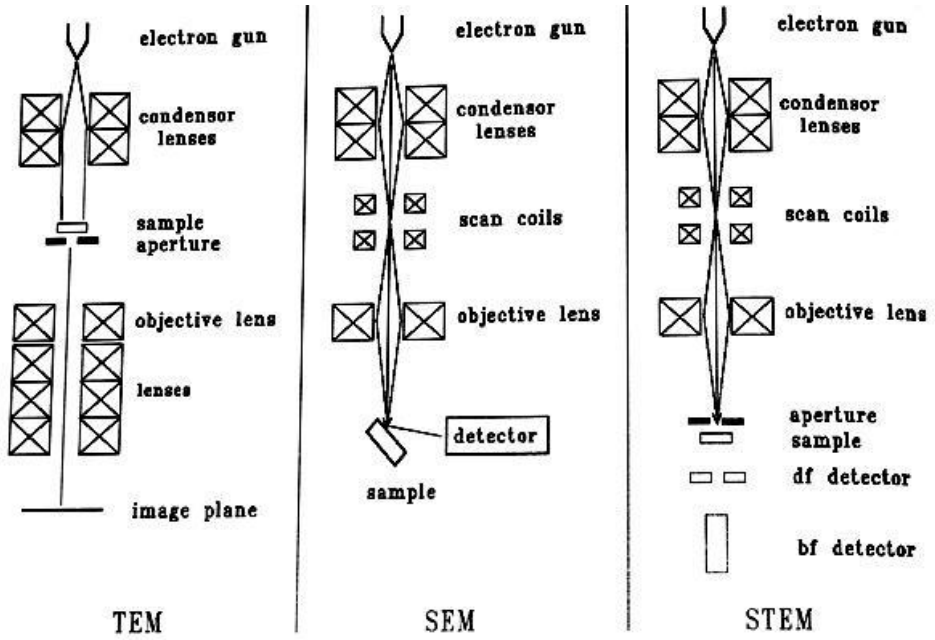

Figure 2.9 Schematic set-up of TEM, SEM and STEM electron microscopes [3].

In general, the high intensity and high energy electron beam goes through a condenser to produce parallel rays, which get attenuated by densities and thicknesses of the sample composition materials. The transmitted electrons are then magnified by the electron optics to produce a two-dimensional projection of the sample mass (bright-field image). The electron beams which get diffracted and are slightly off-angle from the transmitted beam are rendered into dark-field images.

STEM is a potent tool for viewing catalyst metal particles deposited on a support. The contrast imaging capability of a STEM can be significantly enhanced when analyzing electrons

diffracted from metal particles. Figure 2.10 schematizes the organization of the ring-shaped detectors for these annular dark-field (ADF) measurements. At higher angles, an image can be produced by the electrons scattered by heavy elements. This detection mode is called high-angle annular dark field (HAADF) or Z-contrast microscopy where the molecular weight of the analyzed species defines the brightness with which they will be shown in the rendered image.

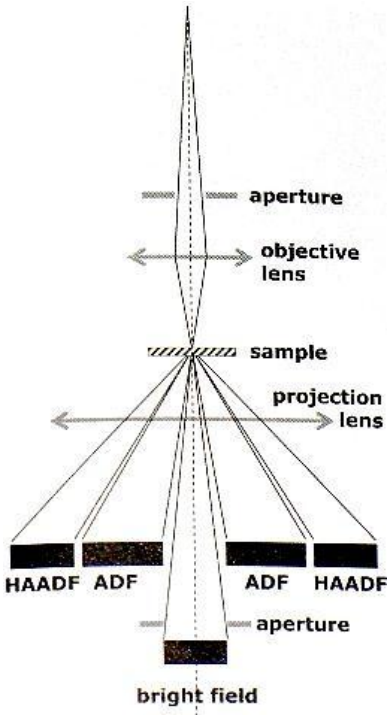

Figure 2.10 STEM outline with bright and dark field, annular dark field, and high angle annular dark field detectors [3].

The HAADF images are perfect for precise particle counting and will be used for all particle size analysis in this thesis research. There are still some weaknesses with this characterization method. Since the samples have to be scanned manually at magnifications ranging from 10,000x to 15,000,000x; the percentage of the sample actually analyzed is quite small. Therefore, it's possible many important features of the catalyst are not identified by this method. For example, while most of the sample has a homogeneous metal distribution, there could still exist few unexplored locations with severe metal agglomerates. A second weakness of STEM is

its reliance on the difference of molecular weight of the analyzed species when their molecular weights are not too different. Platinum (MW=195.1 g/mol) deposited on carbon (MW=12 g/mol) is a perfect catalyst to be analyzed by STEM since their molecular weights are a couple of orders of magnitude away and the Z-contrast is very clear. But systems like palladium (MW=106.4 g/mol) on TiO_2 (Ti MW=47.9 g/mol), where palladium MW is only about twice that of titanium, the palladium particles are barely discernible in HAADF images, especially because titania tends to have very thick particles.

2.4 Literature Review

A direct approach to the influence of heating and humidity conditions on final catalyst particle size has never been systematically examined. This subject has been touched in various studies and their results were useful in orienting some aspects of this thesis research. Table 2.1 is a comprehensive literature review of the various studies that dealt with the influence heat treatments under various reductive, oxidizing, or humid, atmospheres have on the degree of sintering of a catalyst. A fundamental distinction between "treatment" and "pretreatment" must be drawn when examining Table 2.1. Pretreatment must be understood as the treatment, or series of treatments, given to samples which have just been prepared, to reduce its precursor to metallic state bringing it to its "finished" form. Treatment is the conditions a finished catalyst is subjected to, in order to produce further sintering effects on it. The takeaway from Table 2.1 is that higher temperature and the presence of water vapor during reduction treatment or pretreatment induces metal particle sintering. Calcination of catalysts at high temperatures is commonly seen to reduce metal dispersion. Also, the literature evidences how subjecting the catalyst to more than one, or very long, treatment processes induces the loss of dispersion and catalytic activity.

Table 2.1 The influence of various pretreatments and treatments on metal particle size.

Ref	Metal / Precursor	Support	Production Method(s)	Treatment variables	Analysis methods	Results
36	CPA	Al_2O_3	WI	Reduction treatment temperatures in H_2	Pulse hydrogenolysis of methylcyclopentane	At higher reduction temperature, catalyst has lower activity because of surface morphology change.
					Chemisorption	
37	CPA PTA	Carbon	WI	Reduction treatment temperatures	XRD	At higher oxygen content of support, lower dispersion.
			Colloidal	Chemical reduction	XANES	
				Support's surface area	XPS	At higher support's surface areas, smaller Pt particle diameters.
				Pt loading	EXAFS	
				Activation temperature	HRTEM	At higher synthesis temperature for the alcohol reduction method, smaller particle sizes.
					STM	
38	CPA	CeO2	Cocombustion	Oxidation-reduction pretreatment	Infrared	Preoxidized-reduced pretreatment yields bigger particle sizes.
					TPR	
				Chlorine content	HRTEM	
					XPS	
39	Pt	Al_2O_3	Pre-fabricated CK303 by Akzo Chemie B.V.	Pt loading	Pulse hydrogenolysis of n-pentane	At higher reduction temperature, the catalyst has higher hydrocracking activity and lower isomerization activity.
				Reduction treatment temperature		
				Humidity		"Driest" samples have higher hydrocracking activity. "Wettest" samples have higher isomerization activity.
40	CPA	Al_2O_3	WI	Heat treatment temps in H_2 and O_2	TEM	Slight increase in particle size with higher temperature in heat treatments.
41	CPA PTA	Al_2O_3	DI	Heat treatment temps in air and H_2	H_2 chemisorption	Increase in heat treatment temperature and time produces bigger particles and reduces H/Pt chemisorption.
					XRD	
					TEM	
42	PTA	Y zeolite	Ion-exchange	Calcination pretreatment heating rate and temperature	H_2 chemisorption	Slower heat rate during calcination yields smaller particles.
					EXAFS	
					TEM	
			DI		XRD	
43	Pt	Carbon	Pre-fabricated E-Tek Inc.	Heat treatment temperature and time	HRTEM	Higher temperature and time of heat treatment increases particle size.
					XRD	
44	Pt	Al_2O_3	Pre-fabricated Engelhard 4759	Heat pretreatment with air, water, H_2 and O_2	HRTEM	Higher temperature pre-treatment in hydrogen increases particle size.
					XRD and XPS	
					Hydrogenation of ketopantolactone	

Ref	Metal / Precursor	Support	Production Method(s)	Treatment variables	Analysis methods	Results
45	PTA	SiO_2	Impregnation	Reduction treatment temperatures in H_2	H_2 chemisorption Electron microscopy	At higher reduction temperatures, the average particle diameter increases.
46	Pt	Al_2O_3	Pre-fabricated, CK 306	Reduction treatment temperatures in H_2	Pulse hydrogenolysis of n-pentane	Conversion of n-pentane is reduced as pre-treatment temperatures increase.
47	PTA	Al_2O_3	IW	Reduction treatment temperatures in H_2	EXAFS XANES	Higher Pt-Pt coordination shells found as reduction temperatures are increased.
48	Pt	SiO_2		Reduction treatment temperatures in H_2	Hydrogenation of iso- and n-butane	Turnover frequencies are high at low pretreatment temperatures, pass through a minimum in the region of 150 to 200 C, and increase as the pretreatment temperature increases.
49	PTA	SiO_2	IW	Reduction treatment in H_2	Mass spectroscopy	Maximum desorption of H_2O and NH_3 gases is achieved at 210 C under H2 flow.
				Autoreduction treatment in Ar/He	Quick EXAFS H_2 chemisorption	Slow heating rates in autoreduction in Ar/He yields the smallest particles.
				Calcination treatment in O2	HRTEM	
50	Pt	Al_2O_3	Pre-fabricated Engelhard 4759	Cooling after treatment reduction in H_2 vs N_2	Enantioselective Hydrogenation of Ketopantolactone	Cooling in H_2 after reduction in H_2 increases enantioselectivity
				Effect of H_2O on pretreatment		Presence of water during pretreatment reduces enantioselectivity.
51	Pd	ZrO_2	Melt-spinning	Reduction treatment temperatures in H_2	XRD CO chemisorption	At higher reduction temperatures, the Pd particle size increases.
52	$Pd(NO_3)_2$	Al_2O_3	IW	Pretreatment at various gaseous environments, N_2, H_2, 1% CH_4/air, dry air, or wet air	H_2 and CO chemisorption	Samples pretreated in dry atmospheres show more active catalysts compared to wet atmospheres.
53	Pd	Carbon		Heat treatment in various N_2 and N_2/H_2 atmospheres	Heck coupling reaction of bromobenezene with styrene	Dispersion and amount of CO chemisorbed on Pd sufrace decreased with increasing treatment temperature. The higher the treatment temperature, the lower the dispersion, and hence the lower the catalytic activity in the Heck reaction.

Ref	Metal / Precursor	Support	Production Method(s)	Treatment variables	Analysis methods	Results
54	Pd	MgO	Precipitation	Production method	Gas mix conversion: 10 mmol bromobenzene, 15 mmol styrene, 12 mmol NaOAc	Catalytic activity decreases with decreasing catalyst. dispersion. In this article, increasing the reduction temperature is assumed to reduce the dispersion of the Then, increase in reduction temperature decreases catalytic activity.
		TiO_2	P25 (Degussa)	Support		
		TiO_2	sol-gel	Reduction Treatment temperatures		
		SiO_2	Areosil 200			
		ZnO	Thermal decomposition		GLC	
		Al_2O_3	Fluka AG			
		ZrO_2	Degussa			
		Carbon	Hoechst AG			
55	$Pd(C_5H_7O_2)_2$	Carbon	IW	Pd loading	O_2, CO_2 and H_2 Chemisorption	Calcination and reduction yields better dispersion than just reduction for both C and SiO_2 supports.
56	PTA	SiO_2		Precursor		
				Pretreatment reduction in H_2	XRD	
				Pretreatment calcination in O_2, reduction in H_2		Further "re-calcination" and "re-reduction" improves dispersion.
				Pretreatment calcination in O_2		
57	Pt	Al_2O_3	Vapor deposition	Pretreatment in H_2	High resolution EM	Calcinated (O_2) samples yield larger particles than reduced (H_2) samples
				Pretreatment in O_2		
				Pretreatment length		The longer the pretreatment, the larger the particles
58	Pt	SiO_2 gel	Ion-exchange	Pretreatment reduction temperatures in H_2	H_2 adsorption	Increasing reduction temperatures decreases platinum dispersion.
					XPS	
59	CPA	SiO_2 gel	WI	Pretreatment reduction temperatures in H_2	FTIR	Increasing reduction temperatures decreases platinum dispersion.
60	PTA	SiO_2	DI	Pretreatment calcination temperatures in O_2	XANES	Increasing calcination temperatures decreases platinum dispersion
			SEA		EXAFS	
61	$Pd(NO_3)_2$	SiO_2	Ion-exchange	Pretreatment calcination temperatures in O2	H_2 chemisorption	Calcination temperatures above 500°C cause metal sintering
	$PdCl_2$				TEM	
62	PTA	SiO_2	Ion-exchange DI	Reduction treatment temperatures in H_2	H_2 chemisorption	Higher temperatures during H_2 heat treatment increases sintering.

Ref	Metal / Precursor	Support	Production Method(s)	Treatment variables	Analysis methods	Results
63	CPA	SiO_2	Ion-exchange Vaccum evaporation	Heat treatment in O_2, N_2, H_2O and Cl_2 atmospheres	TEM	Heat treatment with O_2 enhances sintering Heat treatment with H_2O inhibits sintering No crystallite migration observed, PMC can't be sintering mechanism
64	CPA	Al_2O_3	WI	Time of heat treatment in H_2	CO chemisorption	Longer time of heat treatment in H_2 increases sintering
65	Pt	Al_2O_3		Reduction treatment temperatures in H_2	XRD CO Chemisorption	Higher temperatures during H_2 heat treatment increases sintering.
66	$Pt(NH_3)_2$--$(NO_3)_2$	Carbon	DI WI	Reduction treatment temperatures in H_2 Time of heat treatment in H_2	Electron microscopy	Higher temperatures during H_2 heat treatment increases sintering. Longer time of heat treatment in H_2 increases sintering
67	CPA	Al_2O_3	WI	Reduction treatment temperatures in H_2	XRD	Higher temperatures during H_2 heat treatment decreases dispersion.
68	CPA	Al_2O_3	WI Pre-fabricated Engelhard 0.5% Pt	Reduction treatment temperatures in H_2 Time of heat treatment in H_2	XRD	Higher temperatures during H_2 heat treatment increases sintering. Longer time of heat treatment in H_2 increases sintering
69	CPA	Al_2O_3	WI	Pretreatment reduction temperatures in H_2	Hydrogenation of cyclohexane Decomposition of H_2O_2	Progressive decrease in Pt catalytic activity and dispersion for temperatures <400°C, and progressive increase in catalytic activity and dispersion for tempertures >400°C.
70	CPA	Al_2O_3	WI Pre-fabricated Engelhard 0.3 and 0.5% Pt	H_2 reduction normal treatment after pretreatment.	Electron microscopy	Reduction treatment at 300°C causes sintering.
71	PdTC $Pd(OAc)_2$ PdTA	Carbon	IW	Pretreatment reduction temperatures in H_2	CO chemisorption Cyclohexane hydrogenation	Maximum CO chemisorption is achieved when catalysts are reduced at temperatures from 97°C to 147°C. Strong decrease in Pd dispersion at temperatures >147°C.
72	$Pd(OH)_2$ and PdTC	Carbon	IW	Reduction treatment temperatures in H_2	TEM Hydrogenation of benzene	Pd sintering starts at 120°C Sharp loss in catalytic activity starts at 350°C

Ref	Metal / Precursor	Support	Production Method(s)	Treatment variables	Analysis methods	Results
73	$C_3H_3PdC_5H_5$	Carbon	WI	Pretreatment reduction in H_2 at various temps	TEM XPS	Higher temperatures in H_2 reduction during pretreatment increases Pd particle size.
74	Pd	Al_2O_3	IW	Pretreatment reduction in H_2 at various temps	Toluene oxidation	The activity of samples pretreated in H_2 at 3 different temperatures is: $300^oC > 200^oC > 400^oC$

Abbreviations: CPA-Chloroplatinic acid, DI-Dry impregnation, EM-Electron microscopy, EXAFS-Extended X-ray absorption fine structure, FTIR-Fourier transform infra-red, GLC-Gas-liquid chromatography, HRTEM-High resolution transmission electron microscopy, IW-Incipient wetness, PdTA-Palladium tetraammine, PdTC-Palladium tetrachloride, PTA-Platinum tetraammine, STM-Scanning tunneling microscopy, TEM-Transmission electron microscopy, TPR-Temperature programmed reduction, WI-Wet impregnation, XANES-X-ray absorption near edge spectroscopy, XPS-X-ray photoelectron spectroscopy, XRD-X-ray diffraction.

3. EXPERIMENTAL DESIGN

Platinum and palladium were deposited in five different supports to produce ten catalyst systems. The choice of supports where based on their different surface areas and PZC values. Their specifics are summarized in Table 3.1. The precursors utilized are summarized in Table 3.2. Basic PZC supports where matched with cationic precursors and acidic PZC supports with anionic precursors as explained before.

Table 3.1 Supports used for experimentation.

Support Name	**Manufacturer**	**Abbreviation**	**Surface Area (m^2/g)**	**Pore Volume (ml/g)**	**PZC** [75,77]
HSAG 300 carbon	Timrex	HSAG300	280	0.70	4.5
Aerosil 150 SiO_2	Evonik	SiO2	130	1.25	3.7
Aeroxide TiO_2 P25	Evonik	TiO2	50	0.65	4.5
γ-Al_2O_3 VGL-25	UOP	Al2O3	277	1.70	8.5
Vulcan XC-72 carbon	Cabot	XC72	254	2.30	8.9

Table 3.2 Precursors used for experimentation.

Precursor Formula	**Manufacturer**	**Abbreviation**	**Molecular Weight (g/mol)**
$Pt(NH_3)_4Cl_2$	Aldrich	PTA	334.11
H_2PtCl_6	Aldrich	CPA	409.81
$Pd(NH_3)_4Cl_2 \cdot H_2O$	Aldrich	PdTA	263.44
Na_2PdCl_4	Aldrich	PdTC	294.19

All experimentation and analysis in this research was done in two major portions, samples prepared by DI and SEA. All DI samples were prepared and experimented on with an initial set-up. Based on the results obtained, some adjustments were made for the trials of the samples prepared by SEA. For this reason, some of the experimentation is slightly different for the DI and SEA samples. The experiment design for both will be explained separately.

3.1 Catalysts prepared by DI

The metal loading for each metal-support system produced through DI was calculated to match the maximum theoretical loading attainable through SEA based on the precursor surface coverage Γ, previously determined by Santhanam et al. [75], displayed in Table 3.3. The weight of metal per gram of support is calculated by the following equation:

$$\frac{\text{MetalWt[g]}}{\text{Supp.Wt[g]}} = \text{Prec. Surf. Cov.}\,[\mu\text{mol/m}^2] \times 10^{-6}[\text{mol/}\mu\text{mol}] \times \text{MetalMW[g/mol]} \times \text{SA}[\text{m}^2/\text{g}] \quad (3.1)$$

The amount of precursor necessary is retrievable by the following calculation:

$$\text{Prec. Wt[g]} = \frac{\text{MetalWt[g]} \times \text{Prec. MW[g/mol]}}{\text{MetalMW[g/mol]}} \times \text{Supp. Wt[g]} \quad (3.2)$$

The catalysts where produced on 5 grams of support batches, enough quantity for all pretreatment experiments. DI samples were prepared according to the data of Table 3.3. The precursor was dissolved in a de-ionized water volume equal to the pore volume of the 5 grams of support. The precursor solution was added drop-wise to the support with constant shaking until a thick slurry was acquired. The samples where then dried at 45^{o}C for 16 hours.

Table 3.3 Catalyst samples DI preparation data, basis: 5 g of support.

Catalyst System	**Surface Coverage Γ [μmol/m^2]**	**Metal loading Wt%**	**Precursor Wt. [g]**	**Solution Vol. [ml]**
HSAG300/PTA	0.85	4.44	0.398	3.50
HSAG300/PdTA	2.00	5.62	0.738	3.50
SiO2/PTA	0.85	2.11	0.185	6.25
SiO2/PdTA	1.50	2.03	0.257	6.25
TiO2/PTA	0.85	0.82	0.071	3.25
TiO2/PdTA	0.50	0.27	0.033	3.25
Al2O3/CPA	1.60	7.96	0.908	8.50
Al2O3/PdTC	1.25	3.55	0.509	8.50
XC72/CPA	1.60	7.35	0.833	11.50
XC72/PdTC	2.00	5.13	0.747	11.50

Before reduction of the samples was performed, they were exposed to a 150 ml/min flow of helium for 15 minutes. Reduction of the catalysts was then done by exposing 0.5 g of sample to 37 ml/min of continuous hydrogen flow for each pretreatment condition. Using temperature control, the samples where heated from room temperature (23^{o}C) at heating rates of 0.5^{o}C/min, 2.5^{o}C/min and 5.0^{o}C/min. The samples where brought up to final temperatures of 200^{o}C and 500^{o}C, where they stayed for 1 hour. Then the temperature control was turned off and the catalysts remained in hydrogen flow while they cooled down to a temperature of 90^{o}C, where any kind of reduction or sintering process is believed to stop.

Additional to these 6 sets of conditions, 3 more trials where done with humidity variation. For these 3 tests, a heating rate of 0.5^{o}C/min and final temperature of 200^{o}C was used. Flows of 75 ml/min and 150 ml/min of helium were added to 2 samples to try to produce two further levels of dryness. Helium was introduced to increase the stream flow rate, lower the partial pressure of water and chlorine produced during reduction, and increase their evacuation.

Finally, water vapor was introduced into the hydrogen stream to create a "humid" sample by bubbling the stream of hydrogen through liquid water using a bubbling tip. Using vapor pressure data of water at 23^{o}C [76] it was determined 0.76 mg/min of water were being introduced into the hydrogen flow. The humidity pretreatments were only performed on the platinum-containing catalysts since the results are expected to show a clear pattern so the sampling size was reduced. The pretreatment conditions and net residence time under hydrogen flow are summarized in Table 3.4.

All samples will be identified by the following nomenclature: *Support-Precursor-Prep.Method-PretreatmentNomenclature*. For example, the catalyst produced by DI in alumina, with CPA, reduced to 500^{o}C at 2.5^{o}C/min will be identified as Al2O3-CPA-DI-500-2.5.

Table 3.4 Pretreatment conditions summary for DI*.

Final Reduction Temperature (^oC)	Heating Rate (^oC/min)	Dry/Humid Conditions	Total pretreatment time (hours)	Pretreatment Nomenclature
200	0.5	-	8	-DI-200-0.5
	2.5	-	3	-DI-200-2.5
	5.0	-	2.5	-DI-200-5.0
500	0.5	-	18	-DI-500-0.5
	2.5	-	7.5	-DI-500-2.5
	5.0	-	6	-DI-500-5.0
200	0.5	75 ml/min He	8	-DI-75He
	0.5	150 ml/min He	8	-DI-150He
	0.5	0.76 mg/min water	8	-DI-water

***A flow of 37 ml/min of hydrogen was used for all trials.**

Reduced samples where then examined by XRD in a Siemens D5000 diffractometer with Cu*K*α radiation (λ=1.5406 Å) operated at 30 kV and 40 mA, operating in Bragg-Brentano geometry. The angle range was set from 10^o to 70^o 2θ with a step size of 0.02^o and 1.2 s exposure time at each angle. Average particle sizes were calculated by using the Scherrer equation, as explained in Section 2.3.1, with a K value of 0.94.

STEM Z-contrast image analysis for all catalyst samples prepared by DI was performed on a JEOL JEM-2010F TEM/STEM with a digital camera at Research Resources Center, University of Illinois at Chicago. It is a 200 kV field emission transmission electron microscope with a Schottky field emission electron source and fitted with an ultra-high resolution pole piece, which in STEM mode is capable of producing a probe size of 0.13 nm with 15 pA of current. Images were taken using a high angle annular dark field detector. Each image was then analyzed using "Particle2.exe" software to determine average particle size as well as standard deviation. Approximately 1000 particles were counted per sample, when possible.

3.2 Catalysts prepared by SEA

A surface of loading of 1500 m^2/L was chosen for SEA preparation. The same values of Table 3.3 where used for SEA except for the volume of solution required, which was calculated using equation (2.1). For a basis of 5 g of support, the values for preparation by SEA are shown in Table 3.5. The amount of precursor used was based on an ideal maximum adsorption calculation using equations (3.1) and (3.2). The actual metal loading has to be calculated after the adsorption process.

Table 3.5 Catalyst samples SEA preparation data, basis: 5 g of support.

Catalyst System	Surface Coverage [µmol/m^2]	Precursor Wt. [g]	Solution Vol. [ml]
HSAG300/PTA	0.85	0.398	933
HSAG300/PdTA	2.00	0.738	933
SiO2/PTA	0.85	0.185	433
SiO2/PdTA	1.50	0.257	433
TiO2/PTA	0.85	0.071	167
TiO2/PdTA	0.50	0.033	167
Al2O3/CPA	1.60	0.908	923
Al2O3/PdTC	1.25	0.509	923
XC72/CPA	1.60	0.833	847
XC72/PdTC	2.00	0.747	847

Once the metal precursor solution is prepared, the pH has to be adjusted for maximum adsorption. The pH for each support must be found by building an uptake survey curve. Since the pH of the precursor solution will shift, the final pH is plotted versus the uptake (Γ). Precursor solution samples before and after contact with the support are analyzed in a PerkinElmer Optima 2000 DV Inductively Coupled Plasma (ICP) to find the difference in metal

concentration which would be the amount of metal adsorbed by the support. The uptake Γ is calculated by the following equation:

$$\Gamma[\mu mol/m^2] = (Conc_{initial} - Conc_{final})[mg/L] \times \frac{10^6[\mu mol/mol]}{SL[m^2/L] \times MetalMW[g/mol] \times 1000[mg/g]} \quad (3.3)$$

The plot of the final solution pH versus the uptake Γ will usually reveal a volcano-shaped curve. Results for all five supports are displayed in Figure 3.1 where the low PZC supports were put in contact with PTA solutions while CPA was adsorbed onto the high PZC supports. For SEA preparation the precursor solution's pH must be adjusted so that the final pH equals the support's maximum adsorption pH.

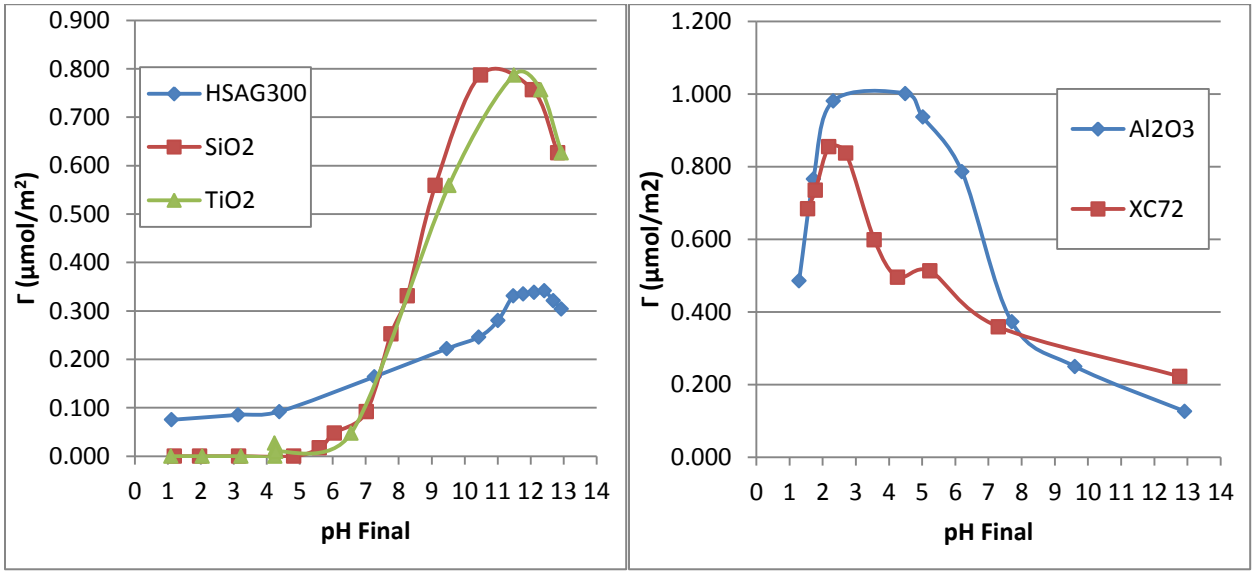

Figure 3.1 (left) Uptake curves for low PZC supports with PTA, (right) Uptake curves for high PZC supports with CPA.

Figure 3.1 reveals the ideal final pH for the supports: pH 12 for HSAG300, pH 10.5 for SiO2, pH 11 for TiO2, pH 4 for Al2O3, and pH 2.5 for XC72. Each precursor solution was prepared according the quantities in Table 3.5 and adjusted to the initial pH values depicted in Table 3.6 using HCl and NaOH solutions. The 5 g of each support where introduced into the precursor solutions of appropriate volume, concentration, and pH, and were shaken for 1 hour.

The impregnated support was later filtered and dried at 45°C for 16 hours. The actual metal loadings for each catalyst system after ICP analysis are shown in Table 3.6.

Table 3.6 Catalyst samples SEA preparation data.

Support	Precursor	Initial pH	Final pH	Solution initial metal concentration (mg/L)	Solution final metal concentration (mg/L)	Γ (μmol/m^2)	Metal loading wt.%
HSAG300	PTA	12.17	12.09	141	35.88	0.36	1.92
HSAG300	PdTA	12.14	12.05	278	216	0.39	1.14
SiO2	PTA	12.01	9.97	234	7.29	0.77	1.93
SiO2	PdTA	11.98	10.09	213	11.3	1.26	1.72
TiO2	PTA	11.89	11.25	256	29.9	0.77	0.75
TiO2	PdTA	11.88	11.38	67.1	0.0	0.42	0.22
Al2O3	CPA	2.50	3.27	319	80.2	0.82	4.22
Al2O3	PdTC	2.49	3.43	160	73.7	0.54	1.57
XC72	CPA	2.50	2.81	783	575	0.71	3.40
XC72	PdTC	2.51	2.86	255	98.7	0.98	2.58

The final adsorption (Γ) values are lower than the ideal values of Table 3.3 probably due to the higher surface loading of 1500 m^2/L used for this experiments whereas Santhanam et al. [75] used much lower surface loadings (25, 50, 100 and 200 m^2/L). All of the pretreatment conditions applied to the SEA samples are same as the DI ones except for one change. It was decided after obtaining the early results of the DI samples that no significant difference was being obtained between the conditions where 75 ml/min of He and the 150 ml/min of He were being introduced into the hydrogen stream. For this reason, the 75 ml/min He pretreatment was eliminated from the SEA trials and it was instead replaced with a "diminished" water vapor addition. This was accomplished by bubbling the hydrogen stream through iced water. According to the vapor pressure calculations, the effective amount of water vapor introduced from water at 3°C into the stream is of approximately 0.22 mg/L, less than a third of other

humidity treatment. This will allow to test if the amount of water introduced in the system has direct influence over the final particle size. For the reasons described in Section 3.1, the humidity variation trials were performed on the platinum-containing samples only. The pretreatment conditions for the SEA samples are summarized in Table 3.7.

Table 3.7 Pretreatment conditions summary for SEA*.

Final Reduction Temperature (^{o}C)	Heating Rate (^{o}C/min)	Dry/Humid Conditions	Total pretreatment time (hours)	Pretreatment Nomenclature
200	0.5	-	8	-SEA-200-0.5
	2.5	-	3	-SEA-200-2.5
	5.0	-	2.5	-SEA-200-5.0
500	0.5	-	18	-SEA-500-0.5
	2.5	-	7.5	-SEA-500-2.5
	5.0	-	6	-SEA-500-5.0
200	0.5	150 ml/min He	8	-SEA-150He
	0.5	0.22 mg/min water	8	-SEA-ice
	0.5	0.76 mg/min water	8	-SEA-water

***A flow of 37 ml/min of hydrogen was used for all trials.**

Particle size analysis by XRD was performed in the same manner as described in the end of Section 3.1. STEM analysis for the SEA prepared samples had to be done in a different, more advanced instrument than the one used of the DI samples. The STEM analysis on the SEA samples was done on a JEOL JEM-ARM200CF microscope. Imaging in this instrument was done by Z-contrast as well. This electron microscope has a 200 kV field emission, in STEM mode is capable of producing a probe size of 0.078 nm with 15 pA of current. Images were taken using a high angle annular dark field detector. Each image was again analyzed using "Particle2.exe" software to determine average particle size as well as standard deviation. Approximately 1000 particles were counted per sample, when possible.

4. RESULTS AND DISCUSSION

It is only appropriate that the outcomes of the particle size analysis is presented separately for the DI and the SEA samples since their nature and general results are different. Not all characterization methods revealed the same amount of information about each set of samples so only the most relevant and conclusive results will be shown.

4.1 Catalysts prepared by DI

The particle counting in the STEM images could not be carried-out in a typical manner for most of the samples. Because of the nature of the DI preparation method, the STEM images showed metal particle clusters with sizes ranging from 10 to 500 nm. These clusters don't have a usual spherical shape, which is expected of regular particles, and show a rather "snowflake" type of shape, which cannot be properly measured with the "Particle2.exe" software.

Table 4.1 Clustering Index.

CI	Cluster size
1	5 - 10 nm
2	10 - 50 nm
3	50 - 100 nm
4	100 - 500 nm
5	> 500 nm

(a) CI = 2 (b) CI = 3 (c) CI = 5

Figure 4.1 Clustering Index examples. (a) SiO2-PTA, (b) HSAG300-PTA, (c) HSAG300-PTA.

Only the particles with spherical and close-to spherical shapes were included in the particle size analysis. The random-shaped clusters were accounted for by introducing a clustering index (CI), as described in Table 4.1 above. The CI should be used to demonstrate the extent of sintering in a sample. Some examples of Clustering Indices are shown in Figure 4.1.

4.1.1 Catalysts supported on HSAG300

The XRD results for the HSAG300-PTA catalyst at all the pretreatment conditions are depicted in Figure 4.2. The locations where platinum peaks are expected have been marked. The particle sizes were calculated from XRD using the Scherrer formula (2.10).

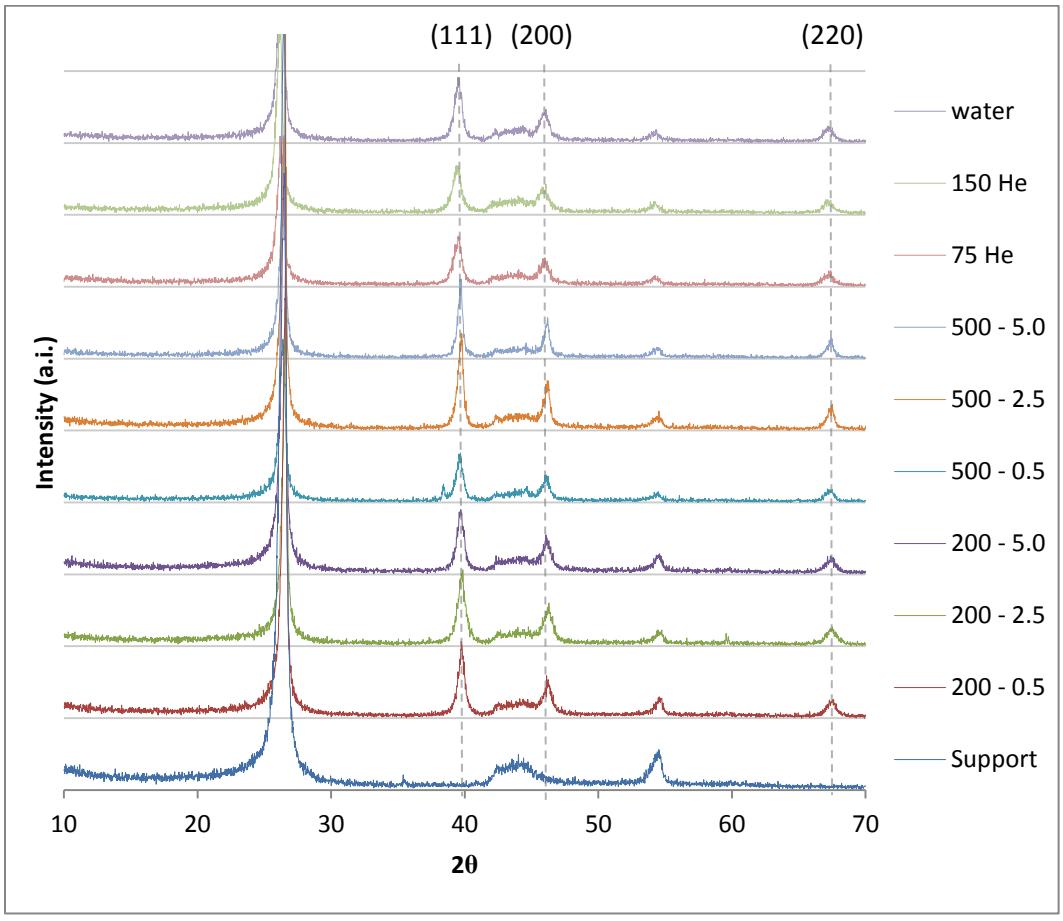

Particle Size [nm]
6.5
5.2
5.8
9.5
10.0
7.9
5.7
5.9
6.3

Figure 4.2 XRD results for HSAG300-PTA-DI.

The support's sharp peak at 26° and the two smaller peaks at 43° and 54° correspond to a high degree of crystallinity of graphitic carbon [78]. From these results it can be seen the

platinum dispersion is low for all samples. There seems to be no obvious and clear sintering pattern. This is somewhat expected since catalyst preparation by DI most likely yields big particle sizes in uneven distributions throughout the support. A closer look however shows the group of samples reduced at 500^{o}C is bigger than the rest. Also the "dry" samples (where He was introduced in the stream) generated the smallest particles of all. The presence of water seems to have no strong influence on the particle sizes.

Table 4.2 STEM particle size analysis for HSAG300-PTA-DI.

	200°C			**500°C**			**200°C at 0.5°C/min**		
	0.5°C/ min	**2.5°C/ min**	**5.0°C/ min**	**0.5°C/ min**	**2.5°C/ min**	**5.0°C/ min**	**75 He**	**150 He**	**water**
<*p*>	7.8	4.7	5.4	12.5	15.0	10.7	2.5	3.2	15.4
n	654	251	359	1814	1130	1729	407	1018	1040
sd	7.8	2.6	2.9	9.2	15.5	12.5	2.6	5.4	8.4
CI	3	5	5	5	5	5	5	4	5

<p> – average particle size, n – number of particles counted, sd – standard deviation, CI – clustering index.

STEM particle size analysis for the HSAG-PTA-DI catalyst gives more information about the clustering of the particles, as well as the particle size distribution. Table 4.2 summarizes the STEM imaging findings. The STEM average particle sizes are notably different from the XRD results. This may be due to the fact that XRD measures the size of individual metal grains which reflect the X-rays while STEM is based on a visual evaluation of the particles found and it is easy to count particles touching each other as a single bigger particle. Nevertheless, the STEM results show a similar pattern of particle sizes as the XRD. Once again the group of samples reduced at 500^{o}C is bigger than that the rest. Clearly the "dry" samples are the smallest of all demonstrating the value of increased evacuation of water. Severe sintering and clustering of the platinum particles for most of the samples is evidenced by the clustering index values of Table 4.2. Some examples of these clusters are shown in Figure 4.3.

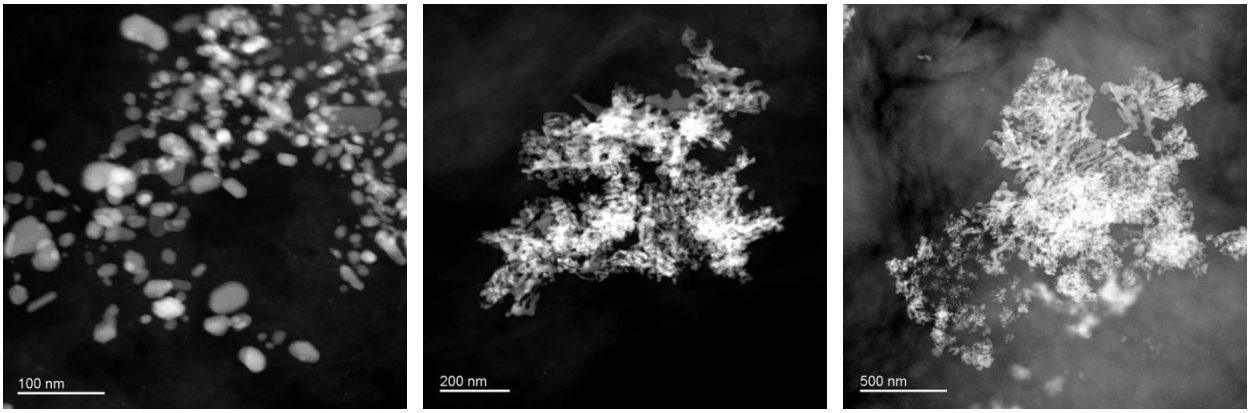

500°C – 5.0°C/min | 150He | water

Figure 4.3 STEM images for HSAG300-PTA-DI catalysts.

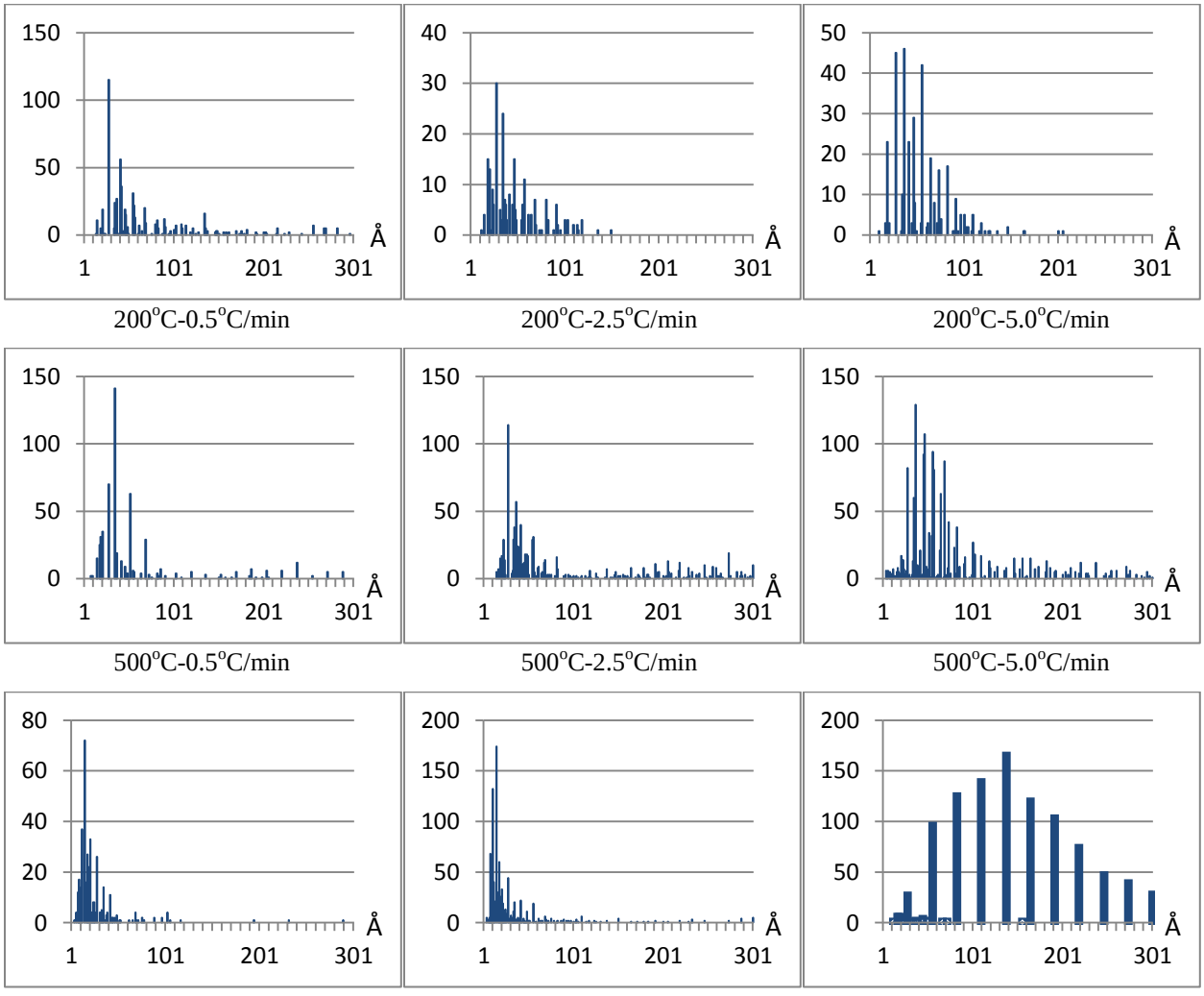

200°C-0.5°C/min | 200°C-2.5°C/min | 200°C-5.0°C/min

500°C-0.5°C/min | 500°C-2.5°C/min | 500°C-5.0°C/min

75He | 150He | water

Figure 4.4 Particle size distributions for HSAG300-PTA-DI catalysts.

Figure 4.4 shows how the particle size distributions widen as higher heating rates are used. Also, it can be seen that bigger particles start becoming more common at the 500°C reduction temperature at every heating rate compared to their 200°C counterpart. Even though the average particle size didn't increase with the heating rate, the widening of the particle size distribution implies platinum particles became more mobile. The narrowest particle size distributions where produced by the "dry" samples while the "humid" sample produced a completely different distribution shape verifying how the presence of water during reduction enhances sintering.

For the HSAG-PdTA-DI catalysts, the XRD results are shown in Figure 4.5. Again, no obvious pattern in the palladium particle sizes can be easily noticed at first glance probably due to the random particle distribution nature of the DI preparation method.

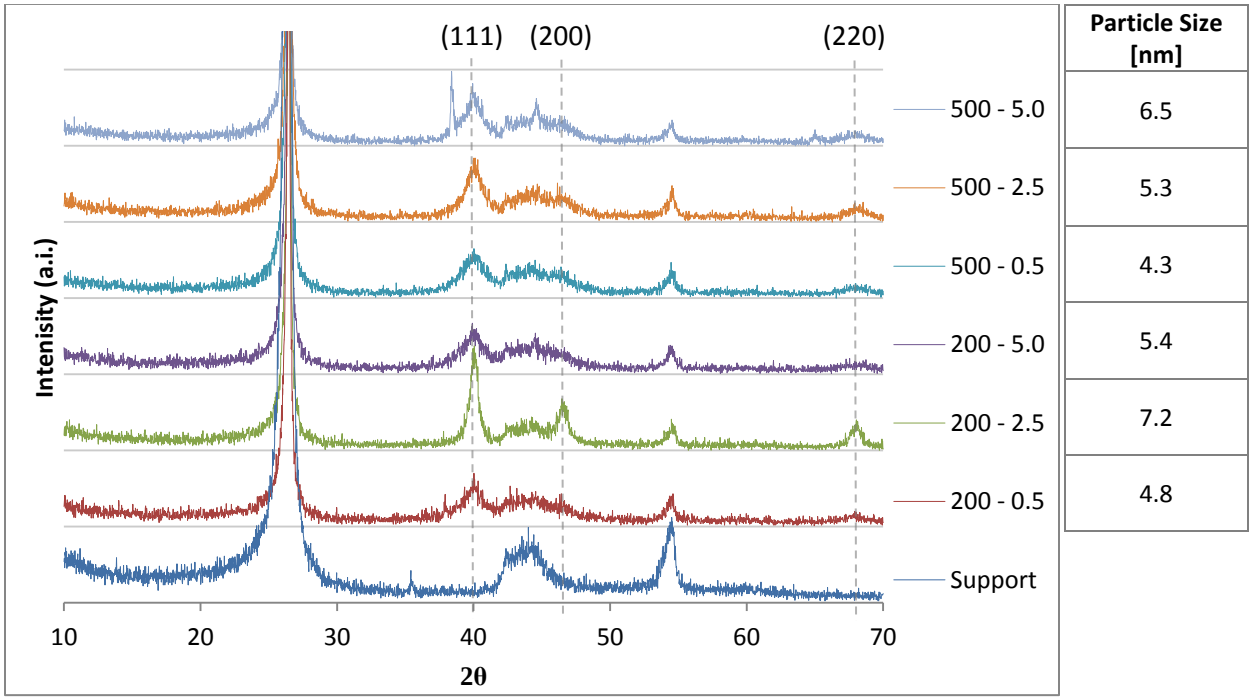

Figure 4.5 XRD results for HSAG300-PdTA-DI.

The STEM particle size analysis results in Table 4.3 and Figure 4.6 for the HSAG300-PdTA-DI catalysts reveal results that mirror those obtained by XRD. Again the HSAG300-PdTA-DI-200-2.5 sample has unexplainably the biggest particle size and the widest particle size

distribution. Though the particle sizes are still characteristic of low dispersion samples, it seems this precursor suffered far less clustering and sintering than the platinum samples, as demonstrated by the clustering indices, the standard deviations, and the average particle sizes.

Table 4.3 STEM particle size analysis for HSAG300-PdTA-DI.

	200°C			**500°C**		
	0.5°C/ min	**2.5°C/ min**	**5.0°C/ min**	**0.5°C/ min**	**2.5°C/ min**	**5.0°C/ min**
<*p*>	2.9	6.5	3.0	4.2	4.8	4.8
n	3852	4202	2092	1089	987	1038
sd	1.5	5.2	1.4	1.4	1.7	1.6
CI	1	2	1	1	1	1

<p> – average particle size, n – number of particles counted, sd – standard deviation, CI – clustering index.

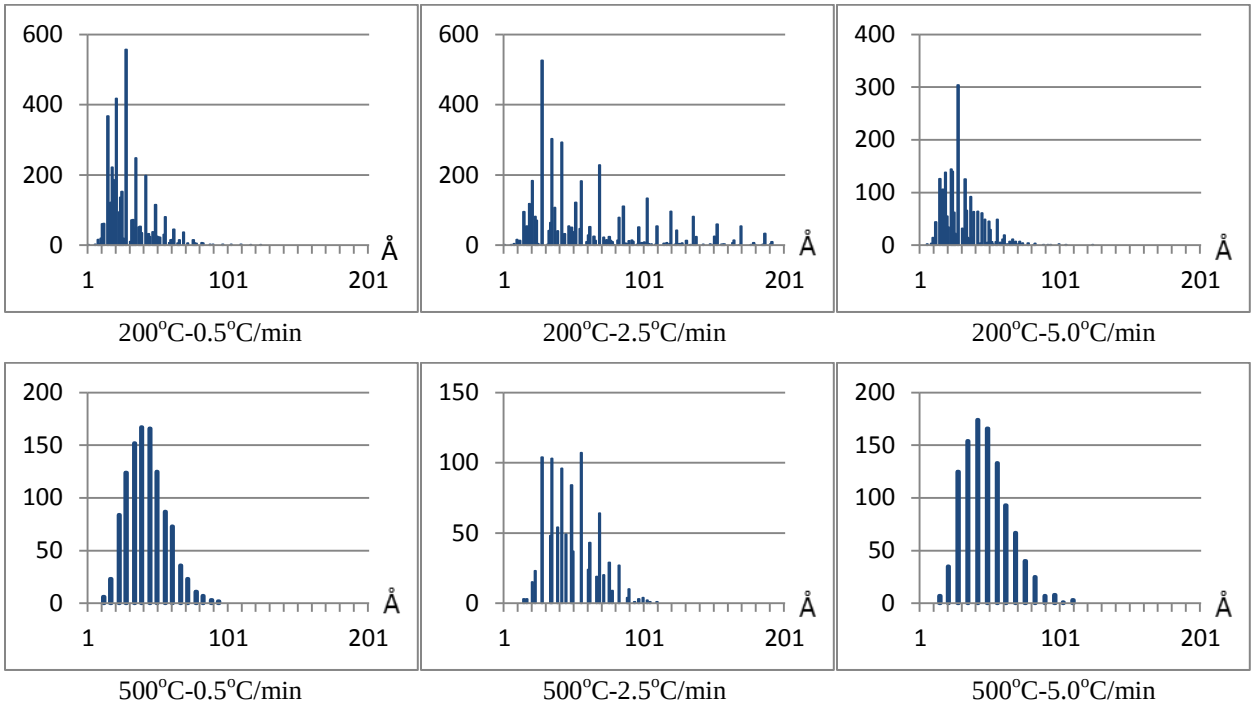

Figure 4.6 Particle size distributions for HSAG300-PdTA-DI catalysts.

The STEM particle size distributions shown in Figure 4.6 don't show any noticeable widening pattern. A common trait between the HSAG-PTA-DI and the HSAG-PdTA-DI catalysts particle size distributions is the fact that the "volcano" leans towards the left and has a

thin extension towards the right. As it was explained in Section 2.1, this particle size distribution shape is characteristic of the PMC sintering mechanism, which suggests sintering is happening by the migration and coalescence of particles. Particle clustering was very much present in the HSAG300-PTA samples but it is still not clear if this was due to the sintering mechanism itself, or just to the erratic distribution of precursor resulting from DI preparation. Further results for this catalyst system prepared by SEA should help clarify this.

4.1.2 Catalysts supported on SiO2

Similar tendencies to the general sintering behavior found in the HSAG300 samples are found in the SiO2-PTA catalysts. The XRD analysis of Figure 4.7 shows low overall dispersions for the catalyst samples. The samples reduced at 500^{o}C of temperature are the group with the biggest particle size. As the heating rate increases, so does the particle size of each sample reduced at the same temperatures. The sintering behavior is clearer in these platinum-silica systems compared to the HSAG300 catalysts. In agreement with the previous HSAG300 catalyst results, the "dry" samples are the smallest of all. Humidity didn't play such a critical role in the creation of bigger metal particles once again. It would appear that although water does seem to make metal particles more mobile, which increases clustering, the particles themselves are not dramatically increased in size, at least in the catalyst prepared by DI where particles are larger in general.

STEM imaging for the SiO2-PTA samples revealed particles of shapes and sizes not suitable for regular particle size analysis. The clustering index values shown in Table 4.4 do provide a perception of the extent of sintering suffered by the samples at each pretreatment condition. As it is shown in a few examples in Figure 4.8, it would seem that most of the platinum mass has merged throughout the support to form these large flakes which appear to increase in size with

higher heating rates and reduction temperatures. It is important to note the silica support quickly gets charged with static under the STEM electron beam which creates interference at high magnifications and makes the finding of small metal particles more difficult.

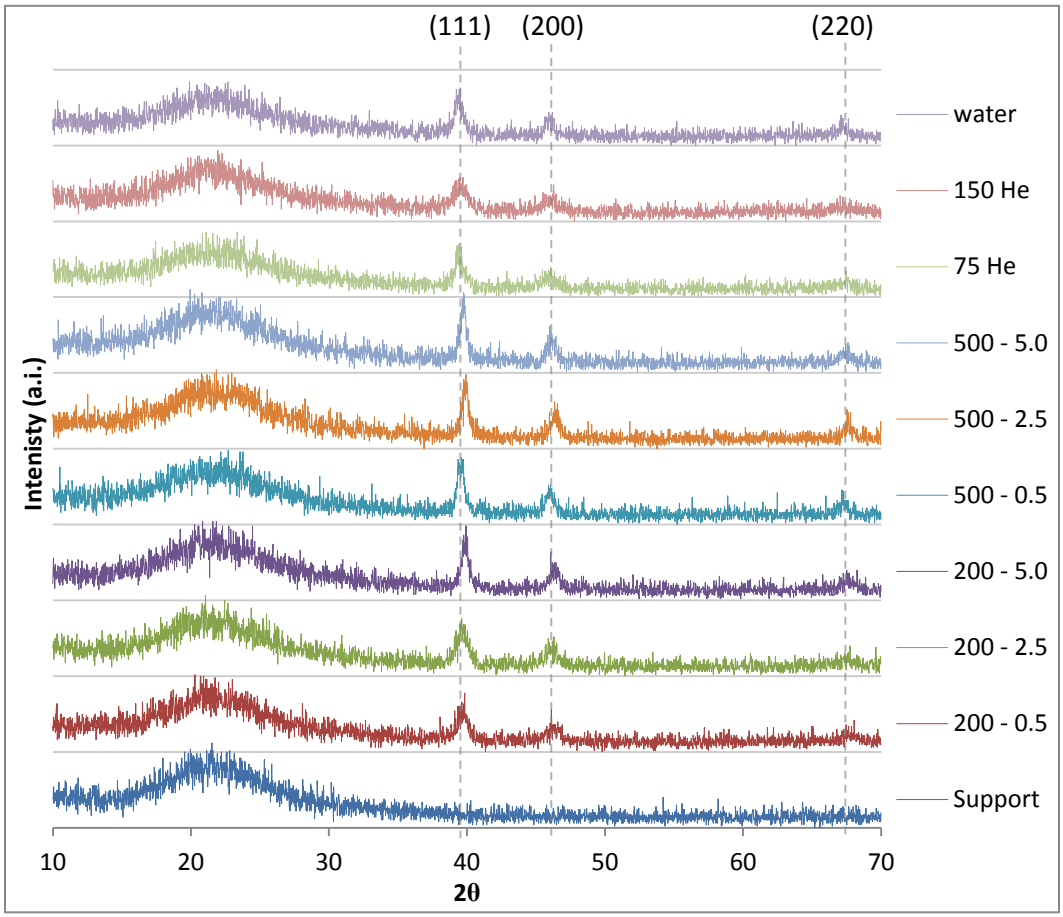

Particle Size [nm]
7.7
6.4
7.4
14.5
13.0
10.5
11.2
7.3
7.3

Figure 4.7 XRD results for SiO2-PTA-DI.

Table 4.4 STEM particle size analysis for SiO2-PTA-DI.

	200°C			500°C			200°C at 0.5°C/min		
	0.5°C/ min	2.5°C/ min	5.0°C/ min	0.5°C/ min	2.5°C/ min	5.0°C/ min	75 He	150 He	water
CI	3	3	4	4	5	5	3	3	5

CI – clustering index.

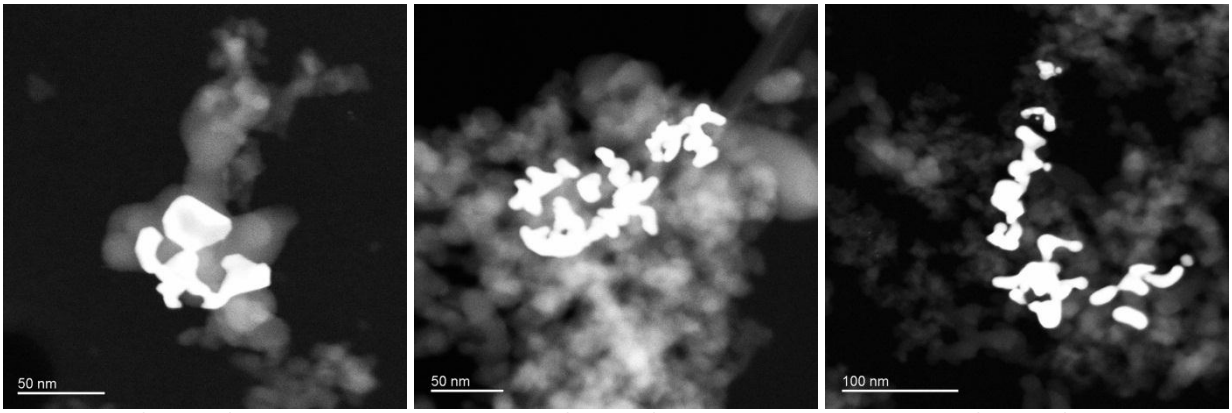

200°C – 0.5°C/min | 200°C – 2.5°C/min | 200°C – 5.0°C/min

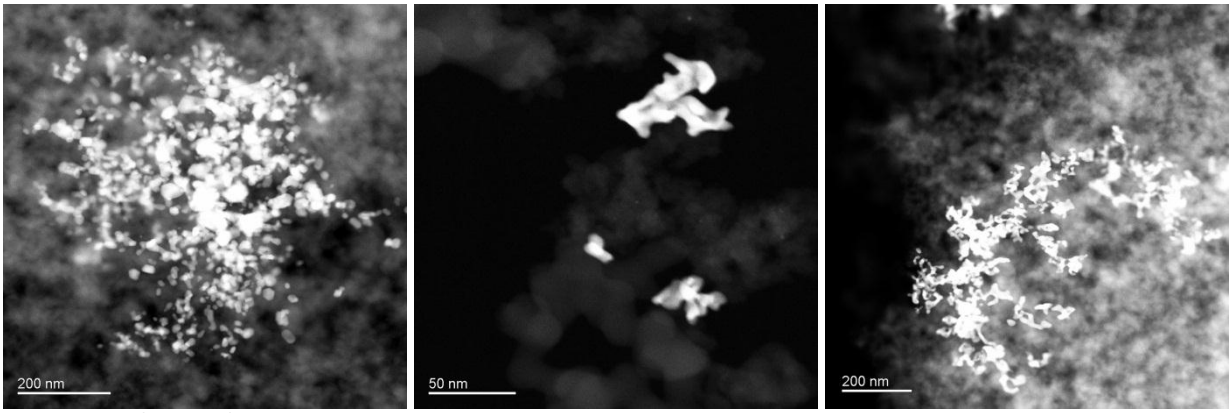

500°C – 5.0°C/min | 150He | water

Figure 4.8 STEM images for SiO2-PTA-DI catalyst.

The palladium on silica particle sizes obtained by XRD (Figure 4.9) don't disclose any marked sintering pattern. These palladium particles are, for the most part, larger than the platinum ones deposited on silica as well. Once again, it appears reduction temperatures and heating rates didn't have as much influence over the larger particle sizes usually produced by the DI preparation method. Unfortunately, STEM particle analysis couldn't provide any more valuable information. Very little palladium was found in the STEM images probably because these larger particles are deposited in the form of large clusters in the thicker support masses. A combination of contamination by the high static interference innate of the support, with decreased contrast in the HAADF images by the lower molecular weight of palladium, together

with the fact that the metal was deposited mostly on the thicker silica masses, made the STEM imaging ineffective.

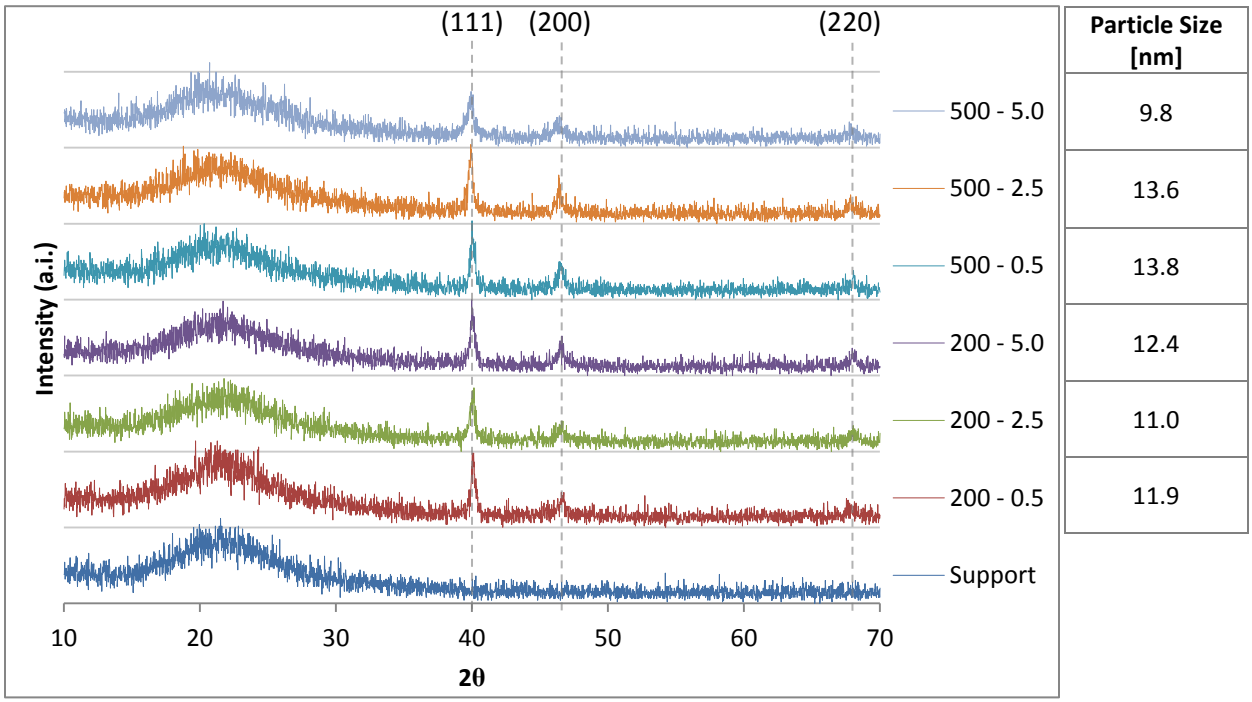

Particle Size [nm]
9.8
13.6
13.8
12.4
11.0
11.9

Figure 4.9 XRD results for SiO2-PdTA-DI.

4.1.3 Catalysts supported on TiO2

The peak pattern for the pure support in the XRD analysis of Figure 4.10 is characteristic of titanium dioxide in the anatase phase [79]. Either because the platinum loadings in the TiO2 support where so low (0.82%), or because the crystallite sizes where under 2 nm, or a combination of both, the XRD graphs didn't show any peaks in the expected locations for platinum. Once a few key samples were evaluated by XRD (Figure 4.10) and no results were shown, XRD analysis was discontinued as the chance of results appearing for the rest of the samples is slim.

STEM analysis revealed a familiar pattern found in the HSAG300 and SiO2 catalysts as well. The data displayed in Table 4.5 demonstrates again how the average particle size from the group of samples reduced at 500^{o}C is in general larger than those reduced at 200^{o}C. The platinum

particles from the "dry" samples are the smallest of all (with a lower standard deviation as well). Finally the "humid" sample not only has larger average particle size, but also a higher standard deviation and clustering index, which indicates the clear influence water had on its sintering.

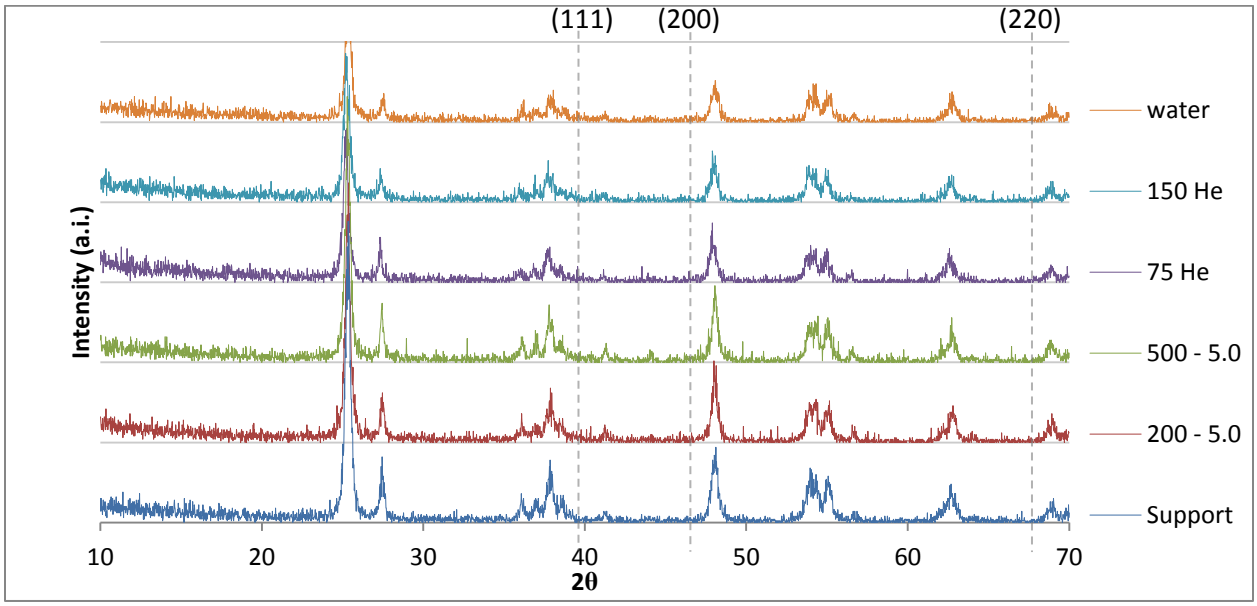

Figure 4.10 XRD results for TiO2-PTA-DI.

Table 4.5 STEM particle size analysis for TiO2-PTA-DI.

	200°C			500°C			200°C at 0.5°C/min		
	0.5°C/ min	**2.5°C/ min**	**5.0°C/ min**	**0.5°C/ min**	**2.5°C/ min**	**5.0°C/ min**	**75 He**	**150 He**	**water**
<*p*>	3.0	2.9	3.0	4.7	3.0	4.5	2.2	2.2	9.1
n	526	922	564	335	393	223	1013	1100	165
sd	1.4	1.4	1.6	3.1	1.8	2.9	0.91	0.97	5.5
CI	2	2	2	2	1	2	2	2	3

<p> – average particle size, n – number of particles counted, sd – standard deviation, CI – clustering index.

Particle size distribution study from STEM results (Figure 4.11) shows a slight widening of the "bells" of the samples reduced at higher temperature demonstrating its influence on sintering. The samples where helium was added to the flow of hydrogen during reduction have the narrower distributions, once again illustrating the importance of efficiently evacuating water during pretreatment reduction to produce the smallest metal particles. Dramatic sintering and

widening of the particle distribution was seen once again in the sample reduced under humid conditions. As sintering increases throughout the samples, a thin extension to the right of the bell starts appearing, this is in agreement with the PMC sintering mechanism.

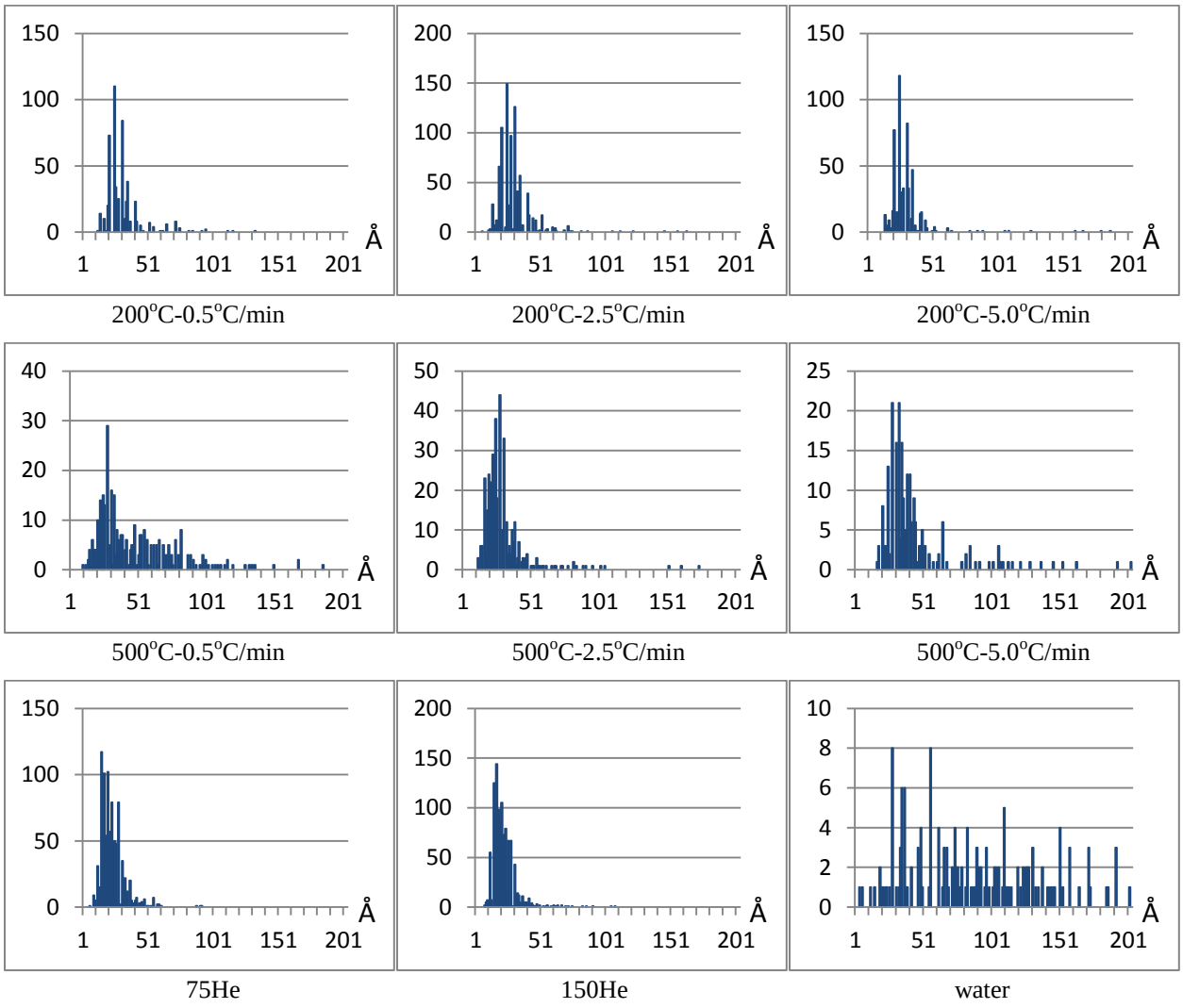

Figure 4.11 Particle size distributions for TiO2-PTA-DI catalysts.

No results for the palladium impregnated on TiO2 could be obtained by either XRD or STEM characterization. The very low palladium loading (0.27%) made XRD examination for these samples fruitless. When attempting STEM analysis, the relative closeness of the molecular weights of palladium and titanium, combined with the thick granules of the TiO2 support where

the palladium should have deposited, made the palladium particles unrecognizable under Z-contrast imaging.

4.1.4 Catalysts supported on Al2O3

The initial XRD inspection of the Al2O3 un-impregnated support in Figure 4.12 detected it had three inherent wide peaks in the exact positions where the peaks for platinum and palladium were expected to appear.

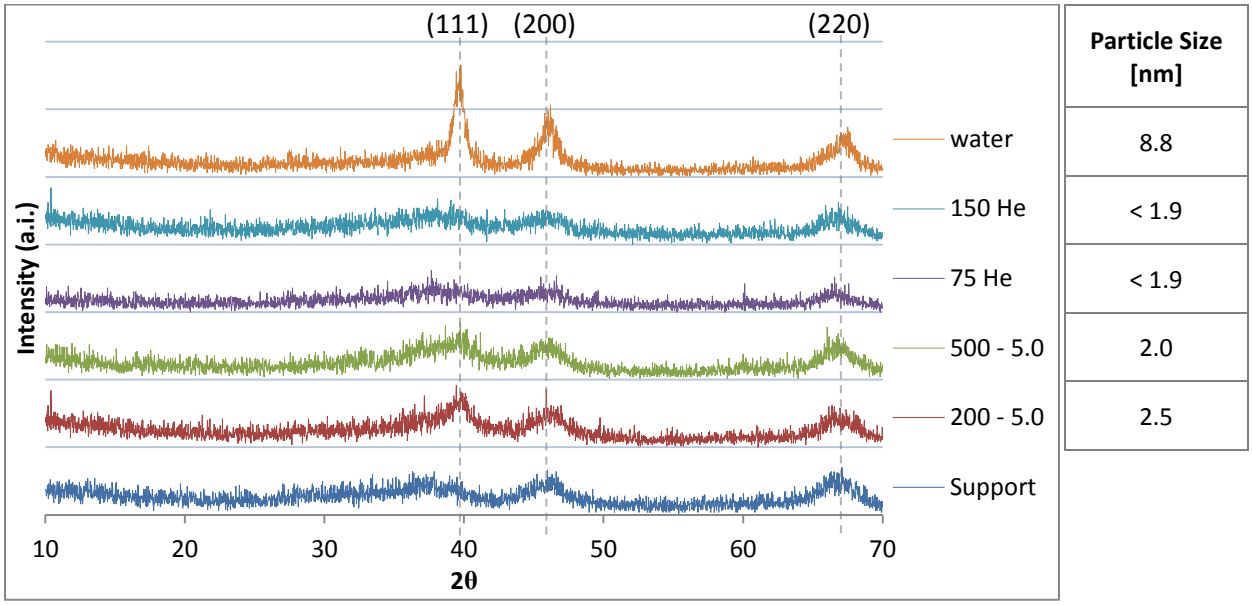

Particle Size [nm]
8.8
< 1.9
< 1.9
2.0
2.5

Figure 4.12 XRD results for Al2O3-CPA-DI.

Unless the metal particles were composed of large crystallites, their peaks would be very weak and ultimately diluted into the support's natural peaks. The initial XRD analysis of a few key samples in Fig. 4.12 confirms most of the platinum peaks will be too weak to be measured accurately, except for the "humid" sample. The values provided in Fig. 4.12 are approximations since the real breadth of the peaks is unidentifiable. These rough results do show the "dry" samples have the smallest particles which, by showing no peaks, have an average size of less than 1.9 nm. The humid sample shows a prominent peak which demonstrates how much dispersion was hurt by the presence of water vapor in the hydrogen stream.

More conclusive results are displayed in Table 4.6 from STEM imaging particle counting. Each of the samples reduced at 500^{o}C had a slightly bigger particle size than their counterpart reduced at 200^{o}C. The presence of helium enhanced the dispersion of the Al2O3-CPA-DI-150He sample resulting in an average particle size of 1.1 nm, equivalent to a dispersion of approximately 91%.

Table 4.6 STEM particle size analysis for Al2O3-CPA-DI.

	200°C			**500°C**			**200°C at 0.5°C/min**		
	0.5°C/ min	**2.5°C/ min**	**5.0°C/ min**	**0.5°C/ min**	**2.5°C/ min**	**5.0°C/ min**	**75 He**	**150 He**	**water**
<*p*>	1.5	2.1	1.5	1.8	2.2	2.1	1.4	1.1	
n	1023	1269	1072	1024	1025	1066	1428	1004	
sd	0.54	0.63	0.61	0.38	0.47	0.46	0.43	0.28	
CI	-	2	1	-	1	-	1	-	5

<p> – average particle size, n – number of particles counted, sd – standard deviation, CI – clustering index.

Particle counting was unfeasible for the "humid" sample since its sintering was too severe. Figure 4.13 illustrates the extent of sintering of the water vapor containing sample compared to the smallest average particle size samples. Since this precursor (CPA) produces chlorine gas during reduction, increased evacuation by the presence of helium plays a vital role in lessening the metal sintering.

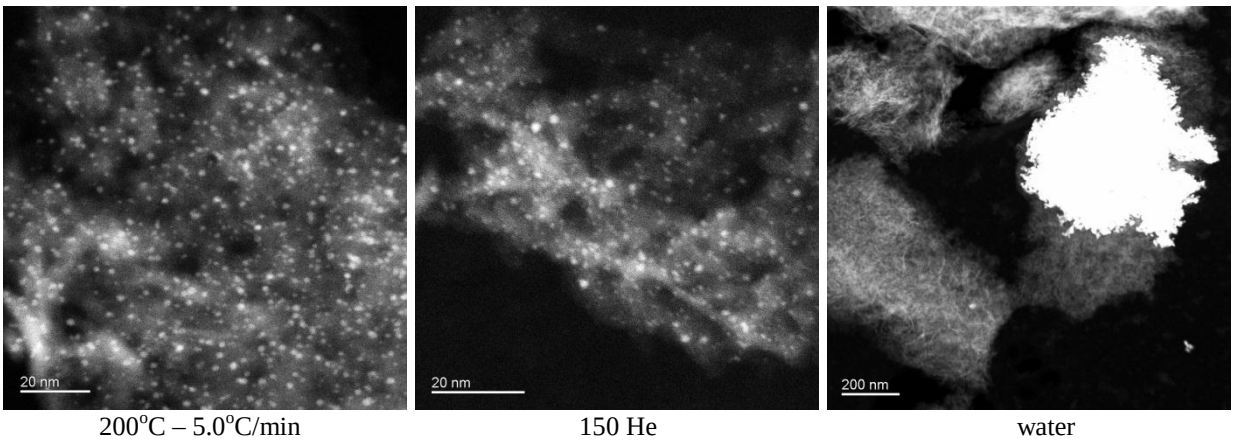

200^{o}C – 5.0^{o}C/min 150 He water

Figure 4.13 STEM images for Al2O3-CPA-DI catalyst.

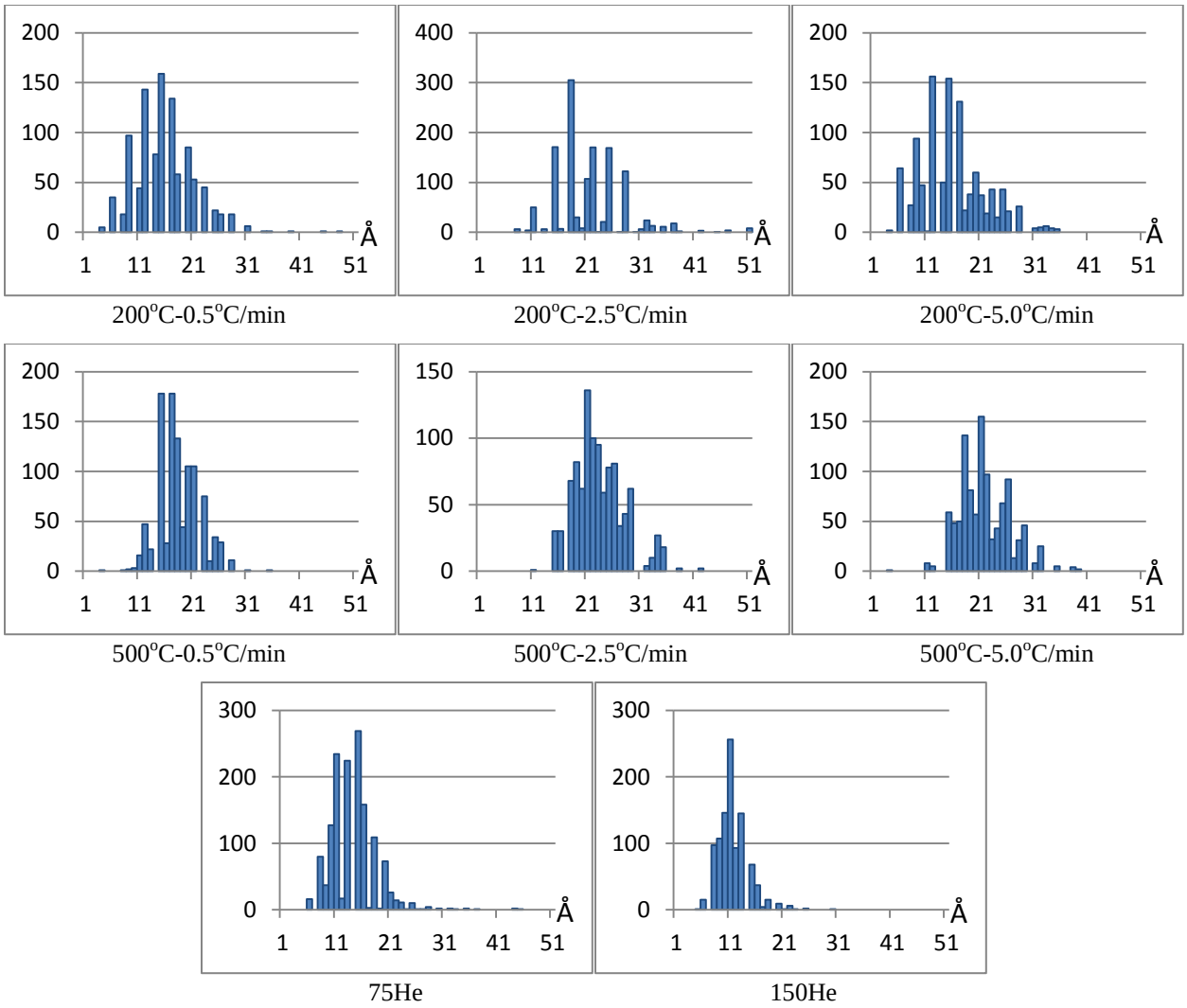

Figure 4.14 Particle size distributions for Al2O3-CPA-DI catalysts.

The particle size distributions for the Al2O3-CPA samples are depicted in Figure 4.14. It can be observed in the case of this catalyst, which has smaller average particles compared to the previous DI prepared catalysts, the distributions don't resemble much of a PMC shape. Many of these samples actually portray rather symmetrical distributions which even though doesn't necessarily deny a PMC sintering mechanism taking place, could open field for the argument that an OR sintering mechanism is happening as well. This is plausible considering the dispersion of all the Al2O3-CPA-DI samples is relatively high which implies small particles

(that have high chemical potential atoms on their surface) are very close to each other, which is a perfect condition for individual metal atom migration consistent with OR theory .

The Al2O3-CPA-DI catalysts showed small particles because the CPA solution used for the impregnation of the alumina support was of pH 2.5 approximately (without any kind of pH adjustment). Based on SEA theory, this pH would be close to optimal for a final pH of maximum adsorption after contact with the support. This may have caused a charge enhanced impregnation which yielded considerably smaller particles compared to other DI prepared catalysts. This same principle may then apply for the XC72-CPA catalysts as well.

Based on the lack of precise results from the XRD performed on the Al2O3-CPA-DI samples, the XRD analysis of the Al2O3-PdTC-DI samples was not performed on all samples. From the few XRD analysis performed, no peaks for Pd where seen. Nevertheless, a weak peak at $2\theta = 31.7^{o}$ was seen which corresponds to PdO. Interestingly, the presence of PdO was detected in the XC72-PdTC-DI samples which will be explained in detail in the next section.

The evaluation of STEM particle size analysis is summarized in Table 4.7. The now familiar pattern of larger average particle sizes at higher reduction temperatures is found as well. A slight increase in clustering index can also be noticed as the heating rates rise.

Table 4.7 STEM particle size analysis for Al2O3-PdTC-DI.

	200°C			**500°C**		
	0.5°C/ min	**2.5°C/ min**	**5.0°C/ min**	**0.5°C/ min**	**2.5°C/ min**	**5.0°C/ min**
<*p*>	3.5	2.1	2.4	4.8	4.9	9.6
n	889	1828	589	943	1869	979
sd	1.7	1.1	2.1	1.9	3.3	2.4
CI	2	2	3	2	3	3

<p> – average particle size, n – number of particles counted, sd – standard deviation, CI – clustering index.

The particle size distributions from Figure 4.15 show increased sintering (wider distributions) for the samples reduced at 500°C compared to the 200°C samples of equivalent heating rate. There also seems to be a noticeable broadening of the distributions for the samples heated at a rate of 5°C/min. As sintering increases, the curves attain more of a PMC mechanism shape especially for the higher heating rates.

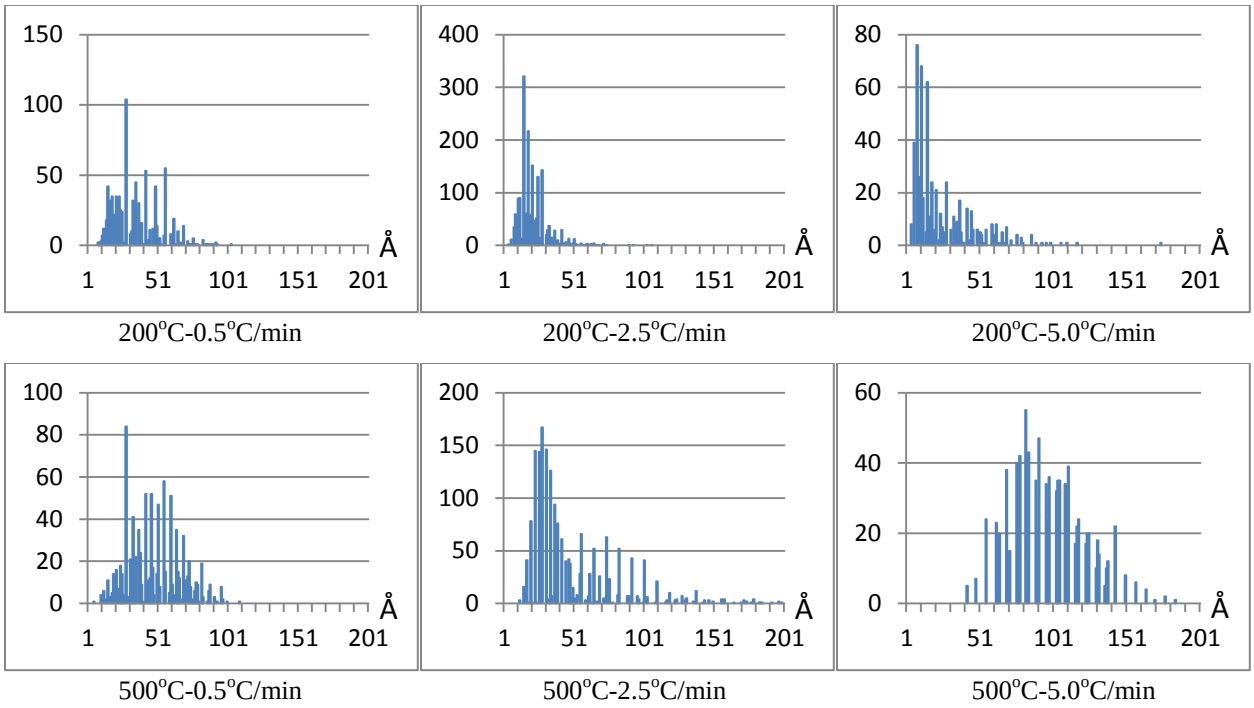

Figure 4.15 Particle size distributions for Al2O3-PdTC-DI catalysts.

These results agree with the outcomes of the previous DI catalysts; a general behavior has been found where higher pretreatment reduction temperatures and increased heating rates increase the average particle sizes of the metal grains.

4.1.5 Catalysts supported on XC72

The CPA solution used for the impregnation of XC72 support had a pH of approximately 2.5 which is very close to the desired initial pH for optimal adsorption in SEA. For this reason the particle sizes in general are very small for what would be expected of DI preparation, as shown in Figure 4.16. Most of the peaks are too wide to make an accurate calculation of the particle

size so the displayed results are approximations (except for the 500°C-5.0°C/min and "water" samples). The highest reduction temperature and heating rate sample (500°C, 5°C/min) showed a considerable increase in particle size which agrees with the general results that higher reduction temperatures and higher heating rates enhance sintering. The water vapor containing sample had severely decreased dispersion as well.

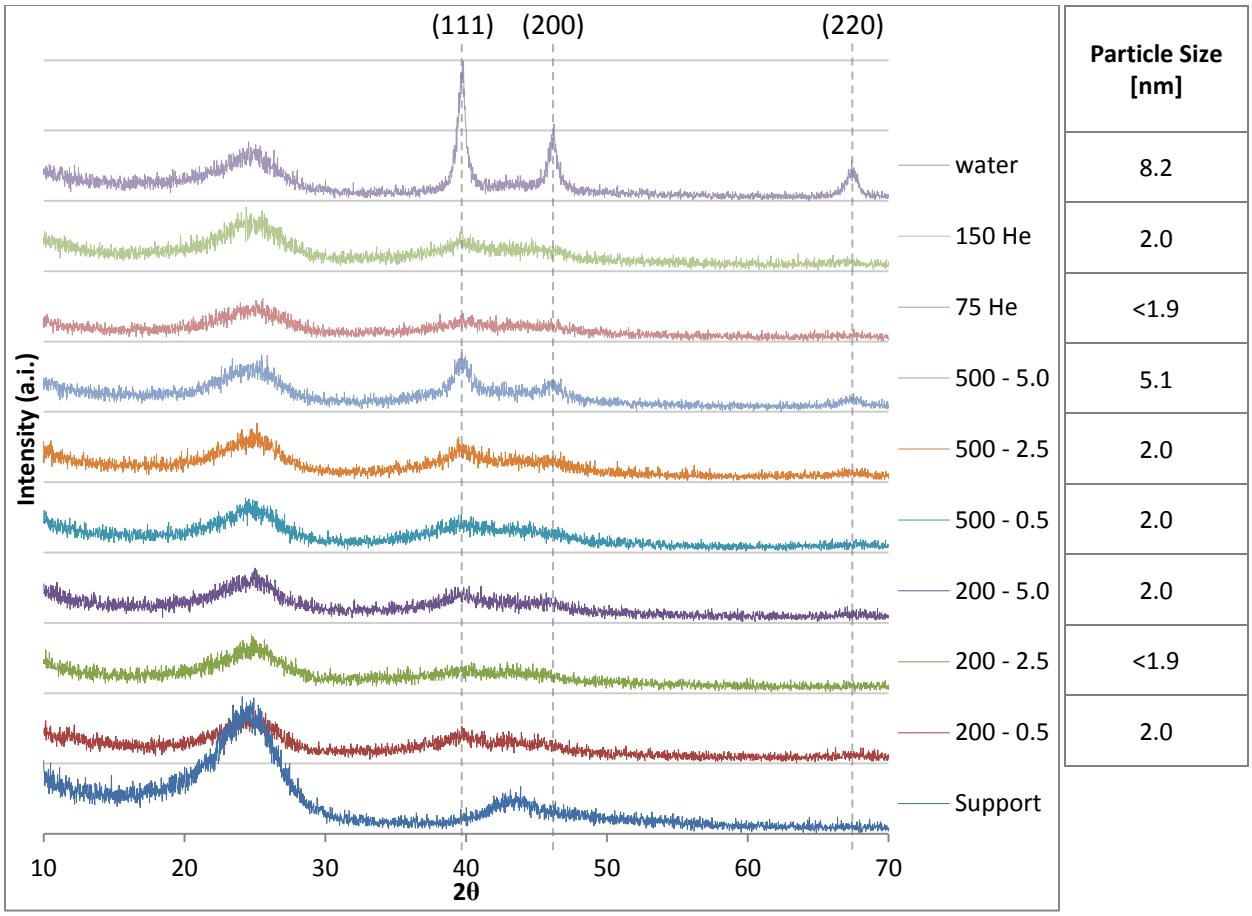

Particle Size [nm]
8.2
2.0
<1.9
5.1
2.0
2.0
2.0
<1.9
2.0

Figure 4.16 XRD results for XC72-CPA-DI.

The STEM average particle sizes of Table 4.8 agree with the XRD results. Most particle sizes appear to be under 2 nm which is the detection limit of XRD. Again a significant increase in particle size can be noticed for the XC72-CPA-DI-500-5.0 and XC72-CPA-DI-water samples. The difference in the particle sizes for these two samples obtained from STEM compared to XRD may occur because XRD is a bulk method which detects signal from the largest crystalline

planes while the smallest ones are undetected. On STEM particle counting, the particles sizes are averaged where each particle, big or small, is given the same burden in the final calculation even though the bigger particles will encompass most of the metal catalyst mass. The standard deviation and clustering index values show how increasing the reduction heating rate favors the formation of larger particles for all samples with a marked increase in sintering for the XC72-CPA-DI-500-5.0 and XC72-CPA-DI-water samples. The advantage of increased evacuation of water and chlorine gases in the two "dry" samples was not as noticeable. Still, the average particle sizes for the two samples reduced in hydrogen and helium are still amongst the smallest of all.

Table 4.8 STEM particle size analysis for XC72-CPA-DI.

	200°C			**500°C**			**200°C at 0.5°C/min**		
	0.5°C/ min	**2.5°C/ min**	**5.0°C/ min**	**0.5°C/ min**	**2.5°C/ min**	**5.0°C/ min**	**75 He**	**150 He**	**water**
<*p*>	1.5	1.3	1.8	1.5	1.5	2.9	1.7	1.7	3.2
n	4871	3936	3192	1014	1023	854	2750	3011	2387
sd	0.67	0.66	1.1	0.49	0.95	3.6	0.68	0.67	3.9
CI	1	1	2	2	2	3	1	1	4

<p> – average particle size, n – number of particles counted, sd – standard deviation, CI – clustering index.

Since in the particle size for most samples is quite small, the particle size distributions from Figure 4.17 are almost equally narrow for all samples with slight widening at the higher heating rates and the water vapor containing sample. Again most of the curves are skewed towards the left while keeping a narrow strip towards the larger particle sizes which is consistent with a PMC type of shape.

A familiar pattern is found in the XRD analysis of Figure 4.18 for the XC72-PdTC-DI catalysts. The set of samples reduced at 500^{o}C is considerably larger than the set reduced at 200^{o}C. There is however a new set of peaks found at 2θ values of 31.7^{o}, 45.4^{o} and 56.5^{o} of about

the same sizes and proportions of the regularly expected peaks for palladium metal in FCC atomic structure. These peaks correspond to PdO [80] where the three peak locations correspond to the (200), (220) and (222) planes respectively. For PdO there should also be another weak peak at $2\theta = 27.4^{o}$ corresponding to the (111) plane which is probably concealed by the support's inherit wide peak at the same location. All these planes ultimately belong to a FCC structure with a lattice parameter of 5.642 Å [80].

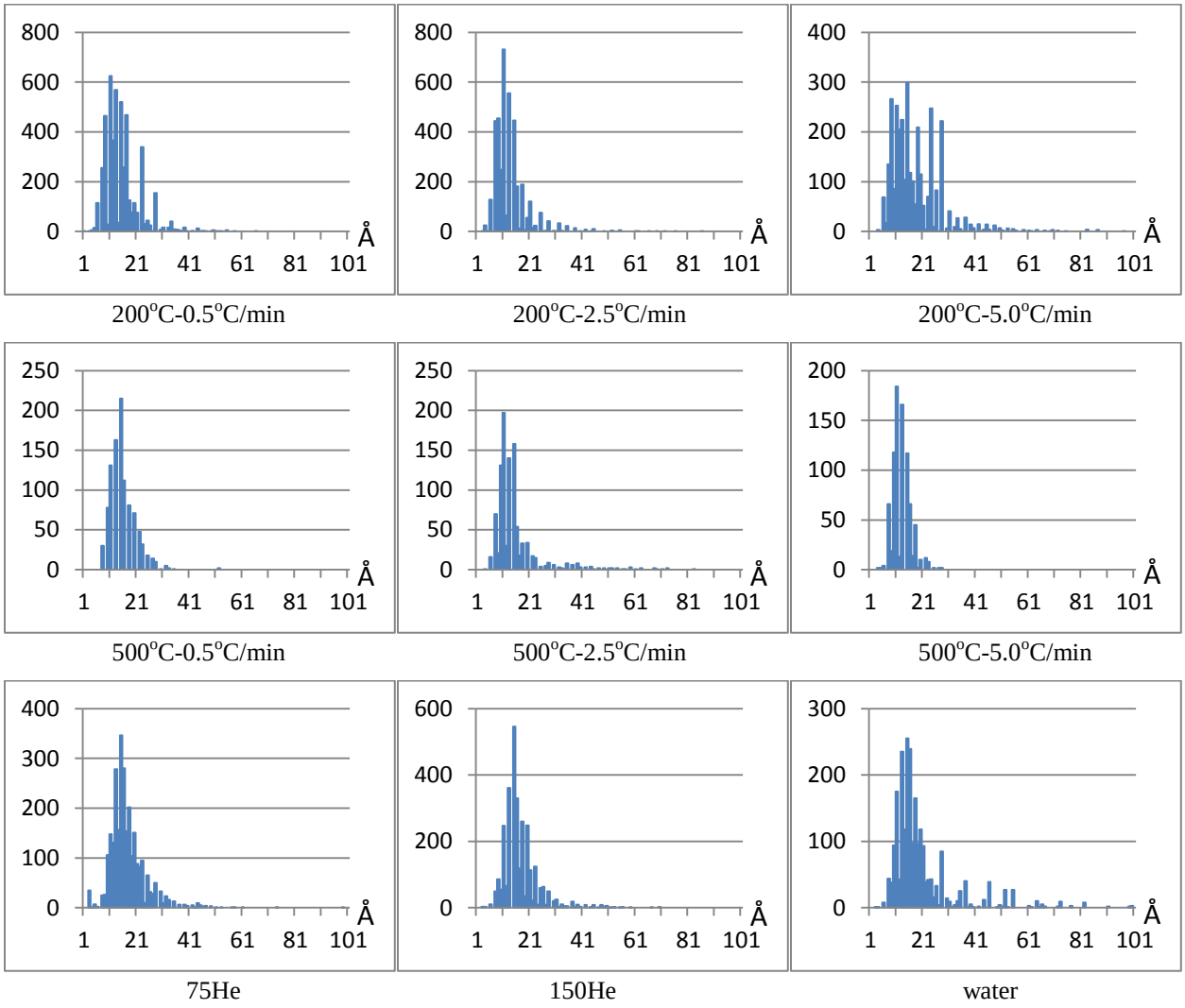

Figure 4.17 Particle size distributions for XC72-CPA-DI catalysts.

It is hard to explain the presence of PdO in this catalyst system; it seems to be found in high concentration regardless of the reduction temperature or heating rate. The presence of PdO was

also mentioned in the Al2O3-PdTC-DI catalysts implying the PdTC precursor tends to facilitate the production of PdO. It is unlikely the Pd got oxidized during the pretreatment reduction so it must have been formed by contact of the fully reduced palladium with air after the reduction in hydrogen flow was completed. Hence, the PdO must be found at the outer crust of the reduced Pd particles which altogether form the particles that can be seen by STEM imaging.

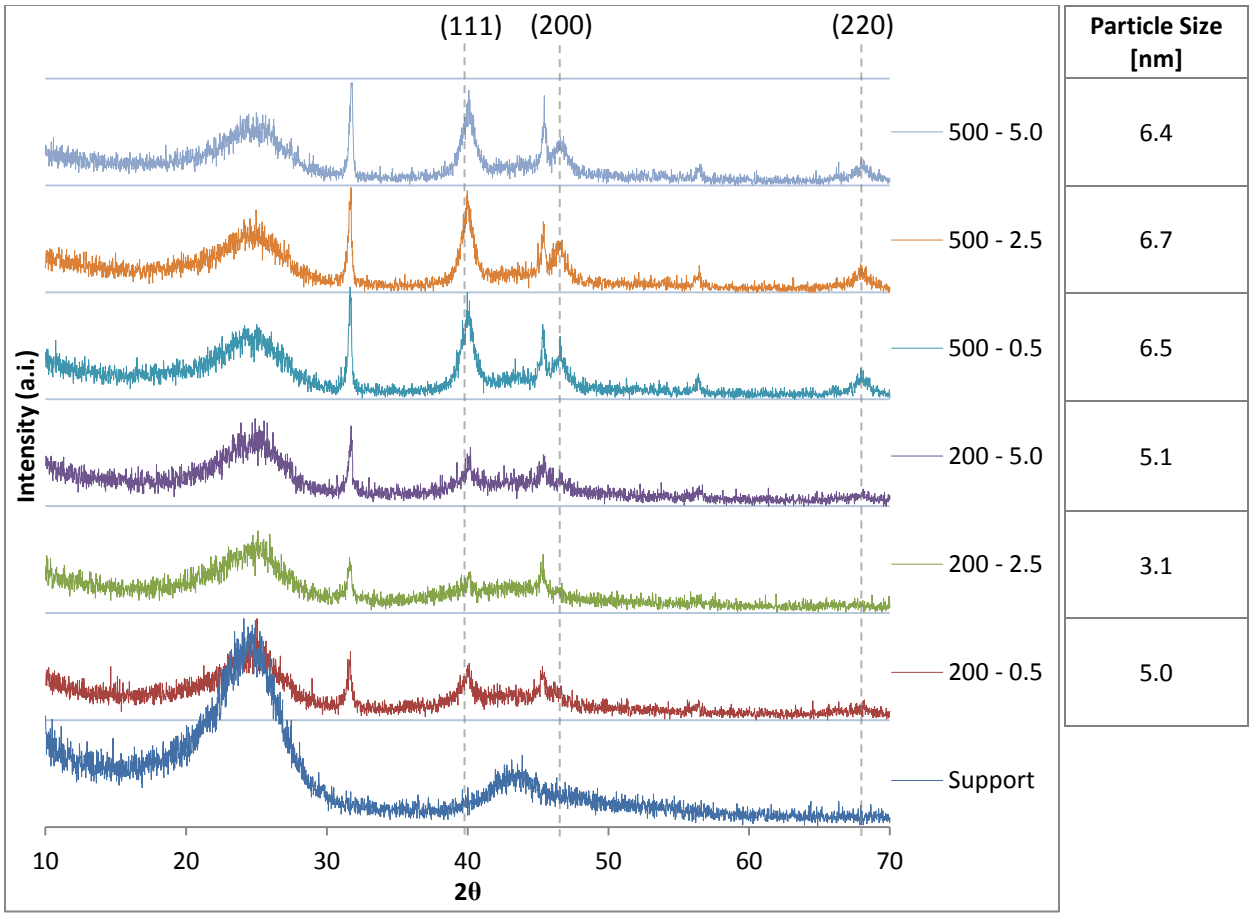

Figure 4.18 XRD results for XC72-PdTC-DI.

The STEM results from Table 4.9 are consistent with XRD. A considerable increase in average particle size is again seen for the samples reduced at higher temperature. It seems however the smallest particles of the 500°C set where produced by the higher heating rate. Pd and PdO particles are not discernible by STEM imaging so these average particle sizes and the particle size distributions from Figure 4.19 must belong to Pd covered by PdO particles. The

particle size distributions mostly show a PMC type of shape and a consistent widening of the curves with increasing reduction temperature and heating rate, which has been the most common result so far for all DI prepared catalysts.

Table 4.9 STEM particle size analysis for XC72-PdTC-DI.

	200°C			**500°C**		
	0.5°C/ min	**2.5°C/ min**	**5.0°C/ min**	**0.5°C/ min**	**2.5°C/ min**	**5.0°C/ min**
<*p*>	2.4	2.0	5.4	6.2	6.9	5.6
n	1099	1450	1165	2401	3727	2549
sd	1.3	0.49	4.9	3.2	3.6	2.6
CI	2	1	2	2	3	3

<p> – average particle size, n – number of particles counted, sd – standard deviation, CI – clustering index.

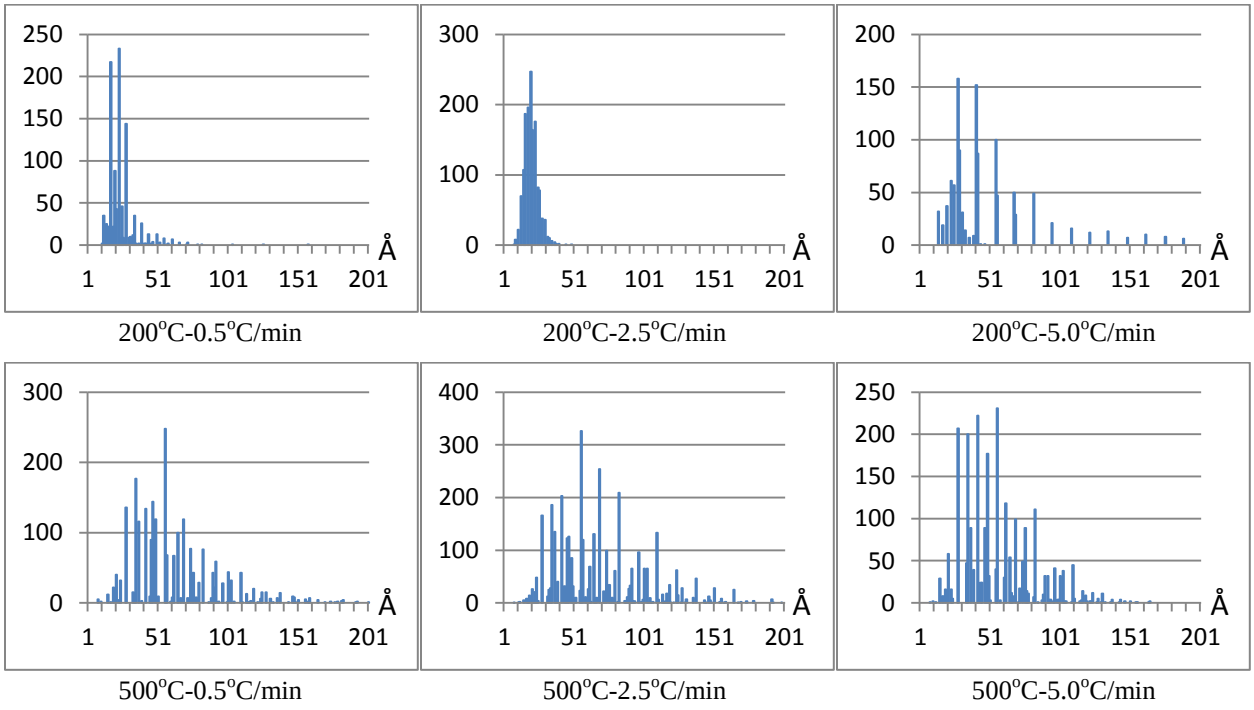

Figure 4.19 Particle size distributions for XC72-PdTC-DI catalysts.

4.2 Catalysts prepared by SEA

Because of the ionic interaction between the metal precursors and the supports, catalysts prepared by SEA produced smaller particles, most of which didn't reveal any results in XRD

analysis. As explained in Section 3.2, the reduction condition where 75 ml/min of helium was introduced into the hydrogen stream during reduction was replaced with a diminished humidity condition where the hydrogen was bubbled through iced water. There were no massive "snowflake" metal formations found in the catalysts prepared by SEA so the Clustering Index used for the previous section will not be required for the particle size analysis of this section. It is important to mention again all SEA prepared catalysts where imaged in a far more advanced STEM instrument than the DI samples, which produced images with a considerably higher level of detail. Some of the new findings in these SEA samples (individual atoms along the surface of the support for instance) doesn't necessarily mean they were not present in the DI catalysts as well, only that they could not be found due to the difference in STEM technology.

4.2.1 Catalysts supported on HSAG300

No peaks where present in the XRD analysis for the HSAG300-PTA-SEA catalyst system probably due to the presence of very small metal particles (< 2 nm) which are below the detection limit of X-Ray Diffraction. This is confirmed by the average particle sizes displayed in Table 4.10 from STEM imaging. The metal particles are quite small, which is expected of an SEA prepared catalyst. For this set of samples the reduction temperature and heating rate didn't have as much of an influence on the average particle size. The "dry" sample on the other hand has the smallest average particle size as well as the lowest standard deviation. As anticipated, the presence of water increases sintering demonstrated not only by the higher average particle size, but also the larger standard deviation. The particle size distributions from Figure 4.20 show there is no noticeable widening of the curves throughout the different heating rates or reduction temperatures. There is a slight increase in the width of the distribution curves for the two "humid" samples, once again indicating the influence water has.

Table 4.10 STEM particle size analysis for HSAG300-PTA-SEA.

	200°C			500°C			200°C at 0.5°C/min		
	0.5°C/ min	**2.5°C/ min**	**5.0°C/ min**	**0.5°C/ min**	**2.5°C/ min**	**5.0°C/ min**	**150 He**	**ice**	**water**
<*p*>	1.3	1.5	1.5	1.4	1.3	1.4	1.1	1.4	1.7
n	1021	1116	998	1127	1127	1235	1055	1158	1048
sd	0.30	0.36	0.35	0.34	0.34	0.34	0.28	0.38	0.45

<p> – average particle size, n – number of particles counted, sd – standard deviation.

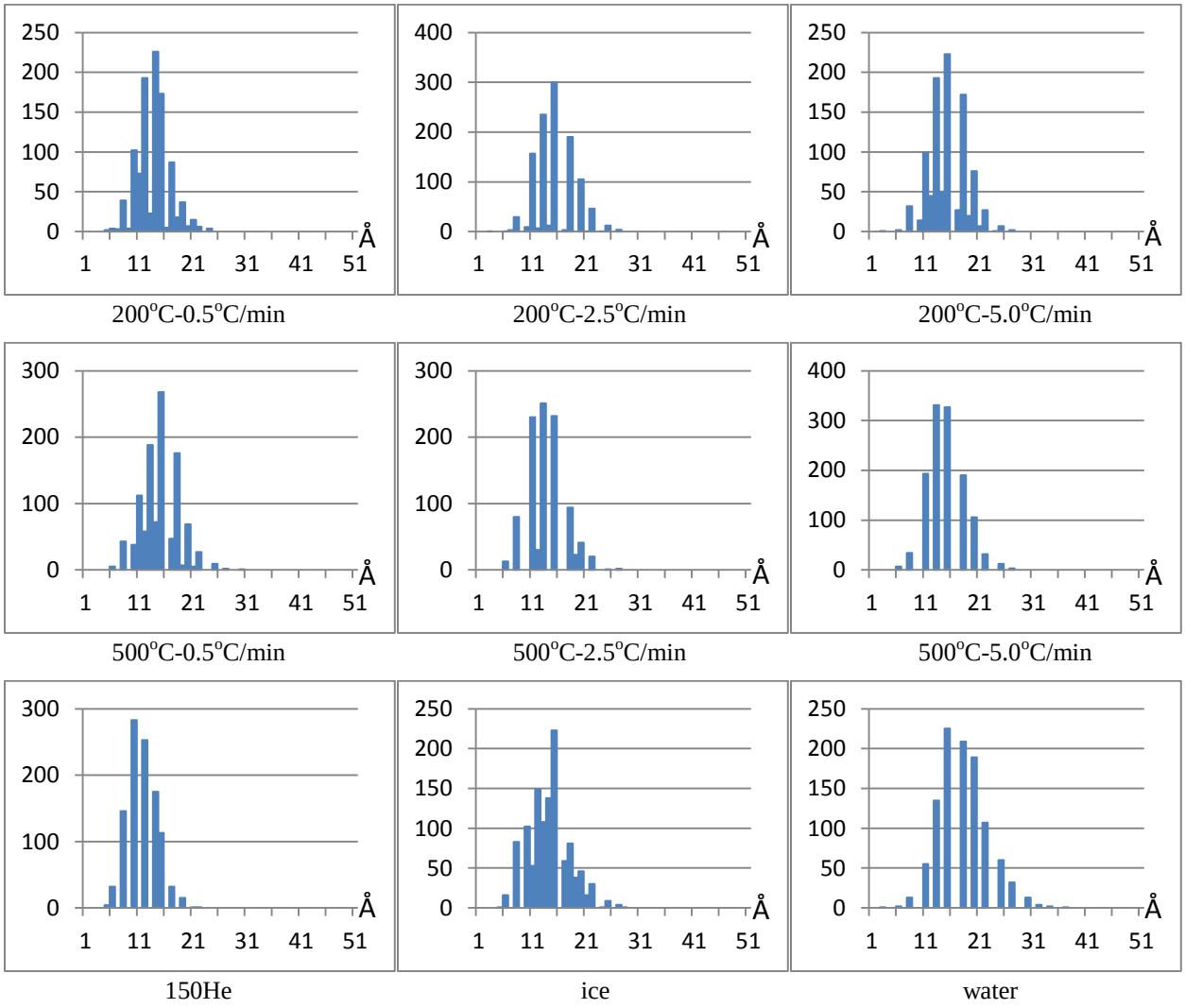

Figure 4.20 Particle size distributions for HSAG300-PTA-SEA catalysts.

Contrary to previous findings for the DI prepared samples, these curves seem quite symmetrical and no clear sintering mechanism seems to have taken place. Since in general these

particles are very small and the metal catalyst has only suffered the first stages of sintering, both sintering mechanisms could be happening at the same time. The STEM images displayed in Figure 4.21 show interesting results. The most important feature that can be noticed is the presence of individual platinum atoms along the surface of the carbon support.

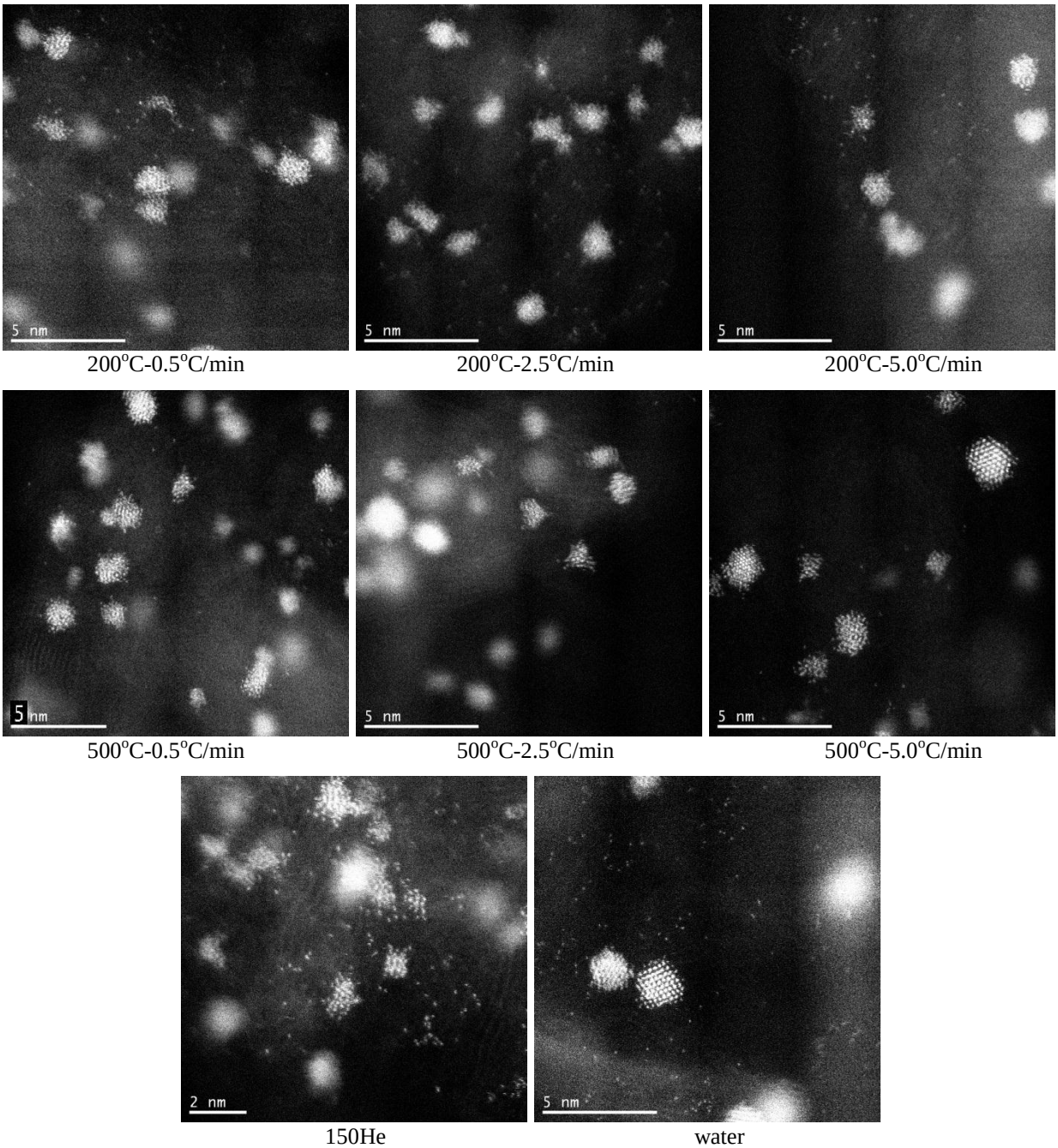

Figure 4.21 STEM images for HSAG300-PTA-SEA catalysts showing the presence of individual atoms.

It is not clear from these images whether these atoms are "unsintered" remains of the original precursor monolayer, or if they are mobile atoms migrating towards larger particles. Should the second case be true, this would draw a strong argument in favor of an OR sintering mechanism taking place. Proving the origin of these isolated atoms is beyond the scope of this research thesis. Further analysis of Figure 4.21 shows another interesting result. It seems individual atoms are not as common for all three samples reduced at 500^{o}C as they are in the first three samples reduced at 200^{o}C, the "dry" sample, or even the "humid" sample (which was reduced at 200^{o}C, 0.5^{o}C/min as well). Remarkably, the HSAG300-PTA-SEA-water sample shows roughly the same density of individual atoms as the set of samples reduced at 200^{o}C. No clear influence of the heating rate is seen on the presence of individual atoms. This implies for this catalyst system, reduction temperature plays a more crucial role in the sintering of individual atoms than heating rate or even water vapor during pretreatment.

The results of the XRD analysis for the HSAG300-PdTA-SEA catalysts are displayed in Figure 4.22. It can be noticed right away how the set of samples reduced at a higher temperature show peaks while the set of lower reduction temperature remain below the detection limit of XRD. From these results, the heating rate doesn't have a profound influence over the extent of sintering of the palladium.

The STEM imaging results are exhibited in Table 4.11. Most of the values are in accordance with the XRD results except for the HSAG300-PdTA-SEA-200-5.0 sample which resulted in a higher average particle size. This might be once again the case where, even though the particles sintered and clustered together to form visually larger bunches, the actual crystallite planes of the metal (which are detected by XRD) did not grow.

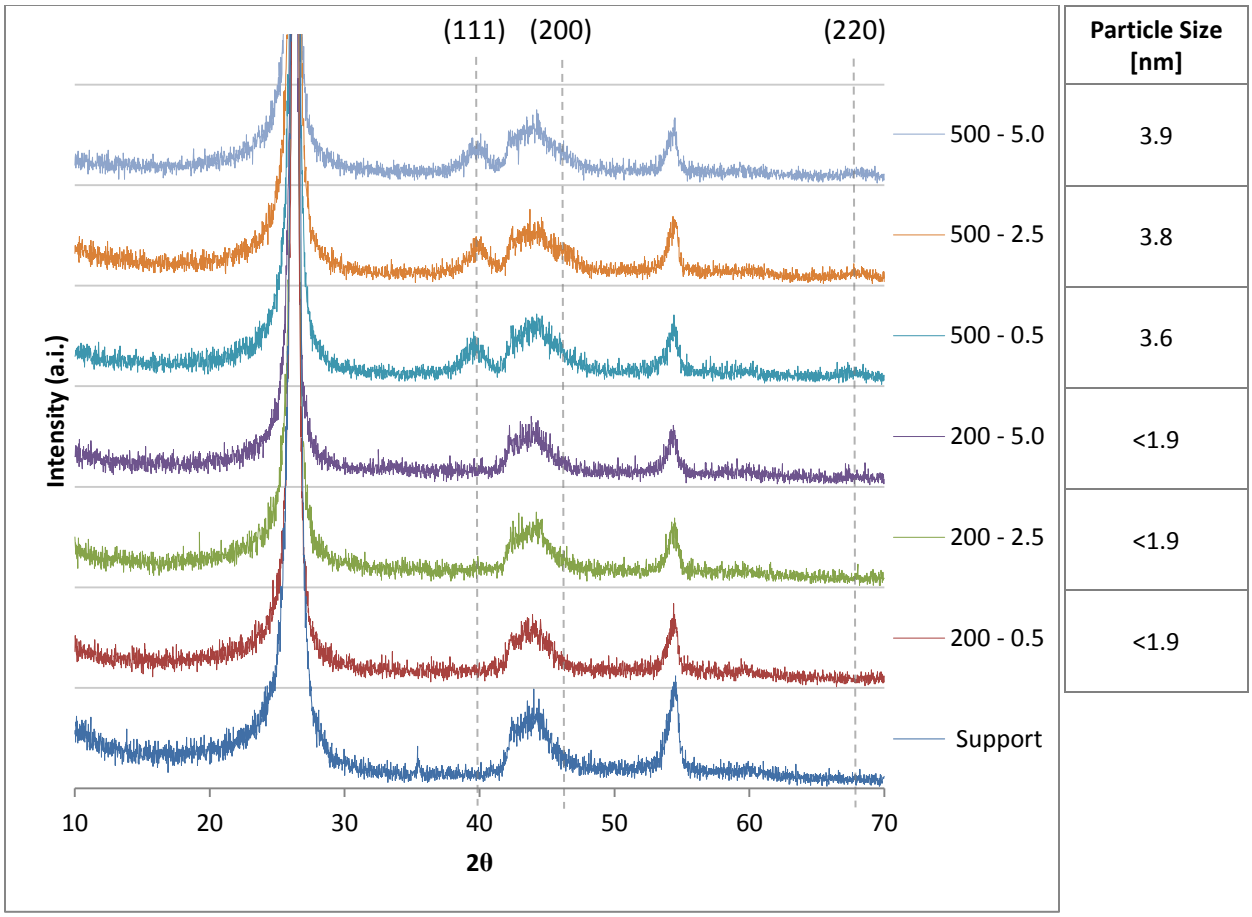

Figure 4.22 XRD results for HSAG300-PdTA-SEA.

Table 4.11 STEM particle size analysis for HSAG300-PdTA-SEA.

	200°C			**500°C**		
	0.5°C/ min	**2.5°C/ min**	**5.0°C/ min**	**0.5°C/ min**	**2.5°C/ min**	**5.0°C/ min**
<*p*>	1.6	1.4	2.5	4.6	4.5	4.0
n	1050	996	985	1061	1021	1097
sd	0.53	0.35	0.79	1.2	1.4	1.3

<p> – average particle size, n – number of particles counted, sd – standard deviation.

For the set of samples reduced at 500°C it seems that the lower heating rates actually acted against the dispersion of the metal. This pattern was seen in the XC72-PdTC-DI catalysts, which is a carbon-palladium catalyst as well. Looking back at the STEM analysis of the HSAG300-PdTA-DI catalysts, the 2.5°C/min heating rate, for both 200°C and 500°C reduction temperatures

yielded the largest metal particles of their corresponding group. An unexpected patter seems to be appearing where moderate and low heating rates actually hurt the dispersion of the Pd deposited on carbon.

The particle size distributions from Figure 4.23 appear as expected, displaying narrower curves for the samples reduced at lower temperature. The curves appear rather symmetrical not evidencing any sintering mechanism in particular.

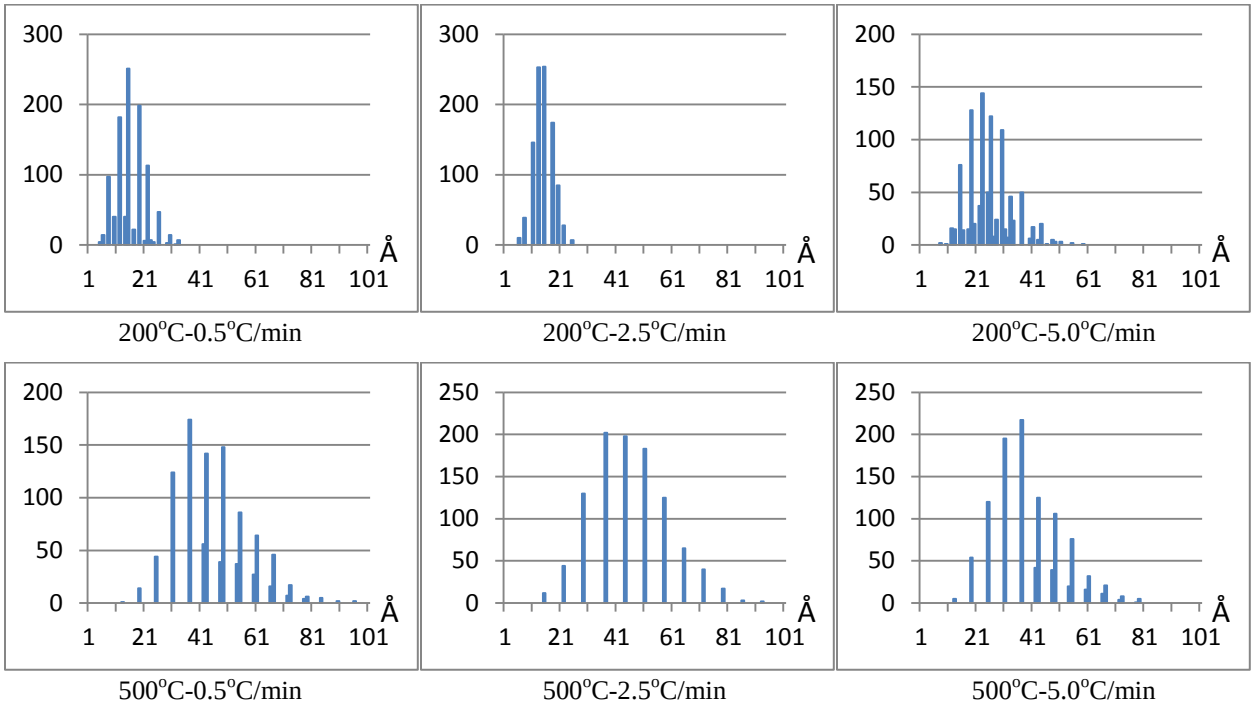

Figure 4.23 Particle size distributions for HSAG300-PdTA-SEA catalysts.

Palladium individual atoms where not observed in the support's surface. It is unclear whether the atoms where not noticeable due to the lower contrast and smaller atom size of the palladium, or they were simply not there. It is noteworthy that such powerful electron microscope as the JEOL JEM-ARM200CF has a very high intensity beam which produces high static in the support's surface and attracts considerable contamination to the area being scanned specially at high magnifications. For this reason, lower contrast atoms like palladium could not be clearly and consistently imaged for some palladium impregnated catalysts.

4.2.2 Catalysts supported on SiO2

XRD analysis for the SiO2-PTA-SEA catalysts didn't show any peaks for any of the pretreatment conditions implying the grain sizes are less than 2 nm. This is confirmed by the particle counting performed on the STEM images, the results are displayed in Table 4.12. For this catalyst the higher heating rates didn't increase the average particle size or the standard deviation, as was the case for the SiO2-PTA-DI samples. The average particle sizes of the samples reduced at 500^{o}C are larger than, or equal to, their same-heating-rate counterpart reduced at 200^{o}C, a common trait for most of the catalysts. Another consistency found is the "dry" sample is the smallest, with the lowest standard deviation as well. Finally the "humid" sample is the largest reiterating the influence of water vapor.

Table 4.12 STEM particle size analysis for SiO2-PTA-SEA.

	200°C			**500°C**			**200°C at 0.5°C/min**		
	0.5°C/ min	**2.5°C/ min**	**5.0°C/ min**	**0.5°C/ min**	**2.5°C/ min**	**5.0°C/ min**	**150 He**	**ice**	**water**
<*p*>	0.94	1.2	0.94	1.4	1.2	1.1	0.82	1.2	1.3
n	1062	1202	1209	907	1047	1133	1024	1055	1231
sd	0.43	0.78	0.37	0.70	0.57	0.49	0.24	0.42	1.18

<p> – average particle size, n – number of particles counted, sd – standard deviation.

The particle size distributions from Figure 4.24 demonstrate once again how the increased evacuation of water vapor and other gases during pretreatment reduction by introducing helium into the hydrogen stream yields the narrowest particle size distribution (sample SiO2-PTA-SEA-150He). The water containing sample shows a peculiar particle size distribution. Most of the curves present a PMC type of shape, most noticeably in the 500^{o}C reduction temperature set. The SiO2-PTA-SEA-ice sample doesn't show any extreme sintering pattern meaning low concentrations of water vapor in the hydrogen stream is not as harmful and had even less influence than the actual reduction temperature.

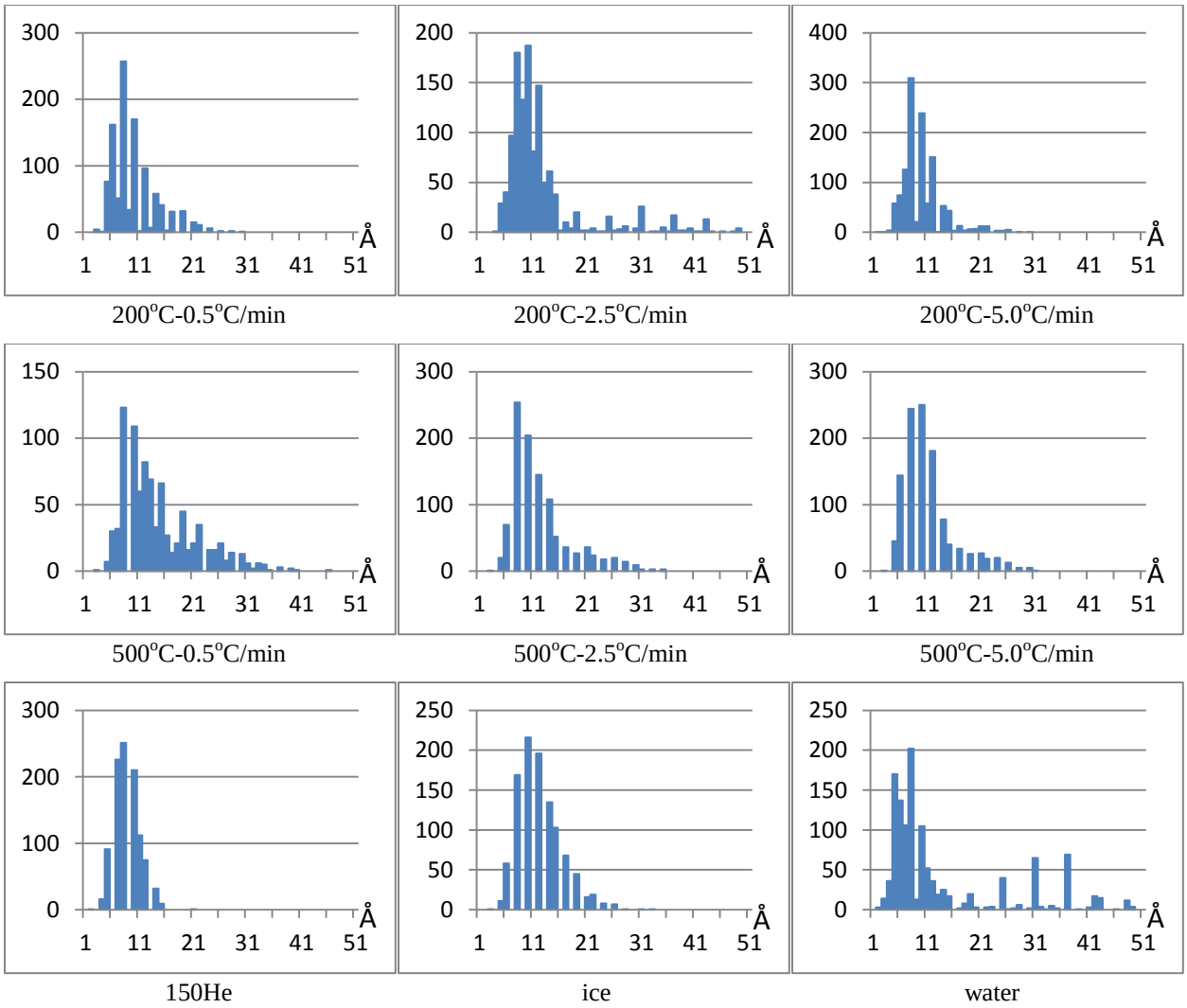

Figure 4.24 Particle size distributions for SiO2-PTA-SEA catalysts.

No catalyst peaks where seen in the XRD plots for the SiO2-PdTA-SEA catalyst samples. The results from STEM imaging are shown in Table 4.13. A steady almost linear increase of average particle size with augmenting heating rate can be observed. A slightly different patter can be noticed for the standard deviation values where both 2.5°C/min heating rates had the smaller standard deviation of their reduction temperature groups, something also seen in the HSAG300-PdTA-SEA-200 set of samples.

Table 4.13 STEM particle size analysis for SiO2-PdTA-SEA.

	200°C			500°C		
	0.5°C/ min	**2.5°C/ min**	**5.0°C/ min**	**0.5°C/ min**	**2.5°C/ min**	**5.0°C/ min**
<*p*>	1.2	1.3	1.5	1.2	1.3	1.4
n	1222	1069	1042	1175	964	1089
sd	0.48	0.44	0.81	0.40	0.35	0.42

<p> – average particle size, n – number of particles counted, sd – standard deviation.

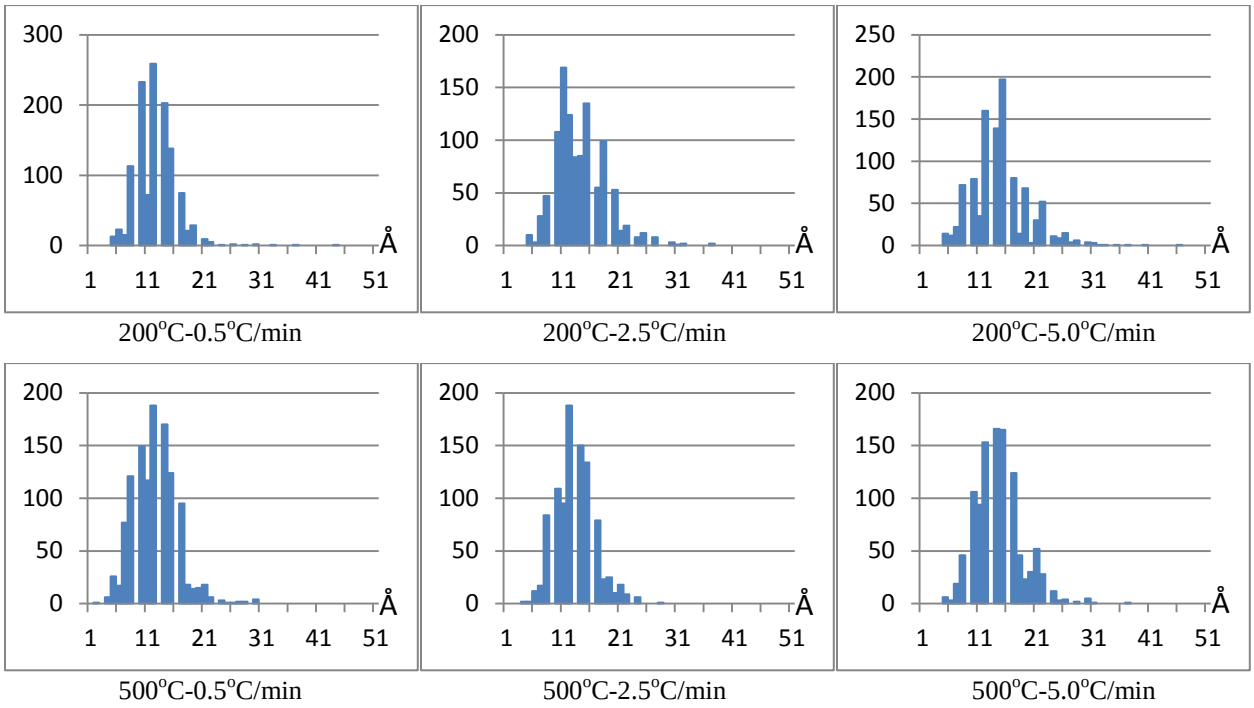

Figure 4.25 Particle size distributions for SiO2-PdTA-SEA catalysts.

The particle size distributions from Figure 4.25 didn't show any remarkable pattern except for a slight widening of the curves at the highest heating rates. The curves are once again symmetrical, not showing enough evidence to favor any particular sintering mechanism.

4.2.3 Catalysts supported on TiO2

Referring back to the XRD analysis of the TiO2-PTA-DI samples from Section 4.1.3, no peaks where seen due to the low concentration of platinum. Since the TiO2-PTA-SEA catalysts are expected to have approximately the same metal concentration but smaller metal particles, the

XRD analysis was carried out only on a few TiO2-PTA-SEA samples. No peaks where seen once again, even for the TiO2-PTA-SEA-water sample.

The results from the STEM particle count in Table 4.14 show almost no variation of the average particle sizes for the temperature trials. The "dry" sample yielded once again the smallest average particle size of all. Increasing humidity conditions impacted metal sintering more significantly. The standard deviation of the samples closely mirrors the average particle size patterns.

Table 4.14 STEM particle size analysis for TiO2-PTA-SEA.

	200°C			**500°C**			**200°C at 0.5°C/min**		
	0.5°C/ min	**2.5°C/ min**	**5.0°C/ min**	**0.5°C/ min**	**2.5°C/ min**	**5.0°C/ min**	**150 He**	**ice**	**water**
<p>	1.2	1.1	1.3	1.1	1.2	1.2	1.0	1.7	1.9
n	1071	1010	1080	1042	990	1069	1002	758	869
sd	0.32	0.32	0.38	0.32	0.30	0.28	0.25	0.60	1.21

<p> – average particle size, n – number of particles counted, sd – standard deviation.

Most of the particle size distribution curves from Figure 4.26 appear symmetrical once again except for the two humidity trials where the curves widened and started showing a slight PMC sintering shape. Agreeing with the data from Table 4.14, the particle size distributions weren't too affected by the varying reduction temperature and heating rate conditions and the "dry" sample definitely produced the narrowest curve. The amount of water vapor introduced into the hydrogen stream during reduction affected the extent of sintering of the platinum particles proportionally. The atomic resolution images obtained from a few samples of the TiO2-PTA-SEA catalysts didn't reveal the presence of individual atoms along the surface of the support or any other notable information.

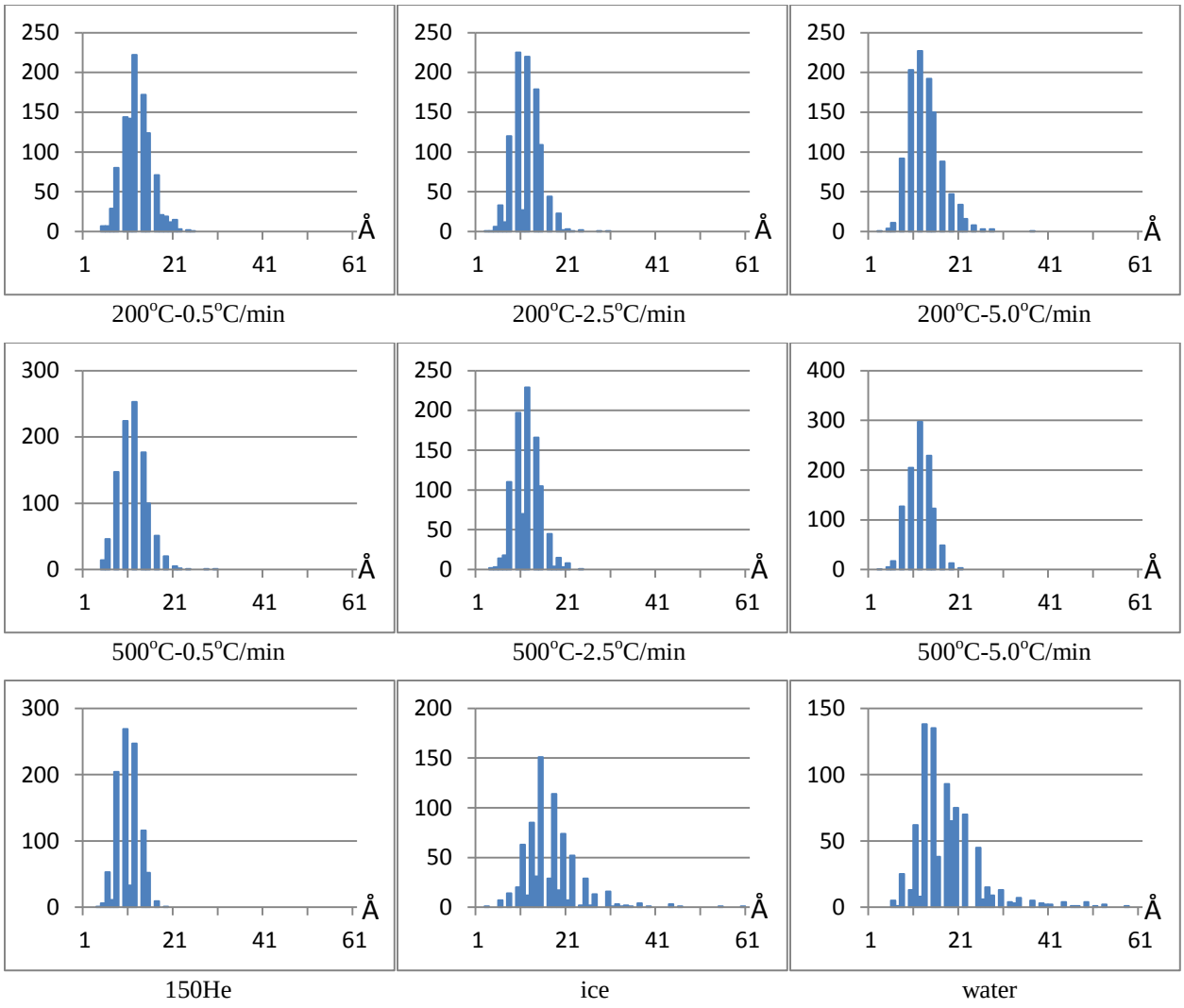

Figure 4.26 Particle size distributions for TiO2-PTA-SEA catalysts.

Unfortunately, no information could be obtained from the titania-palladium catalysts. The very low palladium loading made XRD analysis unsuccessful. The fact that there is not enough difference between titanium's and palladium's molecular weight made STEM imaging difficult because of the reduced contrast. The low palladium loading also made the palladium particles very scarce. Even though a few metal particles were found, there were not enough of them for a reliable particle count.

4.2.4 Catalysts supported on Al2O3

Only the Al2O3-CPA-SEA-500-5.0 sample shows a slight peak in the XRD plot from Figure 4.27. It appears reduction temperature was more critical to the final particle size than presence of water vapor during pretreatment reduction.

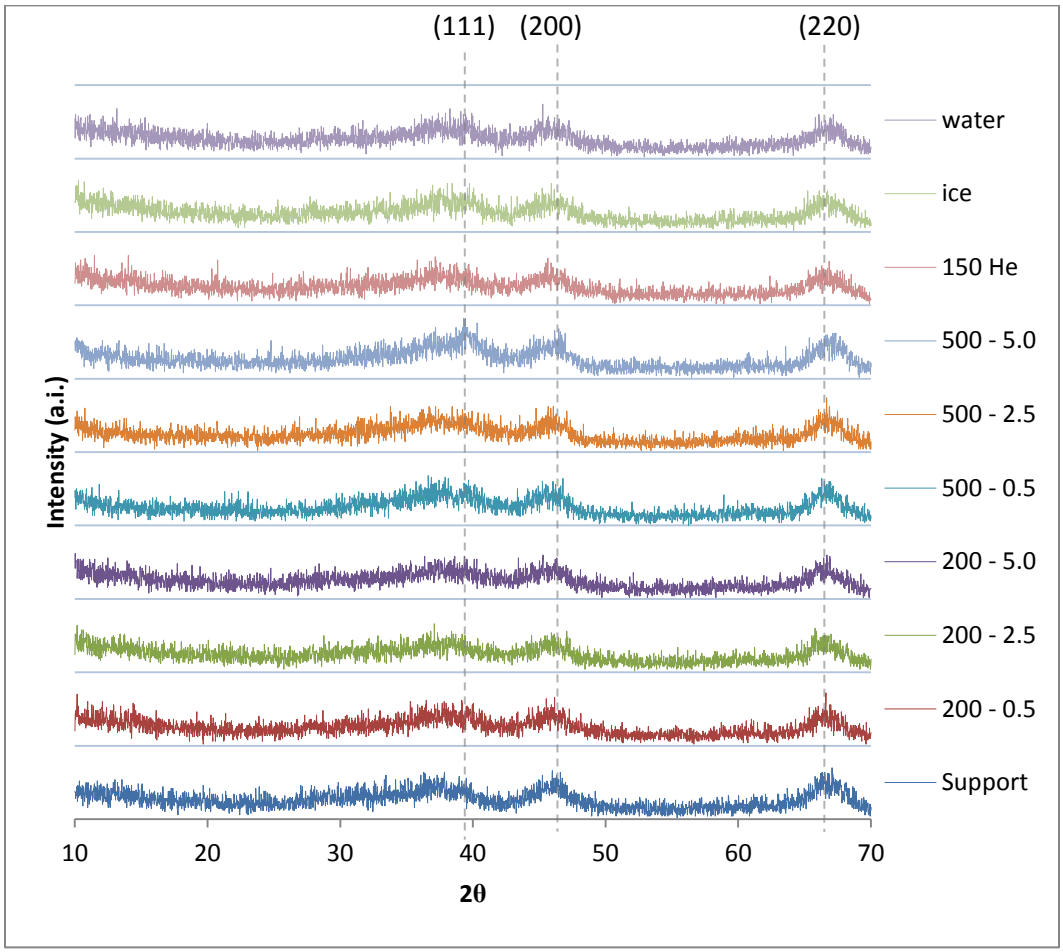

Particle Size [nm]
<1.9
<1.9
<1.9
2.0
<1.9
<1.9
<1.9
<1.9
<1.9

Figure 4.27 XRD results for Al2O3-CPA-SEA.

STEM imaging data from Table 4.15 confirms all the average particle sizes are below 2 nm. When comparing the samples reduced at the same heating rates but at different reduction temperature, all of the samples reduced at 500^{o}C are bigger than their 200^{o}C counterpart. The 2.5^{o}C/min heating rate samples yielded the smallest particle size of their corresponding group. Results also indicate temperature conditions play a more important role than humidity in

determining the final particle size. The standard deviation values mostly follow the average particle size pattern.

Table 4.15 STEM particle size analysis for Al2O3-CPA-SEA.

	200°C			**500°C**			**200°C at 0.5°C/min**		
	0.5°C/ min	**2.5°C/ min**	**5.0°C/ min**	**0.5°C/ min**	**2.5°C/ min**	**5.0°C/ min**	**150 He**	**ice**	**water**
<*p*>	1.0	0.92	1.2	1.2	1.1	1.5	0.94	1.2	1.1
n	895	877	965	1132	933	1099	1097	920	1046
sd	0.33	0.33	0.41	0.39	0.39	0.56	0.34	0.44	0.49

<p> – average particle size, n – number of particles counted, sd – standard deviation.

The particle size distributions of Figure 4.28 show a widening of the curves for the highest heating rate samples, acquiring a slight PMC sintering mechanism type of shape even though all the distributions in general seem symmetrical. The "dry" sample returned the narrowest distribution. Humidity introduced into the last two samples produced a slight widening of the distribution curves when compared to the Al2O3-CPA-SEA-200-0.5 sample, but not really having more sintering effect than the rest of conditions.

STEM imaging for these samples revealed the presence of individual platinum atoms throughout the surface of the support for most of the samples. Figure 4.29 shows a sampler of the images obtained. Unfortunately, not the same detail and quality could be obtained for all the samples. Abundant individual atoms where found on all samples reduced at 200^{o}C, including the "reduced humidity", and the "humid" samples. The platinum atoms were less common in the samples reduced at 500^{o}C, although they were present as well. This type of result was also seen in the HSAG300-PTA-SEA catalyst set where the higher reduction temperature significantly reduced the presence of individual atoms and humidity and heating rate didn't have as much influence.

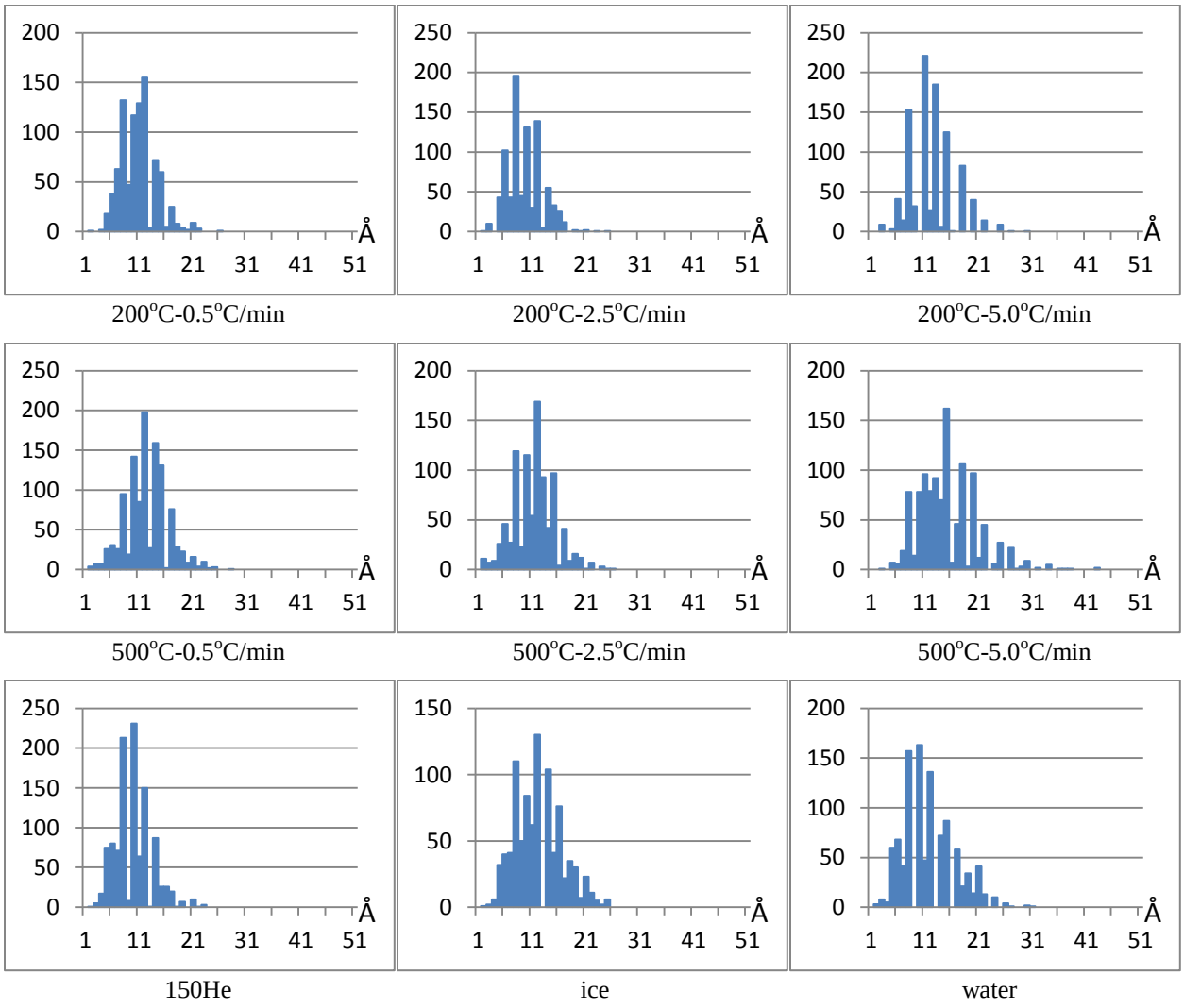

Figure 4.28 Particle size distributions for Al2O3-CPA-SEA catalysts.

The XRD analysis for the palladium-alumina catalysts of Figure 4.30 shows no peaks for the samples reduced at 200°C and a small peak of approximately the same size for the samples reduced at 500°C. From these results it seems the heating rate didn't affect the particle size as much as the reduction temperature did. An exact calculation of the particle sizes from these peaks is hard to achieve because the palladium peaks are deformed by alumina's natural peaks so the displayed values are approximations.

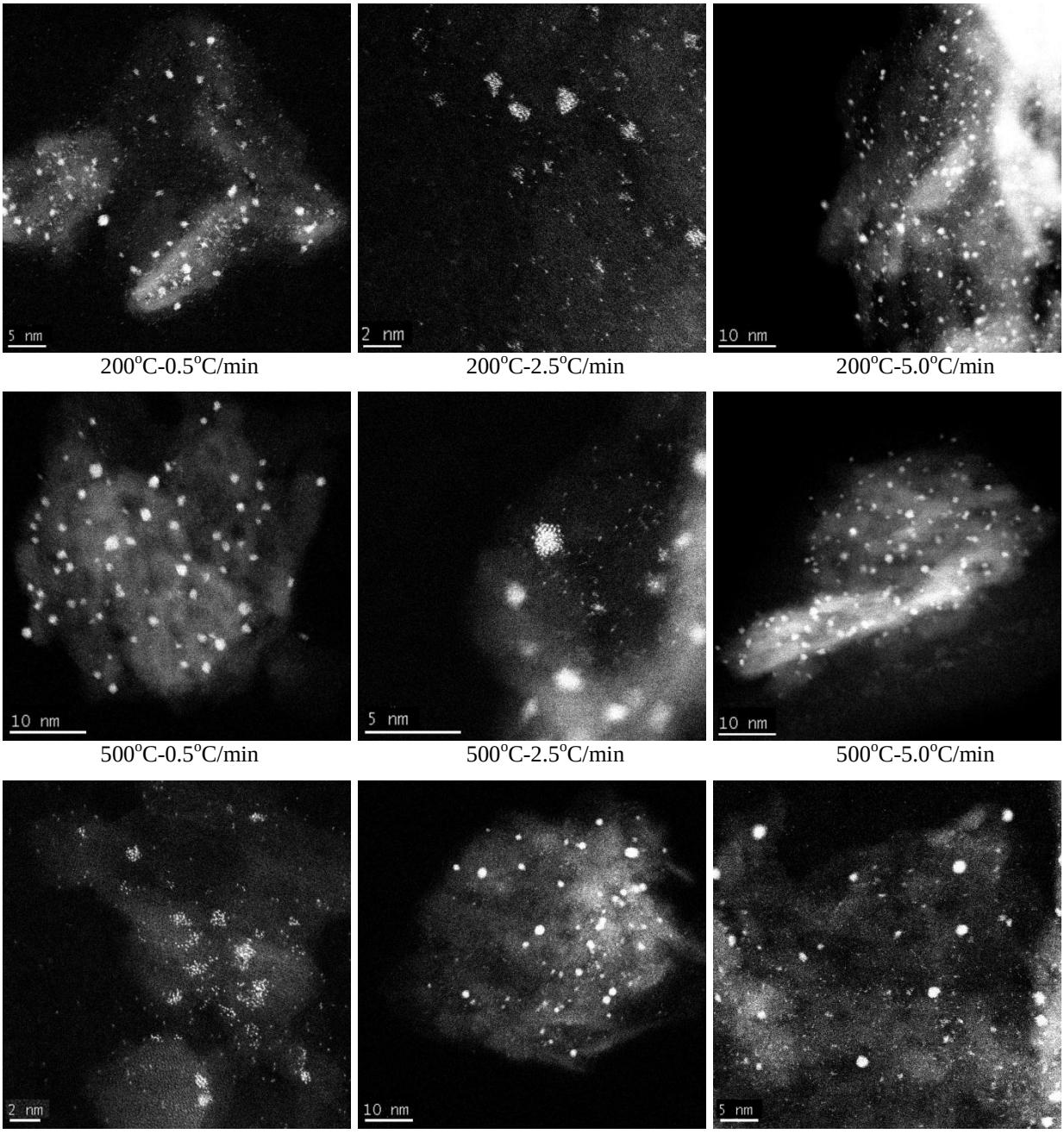

Figure 4.29 STEM images for Al2O3-CPA-SEA catalysts showing the presence of individual atoms.

Table 4.16 shows the results from the particle counting of STEM images obtained for the Al2O3-PdTC-SEA catalysts. The average particle sizes mimic the pattern of those shown in Figure 4.30. The reduction temperature didn't profoundly affect the palladium particle sizes. At the 200°C reduction temperature, the 2.5°C/min heating rate produced the smallest average

particle size and standard deviation. This is a result also seen in the HSAG300-PdTA-SEA, SiO2-PdTA-DI, Al2O3-PdTC-DI, and XC72-PdTC-DI catalysts. It seems palladium benefits the most from a moderate heating rate when it comes to minimizing sintering.

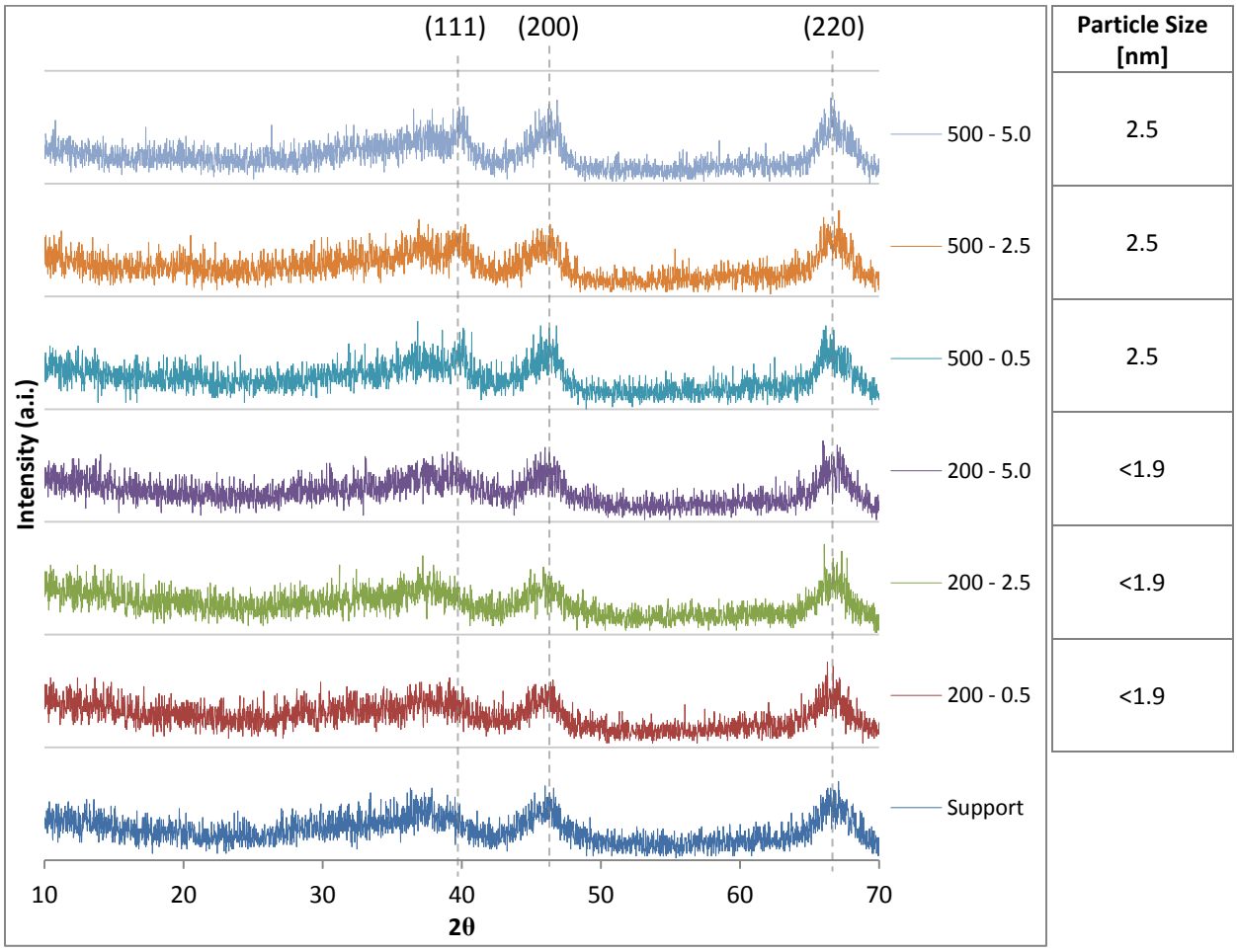

Figure 4.30 XRD results for Al2O3-PdTC-SEA.

Table 4.16 STEM particle size analysis for Al2O3-PdTC-SEA.

	200°C			**500°C**		
	0.5°C/ min	**2.5°C/ min**	**5.0°C/ min**	**0.5°C/ min**	**2.5°C/ min**	**5.0°C/ min**
<*p*>	1.4	0.95	1.3	4.0	4.1	4.1
n	1170	967	1355	1068	976	1073
sd	1.3	0.62	0.91	4.5	1.7	1.8

<p> – average particle size, n – number of particles counted, sd – standard deviation.

The particle size distributions from Figure 4.31 show the Al2O3-PdTC-SEA-200-2.5 sample has the narrowest distribution curve of all. For the samples reduced at 500°C, the increase in heating rate actually helped diminish the widening of the particle size distributions. None of the samples show a shape that would help determine if any particular sintering mechanism had taken place.

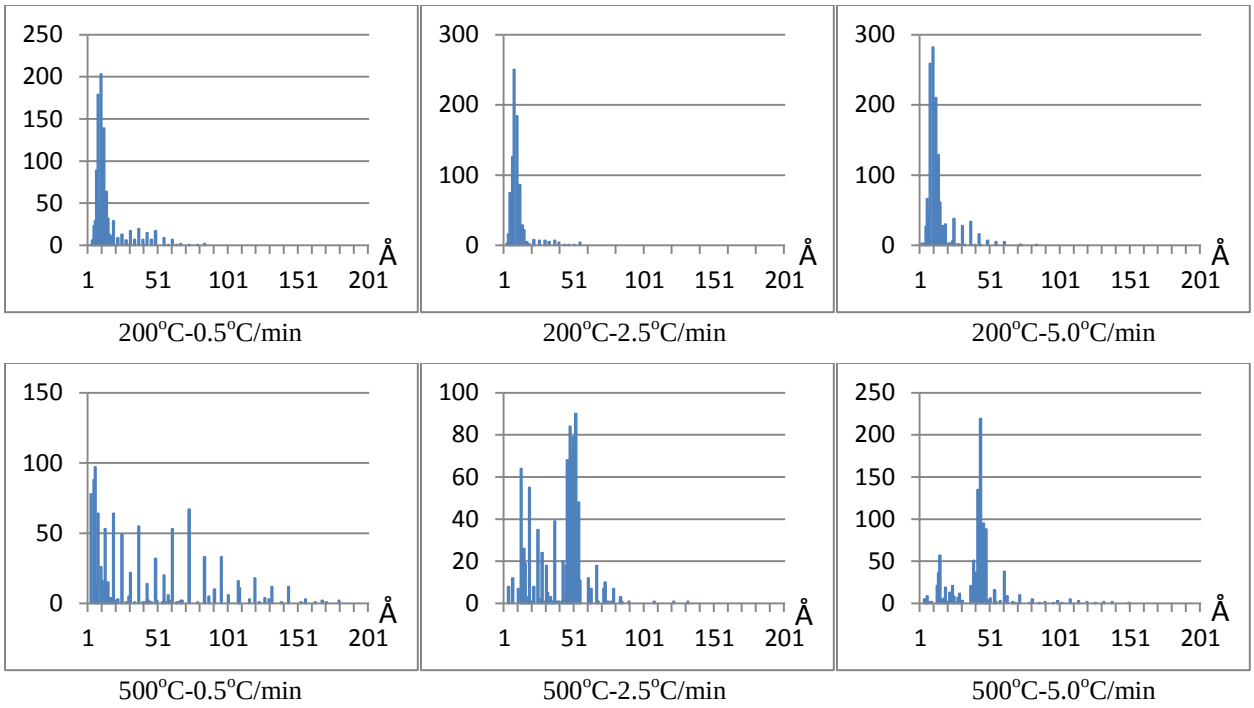

Figure 4.31 Particle size distributions for Al2O3-PdTC-SEA catalysts.

4.2.5 Catalysts supported on XC72

The XRD analysis for the XC72-CPA-SEA catalysts didn't show any peaks for any of the samples across the board except for the XC72-CPA-SEA-water sample which is shown in Figure 4.32 together with the other humidity variation samples. The size difference of the high humidity sample with respect to the rest was not as monumental when looking at the results from the particle size analysis in Table 4.17. This disparity happens because such big particles are usually going to be scarce and are going to reside within the thickest masses of the support. These large particles would also encompass most of the platinum mass. It's possible these huge

particles were not found since STEM imaging only evaluates a small fraction of the support's surface. A wide particle size distribution would be expected if this where the case. Table 4.17 also shows how the samples from the group reduced at 200°C have smaller average particle sizes than the 500°C group. Their standard deviations are lower as well. Humidity is the most important sintering factor for this catalyst set.

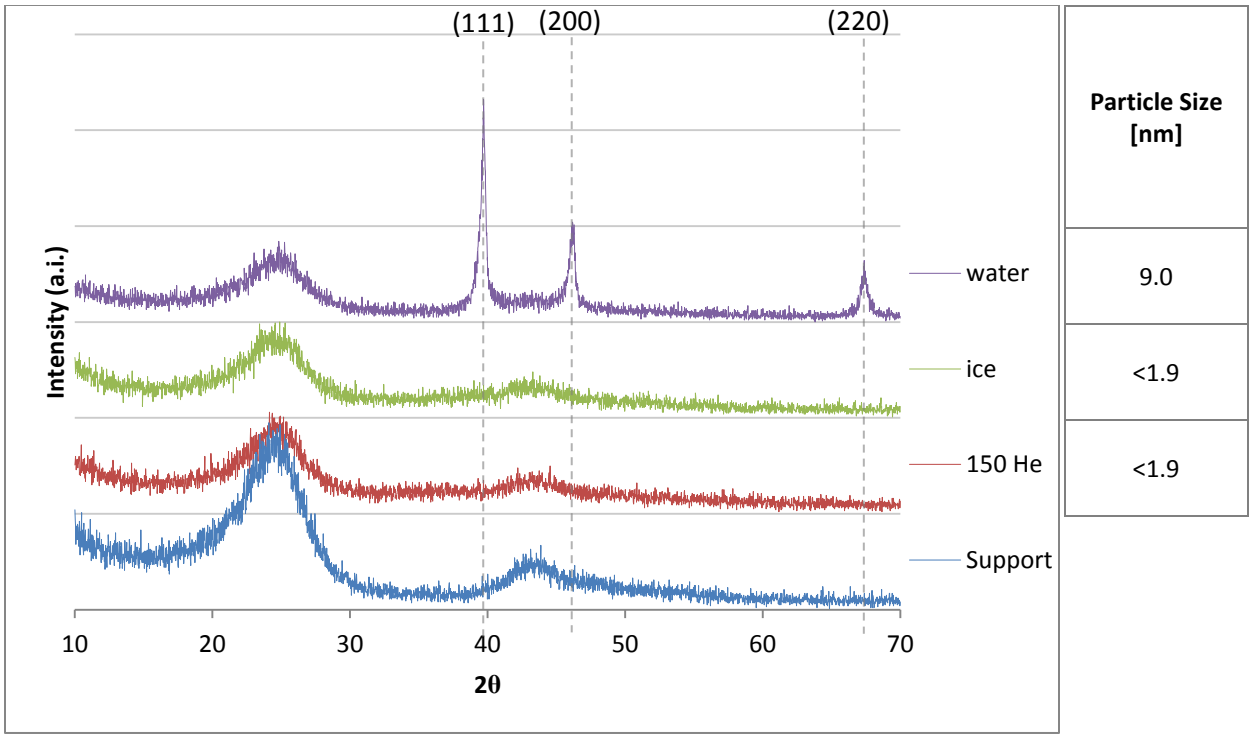

Figure 4.32 XRD results for XC72-CPA-SEA.

Table 4.17 STEM particle size analysis for XC72-CPA-SEA.

	200°C			**500°C**			**200°C at 0.5°C/min**		
	0.5°C/ min	**2.5°C/ min**	**5.0°C/ min**	**0.5°C/ min**	**2.5°C/ min**	**5.0°C/ min**	**150 He**	**ice**	**water**
<*p*>	0.93	0.87	0.95	1.2	1.2	1.3	1.0	1.1	2.5
n	1056	1009	1027	1118	1061	1026	1069	1018	1203
sd	0.23	0.23	0.24	0.35	0.35	0.33	0.29	0.38	2.2

<p> – average particle size, n – number of particles counted, sd – standard deviation.

It can be seen the particle size distribution for the XC72-CPA-SEA-water sample in Figure 4.33 is quite wide as expected. This sample displays a messy distribution which even though is

tilted towards the left and narrowing towards the right doesn't show a PMC sintering mechanism shape. The rest of the curves depict symmetrical shapes not evidencing if a particular sintering mechanism has taken place. The set of samples reduced at 200°C show narrower distribution curves compared to the 500°C set of samples, a common finding by now.

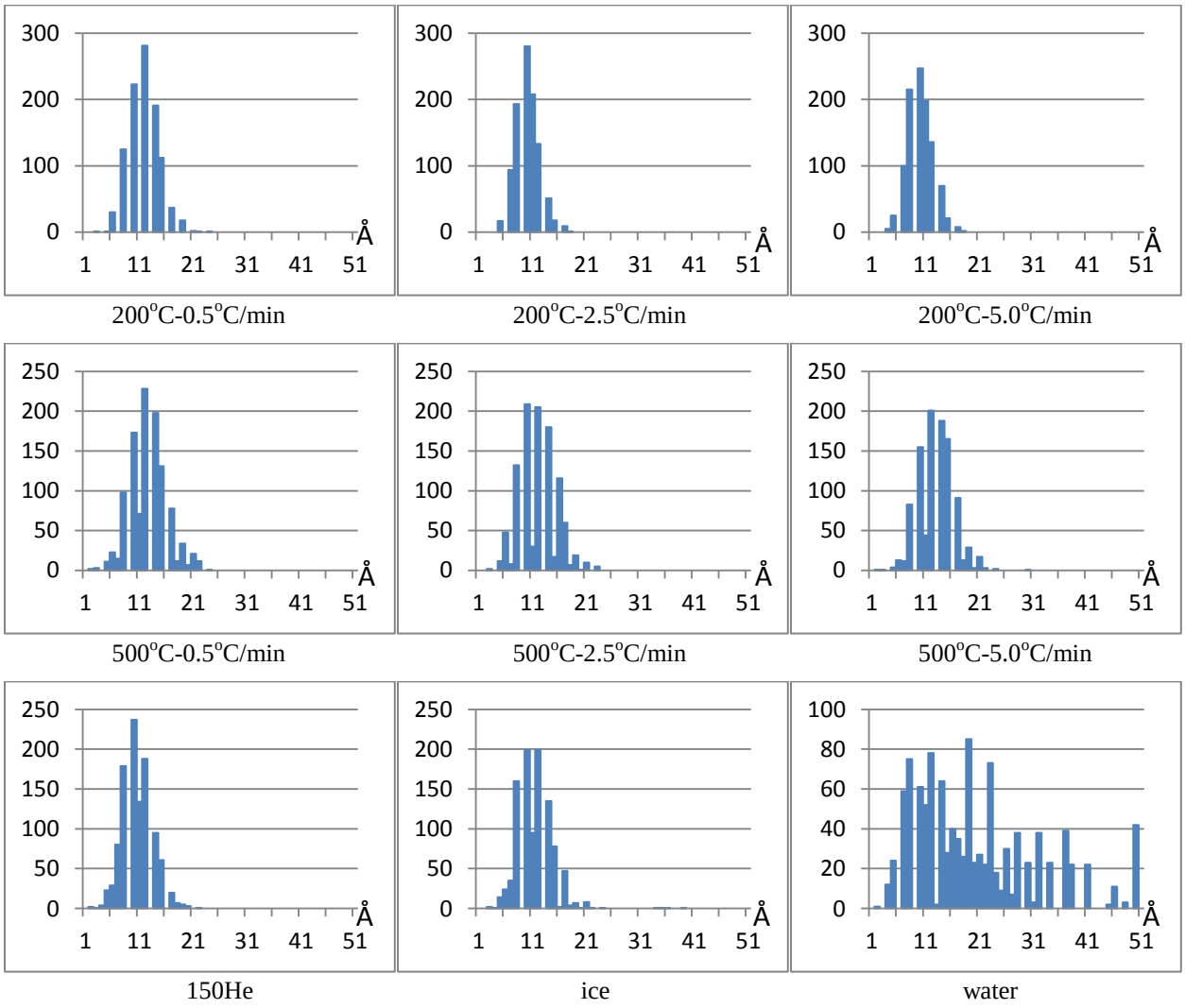

Figure 4.33 Particle size distributions for XC72-CPA-SEA catalysts.

Considering the appearance of the XC72-CPA-SEA-water sample particle size distribution curve, it was expected the XC72-CPA-SEA-ice (reduced humidity) sample would show a higher level of sintering or curve widening than its current state, but it seems to show even less widening than the 500°C set of samples. The STEM images didn't reveal the presence of

individual platinum atoms deposited in the surface of the support. Contamination and static issues also made it difficult to produce atomic resolution images of this catalyst.

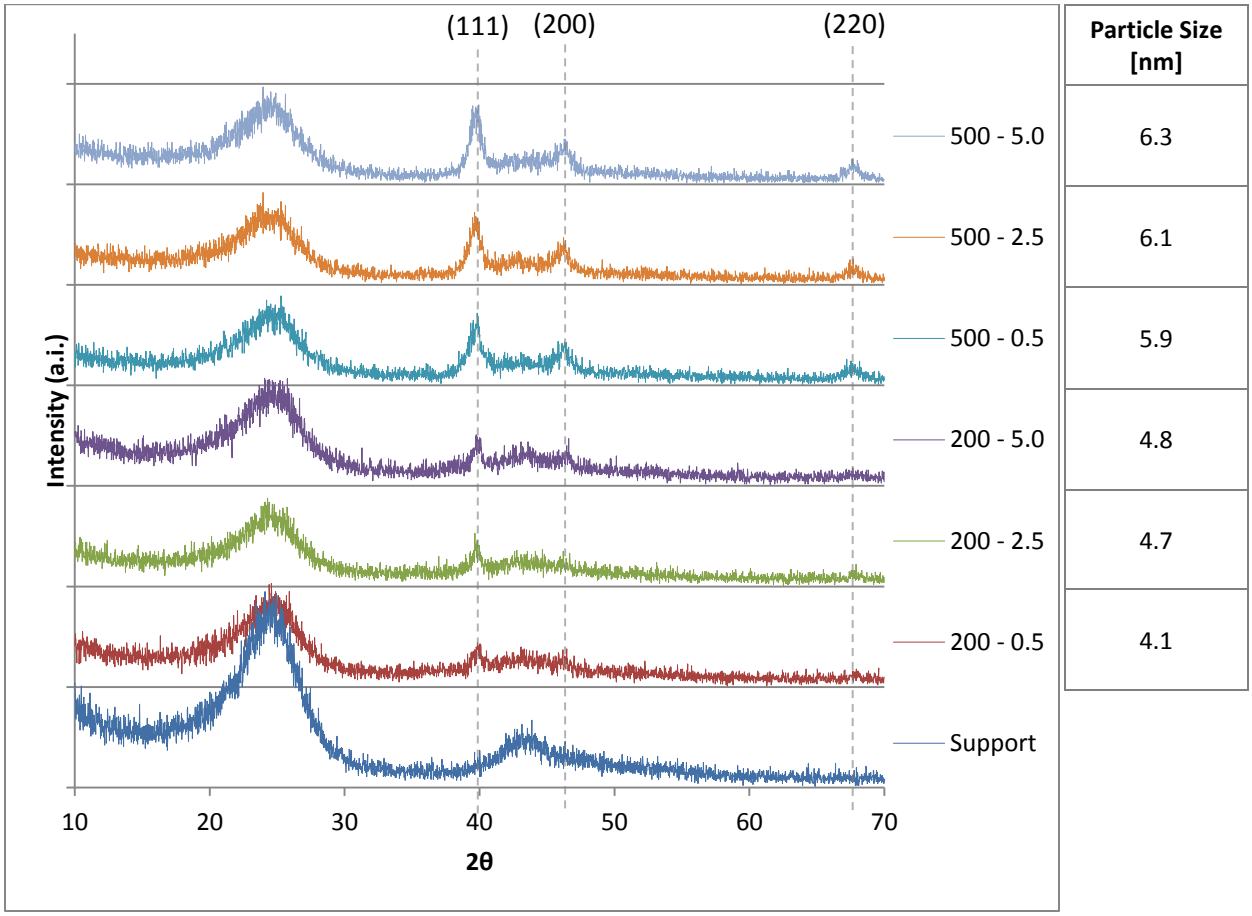

Figure 4.34 XRD results for XC72-PdTC-SEA.

The XRD analysis for the XC72 carbon impregnated with PdTC by SEA is displayed in Figure 4.34. There is an increase in the size of the peaks of the samples reduced at 500°C compared to the 200°C ones. There is also a slight increase in particle size when the heating rate is elevated. This relationship between palladium particle size and reduction temperature was also seen in the other carbon-palladium catalyst HSAG300-PdTA-SEA. It is also noteworthy the PdO peaks which were present in the XC72-PdTC catalyst prepared by DI are not found in this catalyst. This is unexpected considering the particle sizes of the two catalyst sets are similar.

Since the only variation between them is the synthesis method, it appears SEA preparation diminishes the formation of PdO.

The STEM imaging results from Table 4.18 agree with the XRD analysis mentioned above. There is a clear increase of the average particle sizes and standard deviations of the samples reduced at 500°C. Most of the results have revealed palladium particle size is in general more sensitive to reduction temperature than platinum.

Table 4.18 STEM particle size analysis for XC72-PdTC-SEA.

	200°C			**500°C**		
	0.5°C/ min	**2.5°C/ min**	**5.0°C/ min**	**0.5°C/ min**	**2.5°C/ min**	**5.0°C/ min**
<*p*>	1.2	2.7	1.5	5.5	4.9	6.4
n	947	1017	977	1293	1035	1086
sd	0.31	0.31	1.2	2.4	2.2	3.1

<p> – average particle size, n – number of particles counted, sd – standard deviation.

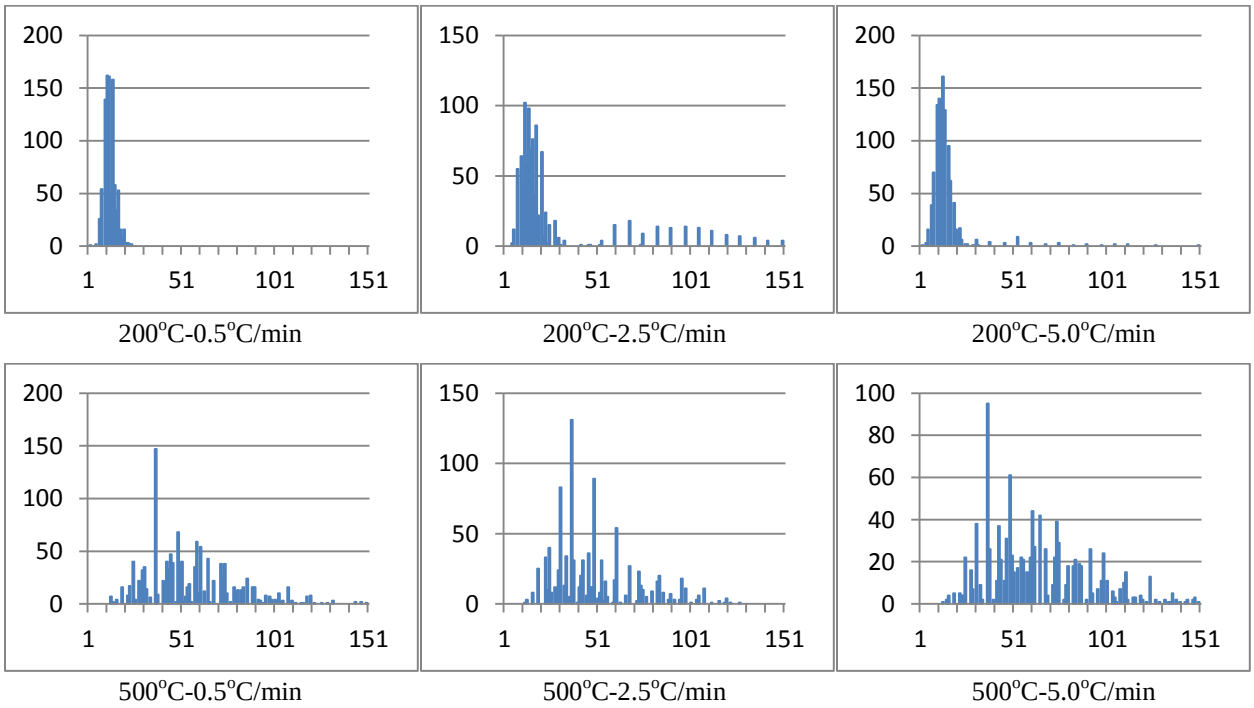

Figure 4.35 Particle size distributions for XC72-PdTC-SEA catalysts.

The results from Figure 4.35 show there is a slight widening of the particle size distribution curves when the heating rate is increased. Once again, reduction temperature plays the dominant role in sintering. The set of samples reduced at 200^{o}C don't show any particular sintering mechanism but the 500^{o}C set does display a PMC shape especially towards the higher heating rates. No individual palladium atoms were seen in the carbon surface during high magnification STEM imaging.

4.3 Further discussion

Tables 4.19 and 4.20 summarize the average particle sizes for all DI and SEA prepared catalysts respectively. The values displayed are mostly from STEM imaging particle size analysis (for those samples which didn't have STEM results, XRD data was used). STEM data was chosen for these master tables since most of the SEA samples didn't show any XRD results. The role humidity and dryness play in the sintering of the metal catalysts can be easily noticed. For the grand majority of the samples, the "humid" samples (ice and water) yielded the largest average particle sizes while the "dry" samples (75 He and 150 He) are always among the smallest.

Table 4.19 DI prepared catalysts particle size [nm] master table.

		200°C			500°C			200°C at 0.5°C/min		
Support	**Precursor**	**0.5°C/ min**	**2.5°C/ min**	**5.0°C/ min**	**0.5°C/ min**	**2.5°C/ min**	**5.0°C/ min**	**75 He**	**150 He**	**water**
HSAG300	PTA	7.8	4.7	5.4	12.5	15.0	10.7	2.5	3.2	15.4
HSAG300	PdTA	2.9	6.5	3.0	4.2	4.8	4.8			
SiO2	PTA	7.3	7.3	11.2	10.5	13.0	14.5	7.4	6.4	7.7
SiO2	PdTA	11.9	11.0	12.4	13.8	13.6	9.8			
TiO2	PTA	3.0	2.9	3.0	4.7	3.0	4.5	2.2	2.2	9.1
TiO2	PdTA	-	-	-	-	-	-			
Al2O3	CPA	1.5	2.1	1.5	1.8	2.2	2.1	1.4	1.1	8.8
Al2O3	PdTC	3.5	2.1	2.4	4.8	4.9	9.6			
XC72	CPA	1.5	1.3	1.8	1.5	1.5	2.9	1.7	1.7	3.2
XC72	PdTC	2.4	2.0	5.4	6.2	6.9	5.6			

Table 4.20 SEA prepared catalysts particle size [nm] master table.

		200°C			500°C			200°C at 0.5°C/min		
Support	**Precursor**	**0.5°C/ min**	**2.5°C/ min**	**5.0°C/ min**	**0.5°C/ min**	**2.5°C/ min**	**5.0°C/ min**	**150 He**	**ice**	**water**
HSAG300	PTA	1.3	1.5	1.5	1.4	1.3	1.4	1.1	1.4	1.7
HSAG300	PdTA	1.6	1.4	2.5	4.6	4.5	4.0			
SiO2	PTA	0.9	1.2	0.9	1.4	1.2	1.1	0.8	1.2	1.3
SiO2	PdTA	1.2	1.3	1.5	1.2	1.3	1.4			
TiO2	PTA	1.2	1.1	1.3	1.1	1.2	1.2	1.0	1.7	1.9
TiO2	PdTA	-	-	-	-	-	-			
Al2O3	CPA	1.0	0.9	1.2	1.2	1.1	1.5	0.9	1.2	1.1
Al2O3	PdTC	1.4	1.0	1.3	4.0	4.1	4.1			
XC72	CPA	0.9	0.9	1.0	1.2	1.2	1.3	1.0	1.1	2.5
XC72	PdTC	1.2	2.7	1.5	5.5	4.9	6.4			

Taking a statistical approach, Figure 4.36 depicts the number of Pt and Pd samples at each pretreatment condition which yielded the smallest particle size of the whole group excluding the humidity variation samples. The results shown are for both DI and SEA samples combined. For example for the HSAG300-PTA-DI set of samples in Table 4.19, the 200^{o}C-2.5^{o}C/min sample had the smallest particle size of the whole set (4.7 nm), so this sample is included in the 200^{o}C-2.5^{o}C/min count for platinum in Figure 4.36. In case two different samples are tied for the lowest particle size of their sample set, they both where included in their respective counts.

The results satisfactorily show a clear pattern where the lower heating rates and low reduction temperature produced most of the smallest particles for both platinum and palladium, making 200^{o}C-2.5^{o}C/min the set of conditions with the top count. These results show agreement with the literature review of Section 2.4. A reason why the lowest heating rate didn't statistically generate the highest --small particle size-- count as was originally expected, could be related to the total pretreatment time. The longer a sample is pretreated, the more probable it is for the metal particles to sinter. The fact that heating the samples at a rate of 2.5^{o}C/min (3 hours) reduces the pretreatment time by 5 hours compared to 0.5^{o}C/min (8 hours), and that the

5.0°C/min rate (2.5 hours) didn't yield as many small particles, implies the 2.5°C/min heating rate holds a better balance of gentle temperature increase with appropriate pretreatment time. It is worth mentioning that when this type of analysis was done for the DI and the SEA samples separately, the results looked reassuringly similar.

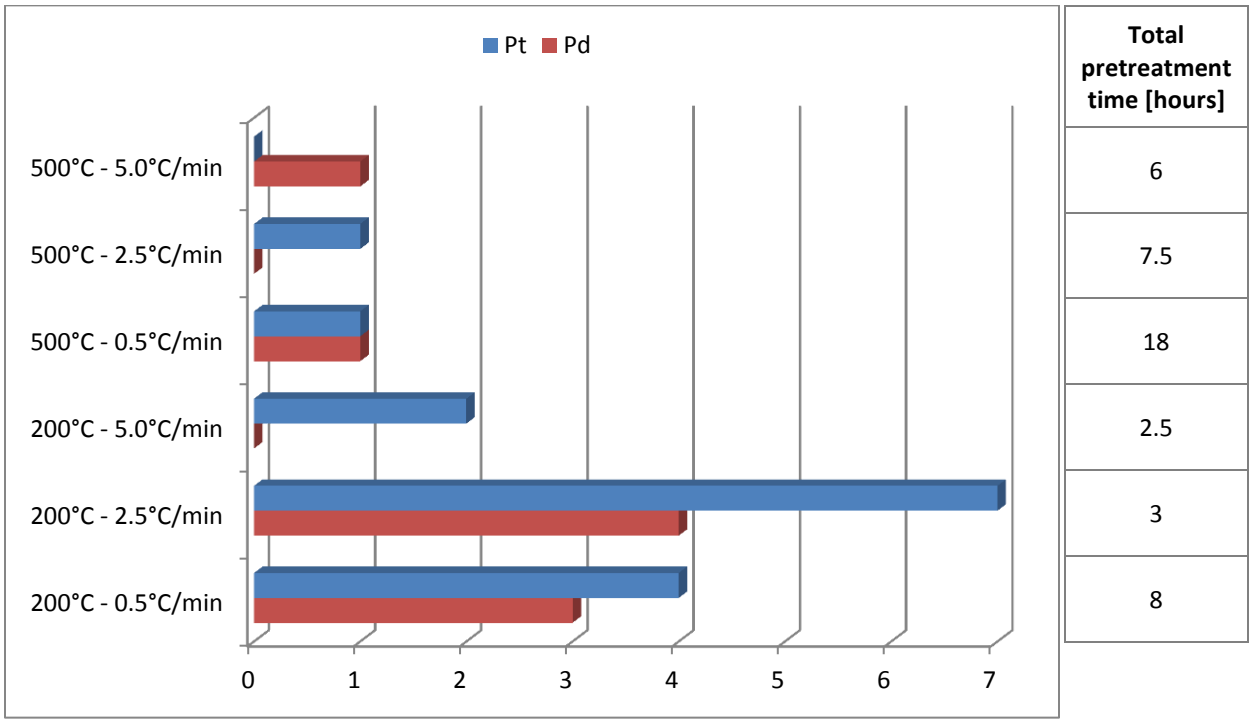

Total pretreatment time [hours]
6
7.5
18
2.5
3
8

Figure 4.36 Number of Pt and Pd samples which had the smallest particle size of their corresponding catalyst set at the indicated reduction conditions.

A visual rendering of Tables 4.19 and 4.20 is constructed in Figures 4.37 and 4.38 for DI and SEA prepared catalysts respectively. The change in particle size with respect to heating rate has been plotted in a 3-dimensional graph where the different samples are grouped according to their similar characteristics and variables. It is noticeable right away how the DI samples' (Figure 4.37) particle sizes fluctuate more than the SEA samples. From the perspective of Figures 4.37 and 4.38, the heating rate didn't develop a clear trend of particle size change, especially in the DI samples where the sole nature of the preparation method introduced an element of randomness. These figures also show how palladium is affected by temperature more than platinum. This is

more clearly demonstrated in the HSAG300-PdTA-SEA samples, and Al2O3 and XC72 supports for both DI and SEA. Some of the observations about the increase in particle size with increasing reduction temperature drawn during the previous explanations of the results are evident in these charts as well. It's apparent the SEA samples' particle sizes weren't affected as much by heating conditions when compared to the DI samples. This is due to the strong electrostatic interaction which takes place between the metal precursors and the support (explained in section 3.2). These ionic interactions were even strong enough to compete with the sintering effects of water vapor during reduction, demonstrated by comparing the average particle sizes of the "humid" samples from the DI and SEA prepared catalysts in Tables 4.19 and 4.20.

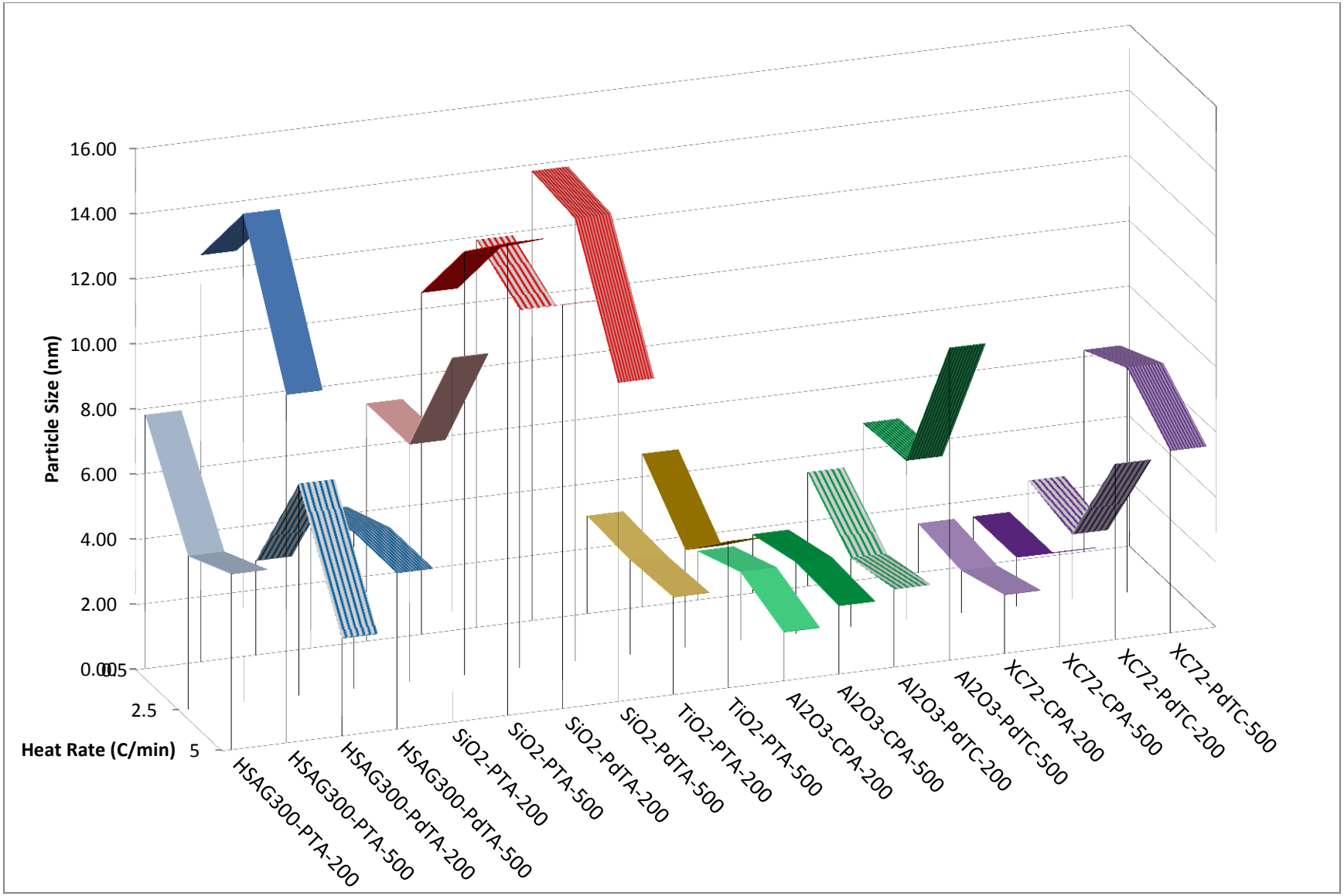

Figure 4.37 DI prepared catalysts master chart. General identifications: Blue-HSAG300, Red-SiO2, Brown-TiO2, Green-Al2O3, Violet-XC72; light colors-200^{o}C reduction temperature, dark colors-500^{o}C reduction temperature; thick stripes-Pt, thin stripes-Pd.

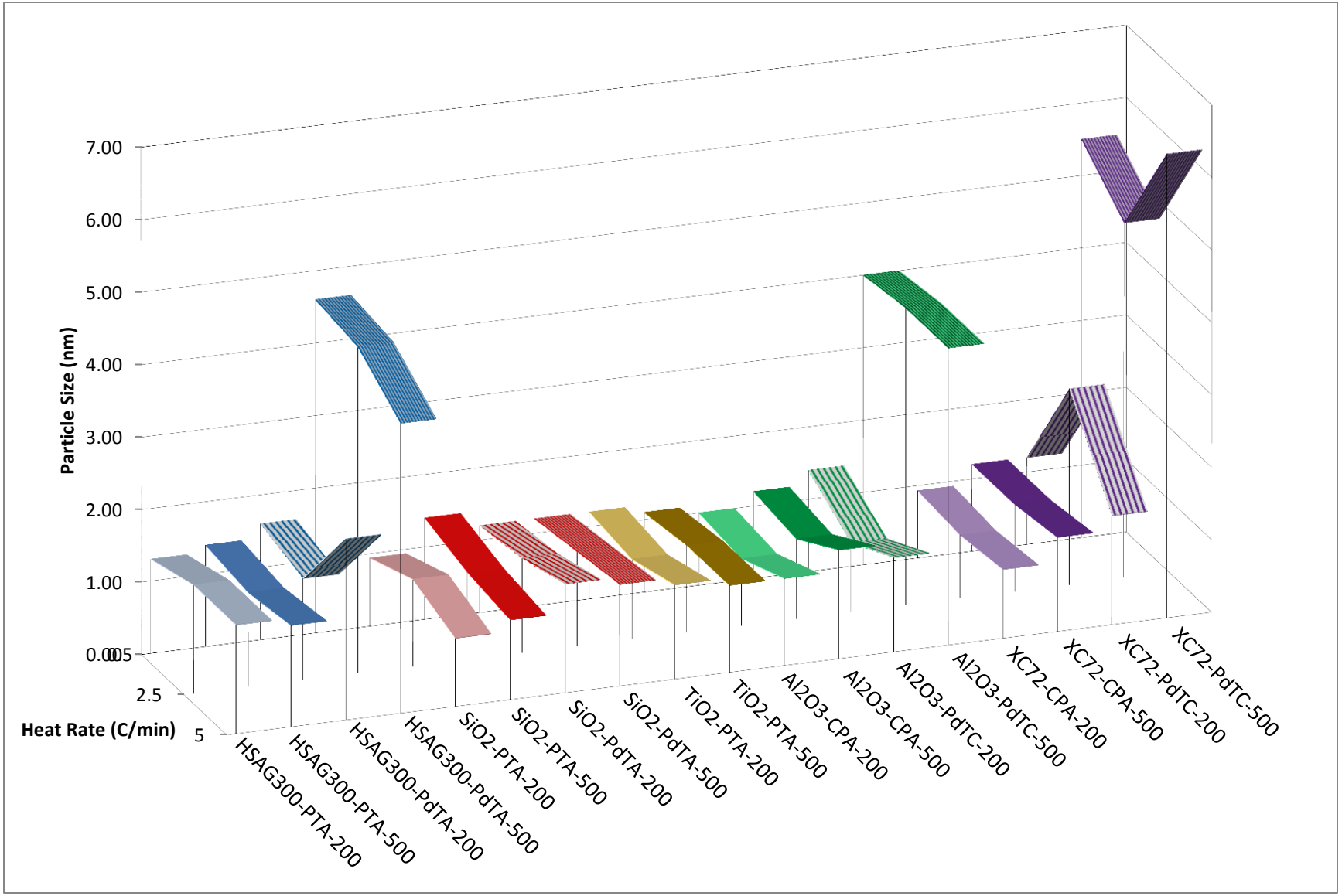

Figure 4.38 SEA prepared catalysts master chart. General identifications: Blue-HSAG300, Red-SiO2, Brown-TiO2, Green-Al2O3, Violet-XC72; light colors-200^{o}C reduction temperature, dark colors-500^{o}C reduction temperature; thick stripes-Pt, thin stripes-Pd.

5. CONCLUSIONS AND RECOMMENDATIONS

The experimentation has revealed the most critical sintering factor during pretreatment reduction is the presence of water vapor especially for DI prepared catalysts. The results also proved that the opposite is true; if the partial pressure of water vapor or chlorine produced during reduction is lessened by effective evacuation with the introduction of helium into the hydrogen stream, sintering is reduced to a minimum.

The results demonstrated how low heating rates and a low reduction temperature during pretreatment produces smaller metal particle sizes for both platinum and palladium. An optimal set of pretreatment conditions was found (200^{o}C of reduction temperature at a heating rate of 2.5^{o}C/min) where the catalyst systems are most likely to produce the smallest particle size. Palladium indicated to be more sensitive to reduction temperature than platinum.

For some samples STEM imaging revealed the presence of individual platinum atoms along the surface of the support. The abundance of these individual atoms was significantly diminished for the samples reduced at 500^{o}C which further proves the sintering effect of higher reduction temperatures.

If the shape of the average particle size distribution curve can indicate a certain sintering mechanism taking place, then the PMC mechanism was found to occur especially for the catalyst samples with low levels of dispersion (DI prepared catalysts mostly). The SEA samples showed mostly symmetrical particle size distribution curves which could indicate both OR and PMC mechanisms taking place at the same time. Furthermore, individual platinum atoms where noticed to withdraw when the reduction temperature was increased suggesting that movement and migration of individual atoms took place, which is the basic principle of the OR sintering mechanism.

For future work it is recommended a closer look is taken to the Al2O3-CPA and HSAG300-PTA catalysts systems, which revealed the presence of individual atoms through the surface of the supports, and attempt to understand the sintering mechanism of platinum starting from its monolayer form.

Since the lowest heating rate didn't produce the smallest metal particle size in the majority of the cases, and a moderate heating rate seemed to better balance the time of pretreatment with an appropriate heating rate, further experimentation is required to precisely determine an optimal heating rate.

To confirm if the pretreatment time plays a crucial role in metal particle sintering, subsequent experiments are suggested where the dwell time of the catalyst at the final reduction temperature is increased and observe if there is any loss of dispersion. Should no significant change in the sintering of the catalyst under these new conditions occur, a new theory to explain why a moderate heating rate produces the smaller particle sizes would be required.

This research revealed that reduction temperature affected the level of sintering of Pt and Pd differently. At higher reduction temperatures Pd showed to change lose dispersion more significantly in carbon and alumina supports for both DI and SEA prepared catalysts. It is recommended to investigate the causes why the Pd precursors are apparently more mobile than Pt under higher reduction temperatures.

While the experiments of this thesis dealt purely with metal particle sizes, a different analysis approach should be taken on these samples to gather more information about the oxidation state of the metals, changes in surface area of the supports, hindrance of the metal catalysts due to strong metal support interactions, and other aspects which the pretreatment conditions could have influenced and will ultimately affect the performance of the catalysts.

Finally, the behavior of palladium impregnated into TiO2 could not be analyzed because of the very low loading of the metal due to the small surface area of the support. The analysis of this catalyst system should be attempted once again on a higher surface area TiO2 where a higher concentration of palladium can be achieved.

CITED LITERATURE

[1] Richard I. Masel, Chemical Kinetics and Catalysis, Wiley-Interscience, New York, 2001.

[2] J.W. Niemantsverdriet, Spectroscopy in Catalysis an Introduction, Wiley-VCH, Weinheim, 2007.

[3] J.R. Regalbuto, (Ed.), Catalyst Preparation: Science and Engineering, Taylor & Francis/CRC Press, Boca Raton, 2006, p. 297.

[4] G.C. Bond, Heterogeneous Catalysis Principles and Applications, Oxford University Press, New York, 1987.

[5] Julian R.H. Ross, Heterogeneous Catalysis Fundamentals and Applications, Elsevier B.V., Amsterdam, 2012.

[6] W. Gerhartz et al., "Catalysis and Catalysts" in Ullmann's Encyclopedia of Industrial Chemistry, Vol A5, VCH, Germany, 1986.

[7] J. Park, and J.R. Regalbuto, *J. Colloid Interface Sci.* 175 (1995) 239.

[8] J.R. Regalbuto, in: R.M. Richards, (Ed.), Surface and Nanomolecular Catalysis, Taylor & Francis/CRC Press, Boca Raton, 2006, p. 161.

[9] M. Schreier, and J.R. Regalbuto, *J. Catal*. 225 (2004) 190.

[10] K.B. Agashe, and J.R. Regalbuto, *J. Colloid Interface Sci.* 185 (1997) 174.

[11] J.R. Anderson, Structure of Metallic Catalysts; Academic Press Inc., London, 1975.

[12] John B. Moffat, Theoretical Aspects of Heterogeneous Catalysis, Van Nostrand Reinhold, New York, 1990.

[13] R.A. Dalla Betta and M. Boudart, Proceedings 5th International Congress on Catalysis, J.W. Hightower ed, Amsterdam, 1973.

[14] D. Radivojevic´, K. Seshan, L. Lefferts, *Applied Catalysis A: General* 301 (2006) 51.

[15] A. Borgna, T.F Garetto, C.R. Apesteguía, F. Le Normand, and B. Moraweck, *J. Catal.* 186, (1999) 433.

[16] J.J.F. Scholten, and A. van Montfoort, *J. Catal*. 1, (1962) 85.

[17] E. Ruckenstein and B. Pulvermacher, *J. Catal.* 29 (1973) 224.

[18] B.K. Chakraverty, *J. Phys. Chem. Solids*. 28 (1967) 2401.

[19] P.C. Flynn, and S.E. Wanke, *J. Catal.* 33 (1974) 233.

[20] P.C. Flynn, and S.W. Wanke, *J. Catal.* 34 (1974) 390.

[21] E. Ruckenstein, and D.B. Dadyburjor, *J. Catal*. 48 (1977) 73.

[22] H.H. Lee, *J. Catal.* 62 (1980) 129.

[23] P.Wynblatt, and N.A. Gjostein, *Prog. Solid State Chem.* 9 (1975) 21.

[24] A.K. Datye, Q. Xu, K.C. Kharas, and J.M. McCarty, *Catalysis Today* 111 (2006) 59.

[25] C.G. Granqvist, and R.A. Buhrman, *J. Catal.* 42 (1976) 477.

[26] S.A Stevenson, J.A. Dumesic, R.T.K. Baker, and E. Ruckenstein, Metal-Support Interactions in Catalysis, Sintering, and Redispersion, Van Nostrand Reinhold Company Inc., New York, 1987.

[27] R. Finsy, *Langmuir* 20 (2004) 2975–2976.

[28] Q. Wang, R. Finsy, XU Hai-bo, and LI Xi, *J Zhejiang Univ SCI* 2005 6B(8): 705.

[29] C.G. Granqvist, and R.A. Buhrman, *J. Appl. Phys.*47 (1976) 2200.

[30] Y. De Smet, L. Deriemaeker, and R. Finsy, *Langmuir* 13 (1997) 6884–6888

[31] S.E. Wanke, *J. Catal.* 46 (1977) 234.

[32] C.G. Granqvist, and R.A. Buhrman, *J. Catal.* 46 (1977) 238.

[33] E.C. Stassinos, and H.H. Lee, *Chem. Eng. Sci.* Vol. 50, No. 8 (1995) 1337.

[34] I. Sushumna, and E. Ruckenstein, *J. Catal.* 109 (1988) 433.

[35] Y. Waseda, E. Matsubara, K. Shinoda, X-Ray diffraction crystallography [electronic resource] : introduction, examples and solved problems, Springer, Berlin, 2011.

[36] A. Al-Owais, *J. King Saud Univ., Vol. 7, Science(1)* (A.H. 1415/1995) p.89.

[37] E. Antolini, *J. Mat. Sci.* 38 (2003) 2995.

[38] N. Barrabés, K. Föttinger, J. Llorca, A. Dafinov, F. Medina, J. Sá, C. Hardacre, and G. Rupprechter, *J. Phys. Chem. C* 114 (2010) 17675.

[39] R. Burch, and L.C. Garla, *J. Catal.* 73 (1982) 20.

[40] H.C. Yao, M. Sieg, and H.K. Plummer Jr., *J. Catal.* 59 (1979) 365.

[41] F.M. Datuzenberg, and H.B.M. Wolters, *J. Catal.* 51 (1978) 26.

[42] J. de Graaf, A.J. van Dillen, K.P. de Jong, and D.C. Koningsberger, *J. Catal.* 203 (2001) 307.

[43] K.S. Han, Y.S. Moon, O.H. Han, K.J. Hwang, In Kim, and H. Kim, *Electorchem. Communications* 9 (2007) 317.

[44] T. Mallat, S. Frauchiger, P.J. Kooyman, M. Schürch, and A. Baiker, *Catal. Lett.* 63 (1999) 121.

[45] G.A. Martin, R. Dutartre, S. Yuan, C. Márquez-Alvarez, and C. Mirodatos, *J. Catal.* 177 (1998) 105.

[46] P.G. Menon, and G.F. Froment, *J. Catal.* 59 (1979) 138.

[47] A. Muñoz-Páez, and D.C. Koningsberger, *J. Phys. Chem.* 99 (1995) 4193.

[48] P.H. Otero-Schipper, W.A. Wachter, J.B. Butt, R.L. Burwell Jr, and J.B. Cohen, *J. Catal.* 53 (1978) 414.

[49] M.K. Oudenhuijzen, P.J. Kooyman, B. Tappel, J.A. van Bokhoven, and D.C. Koningsberger, *J. Catal.* 205 (2002) 135.

[50] M. Schürch, O. Schwalm, T. Mallat, J. Weber, and A. Baiker, *J. Catal.* 169 (1997) 275.

[51] C.A. Müller, M. Maciejewski, R.A. Koeppel, and A. Baiker, *Catal. Today* (1999) 245.

[52] R. Burch, and F.J. Urbano, *Appl. Catal. A: Gen.* 124 (1995) 121.

[53] K. Köhler, R.G. Heidenreich, J.G.E. Krauter, and J. Pietsch, *Chem.-A Europ. J.* Vol. 8, Issue 3 (2002) 622.

[54] M. Wagner, K. Köhler, L. Djakovitch, S. Weinkauf, V. Hagen, and M. Muhler, *Topics in Catal.* 13 (2000) 319.

[55] N. Krishnankutty, J. Li, and A. Vannice, *App. Cat. A: Gen.* 173 (1998) 137.

[56] N. Krishnankutty, and M.A. Vannice, *J. Catal*. 155 (1995) 312.

[57] D.J. Smith, D. White, T. Baird, and J.R. Fryer, *J. Catal.* 81 (1983) 107.

[58] F. Zhao, Y. Ikushima, M. Shirai, T. Ebina, and M. Arai, *J. Mol. Catal. A: Chem.* 180 (2002) 259.

[59] M. Arai, Y. Takada, and Y. Nishiyama, *J. Phys. Chem. B* 102 (1998), 1968-1973.

[60] J.T. Miller, M. Schreier, A.J. Kropf, and J.R. Regalbuto, *J. Catal*. 225 (2004) 203.

[61] J.H. Sepúlveda, and N.S. Fígoli, *Applied Surface Science* 68, (1993) 257.

[62] H.A. Benesi, and R.M. Curtis, *J. Catal.*10 (1968) 328.

[63] M. Chen, and L.D. Schmidt, *J. Catal.* 55 (1978) 348.

[64] H.L. Gruber, *Anal. Chem.* 34 (1962) 1828.

[65] T.R. Hughes, R.J. Houston, and R.P. Sieg, *Ind. Eng. Chem. Process Des. Develop.* 1 (1962) 96.

[66] J.A. Bett, K. Kinoshita, and P. Stonehart, *J. Catal.* 35 (1974) 3017.

[67] T.A. Dorling, B.W.J. Lynch, and R.L. Moss, *J Catal.* 20 (1971) 190.

[68] R.M.J Friedorow, B.S. Chahar, and S.E. Wanke. *J. Catal.* 51 (1978) 193.

[69] S.A. Hassan, F.H. Khalil, and F.G. El-Gamal, *J. Catal.* 44 (1976) 5.

[70] P.C. Flynn, and S.E. Wanke, *J Catal.* 37 (1975) 432.

[71] M. Gurrath, *Carbon* 38 (2000) 1241.

[72] V.A. Semikolenov, S.P. Lavrenko, V.I. Zaikovskii, and A.I. Boronin, *React. Kinet. Catal. Lett.*, Vol. 51, No. 2 (1993) 517.

[73] Y.A. Ryndin, M.V. Stenin, A.I. Boronin, V.I. Bukhtiyarov, and V.I. Zaikovskii, *Appl. Catal.* 54 (1989) 277.

[74] W.G. Shim, S.C. Kim, H.C. Kang, S.W. Nahm, J.W. Lee, and H. Moon, *Appl. Surf. Sci.*253 (2007) 5868.

[75] N. Santhanam, T.A. Conforti, W. Spieker, and J.R. Regalbuto, *Catal. Today* 21 (1994) 141.

[76] R.H. Perry, and D.W. Green, "Perry's chemical engineers' handbook", 7th ed., McGraw Hill, 1997.

[77] X. Hao, S. Barnes, and J.R. Regalbuto, *J. Catal.* 279 (2011) 48.

[78] R. Hussain, R. Qadeer, M. Ahmad, and M. Saleem, *Turk. J. Chem.* 24 (2000) 177.

[79] K. Thamaphat, P. Limsuwan, and B. Ngotawornchai, *Kasetsart J. (Nat. Sci.)* 42 (2008) 357.

[80] K. Wang, T. Huang, H. Liu, Y. Zhao, H Liu, and C. Sun, *Colloids and Surfaces A: Physiochem. Eng. Aspects* 325 (2008) 21.

[81] B. Cornils, W.A. Herrmann, M. Muhler, and C. Wong, Catalysis from A to Z, A Concise Encyclopedia, Second Ed., Wiley-VCH, Germany.

[82] R.A. van Santen, and J.W. Niemantsverdriet, Chemical Kinetics and Catalysis, Plenum Press, New York, 1995.

[83] J.A. Dumesic, The Microkinetics of Heterogeneous Catalysis, American Chemical Society, Washington, D.C., 1993.

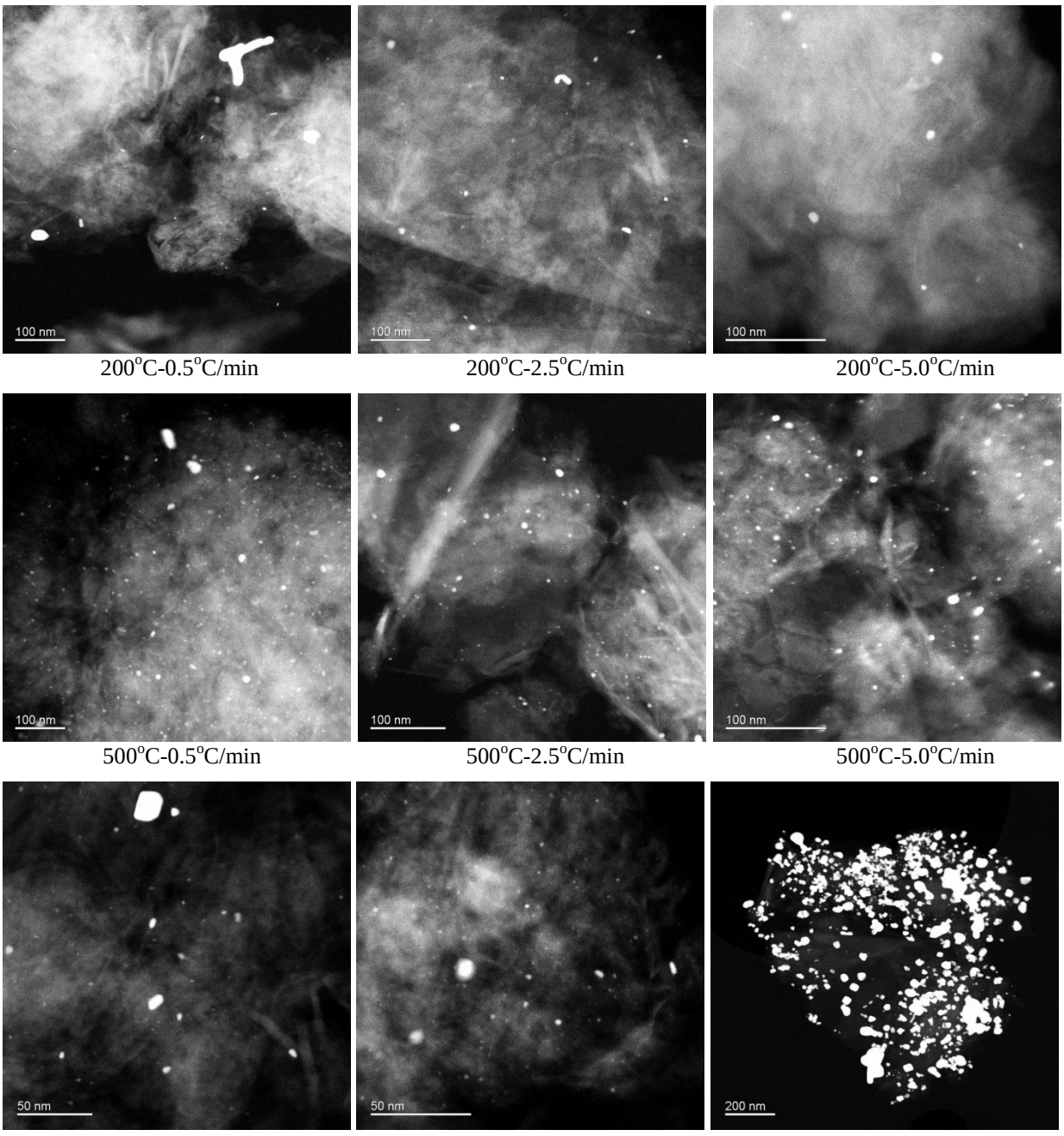

Figure A.1 STEM image examples for HSAG300-PTA-DI catalysts.

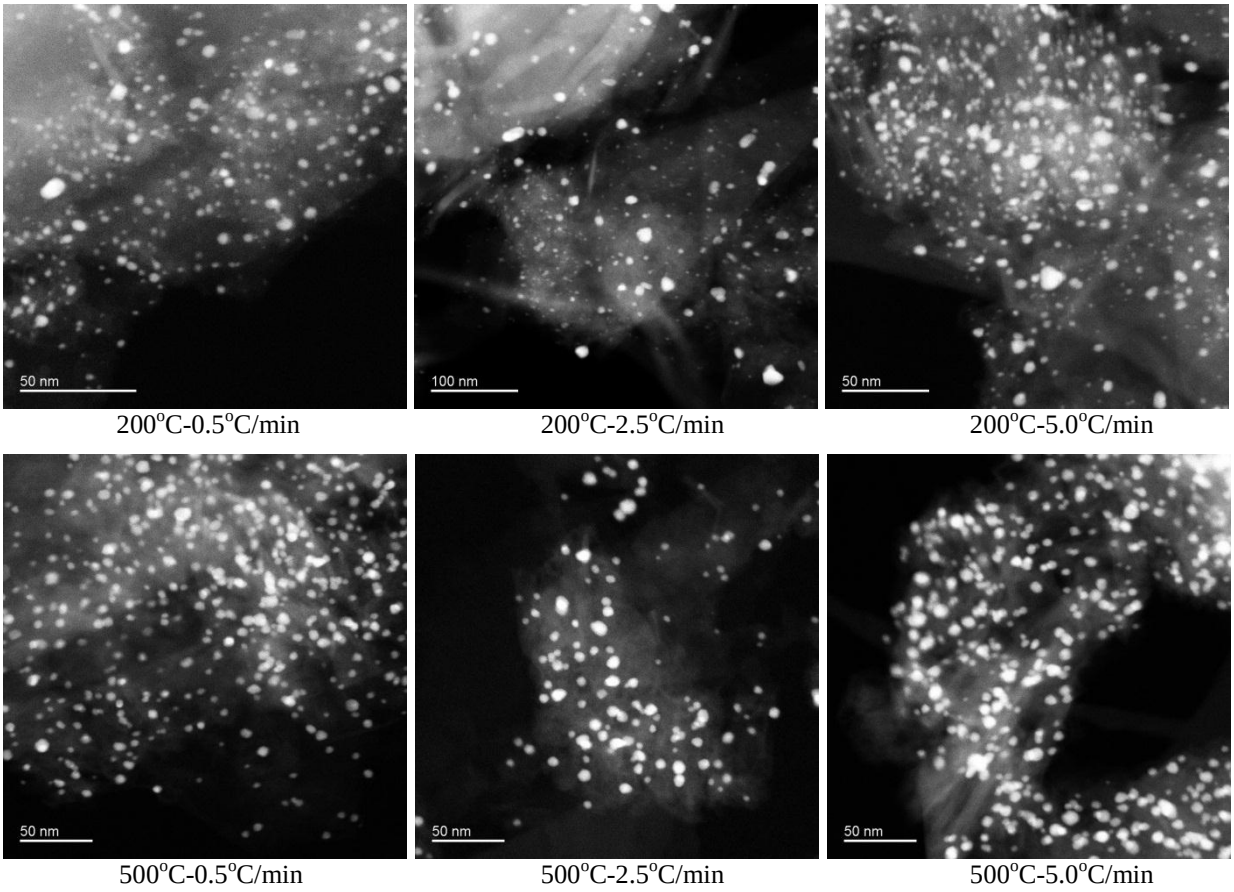

200°C-0.5°C/min | 200°C-2.5°C/min | 200°C-5.0°C/min

500°C-0.5°C/min | 500°C-2.5°C/min | 500°C-5.0°C/min

Figure A.2 STEM image examples for HSAG300-PdTA-DI catalysts.

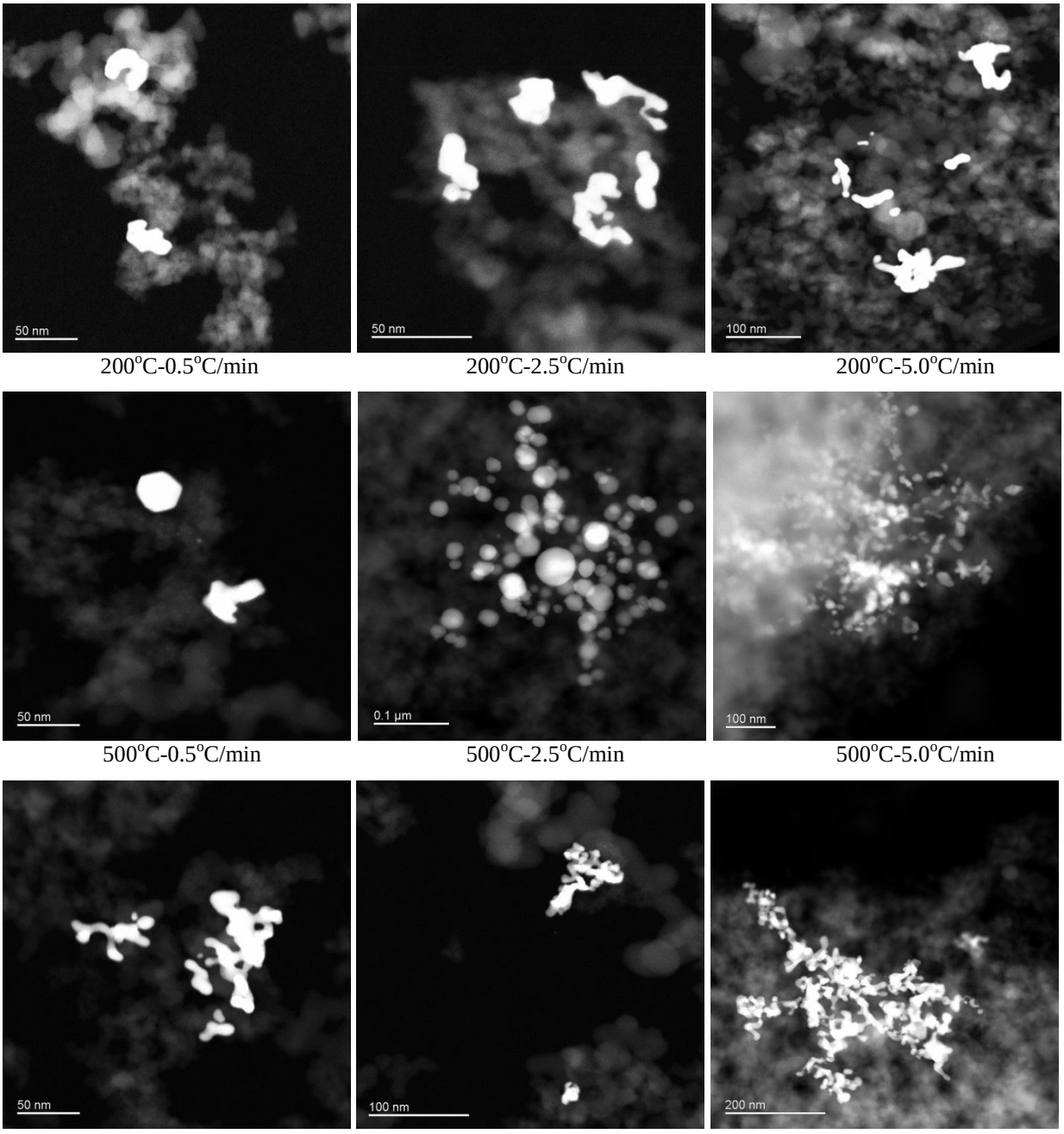

200°C-0.5°C/min | 200°C-2.5°C/min | 200°C-5.0°C/min

500°C-0.5°C/min | 500°C-2.5°C/min | 500°C-5.0°C/min

75He | 150He | water

Figure A.3 STEM image examples for SiO2-PTA-DI catalysts.

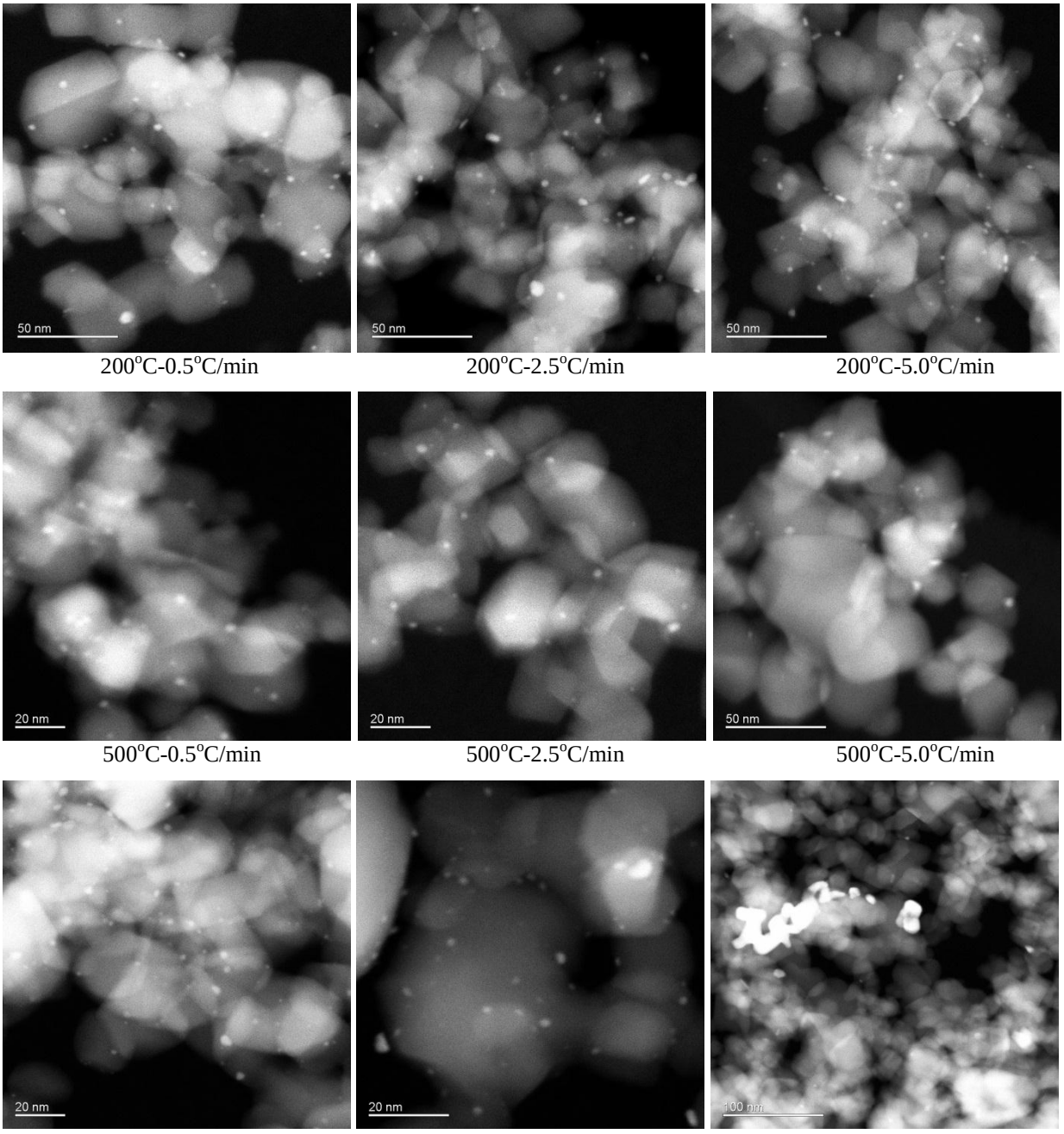

Figure A.4 STEM image examples for TiO2-PTA-DI catalysts.

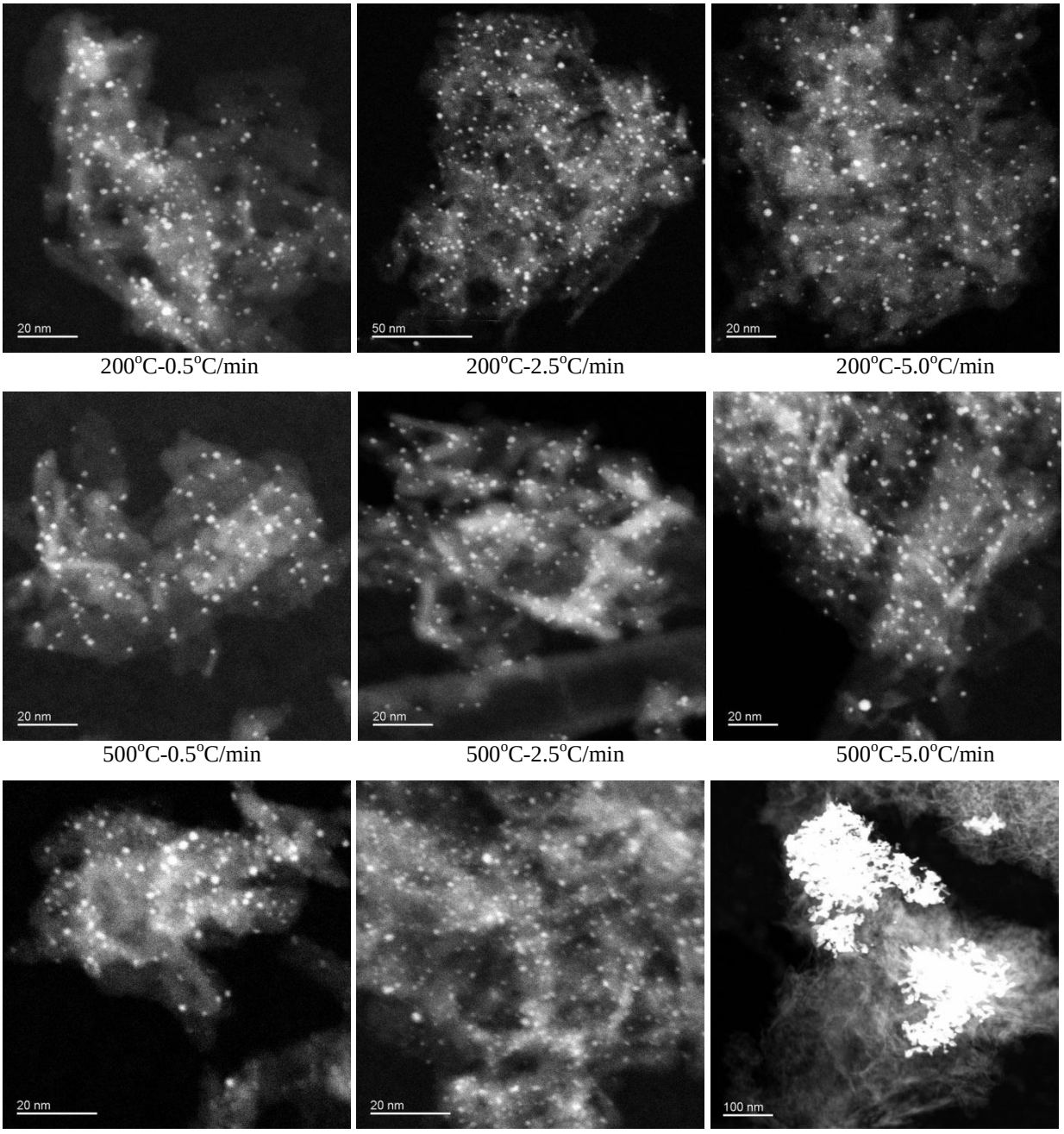

200°C-0.5°C/min | 200°C-2.5°C/min | 200°C-5.0°C/min

500°C-0.5°C/min | 500°C-2.5°C/min | 500°C-5.0°C/min

75He | 150He | water

Figure A.5 STEM image examples for Al2O3-CPA-DI catalysts.

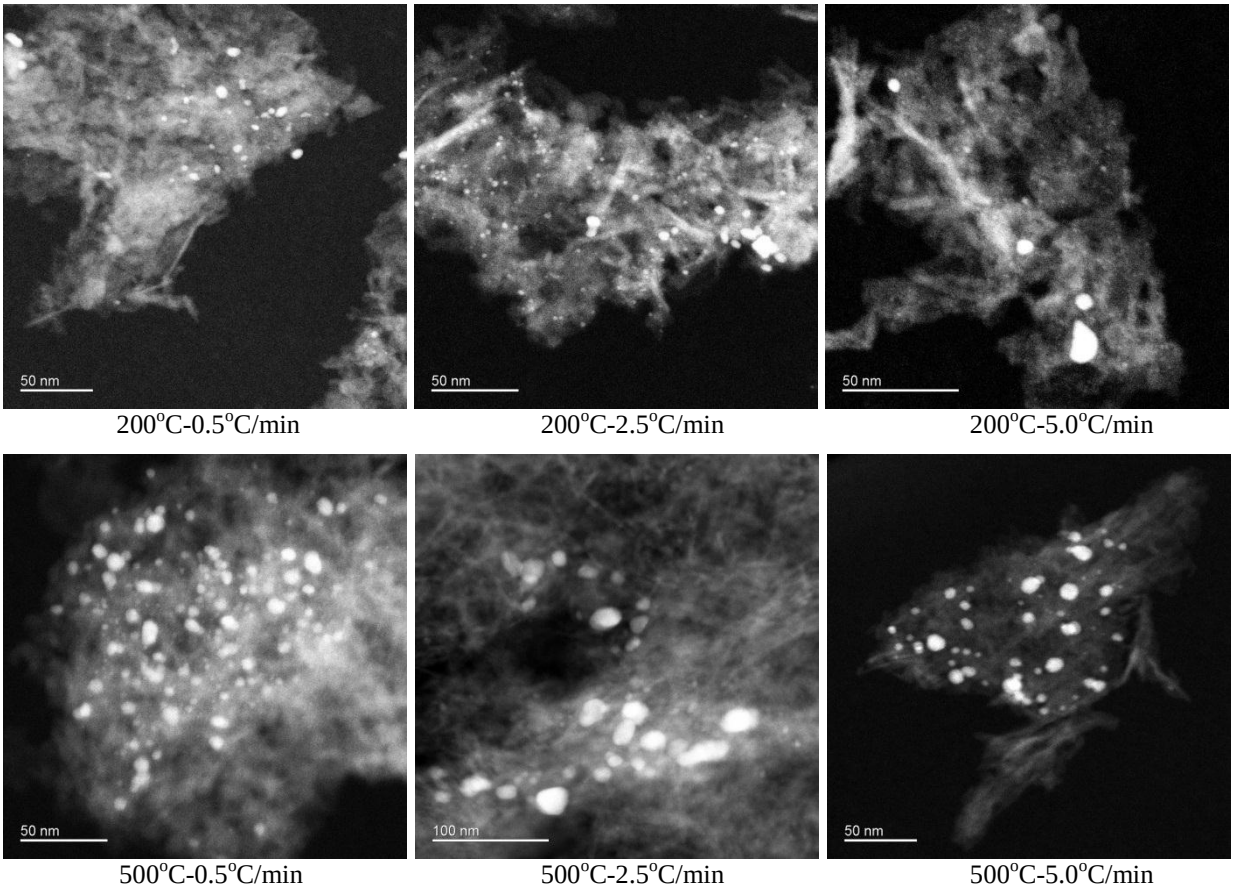

200°C-0.5°C/min | 200°C-2.5°C/min | 200°C-5.0°C/min

500°C-0.5°C/min | 500°C-2.5°C/min | 500°C-5.0°C/min

Figure A.6 STEM image examples for Al2O3-PdTC-DI catalysts.

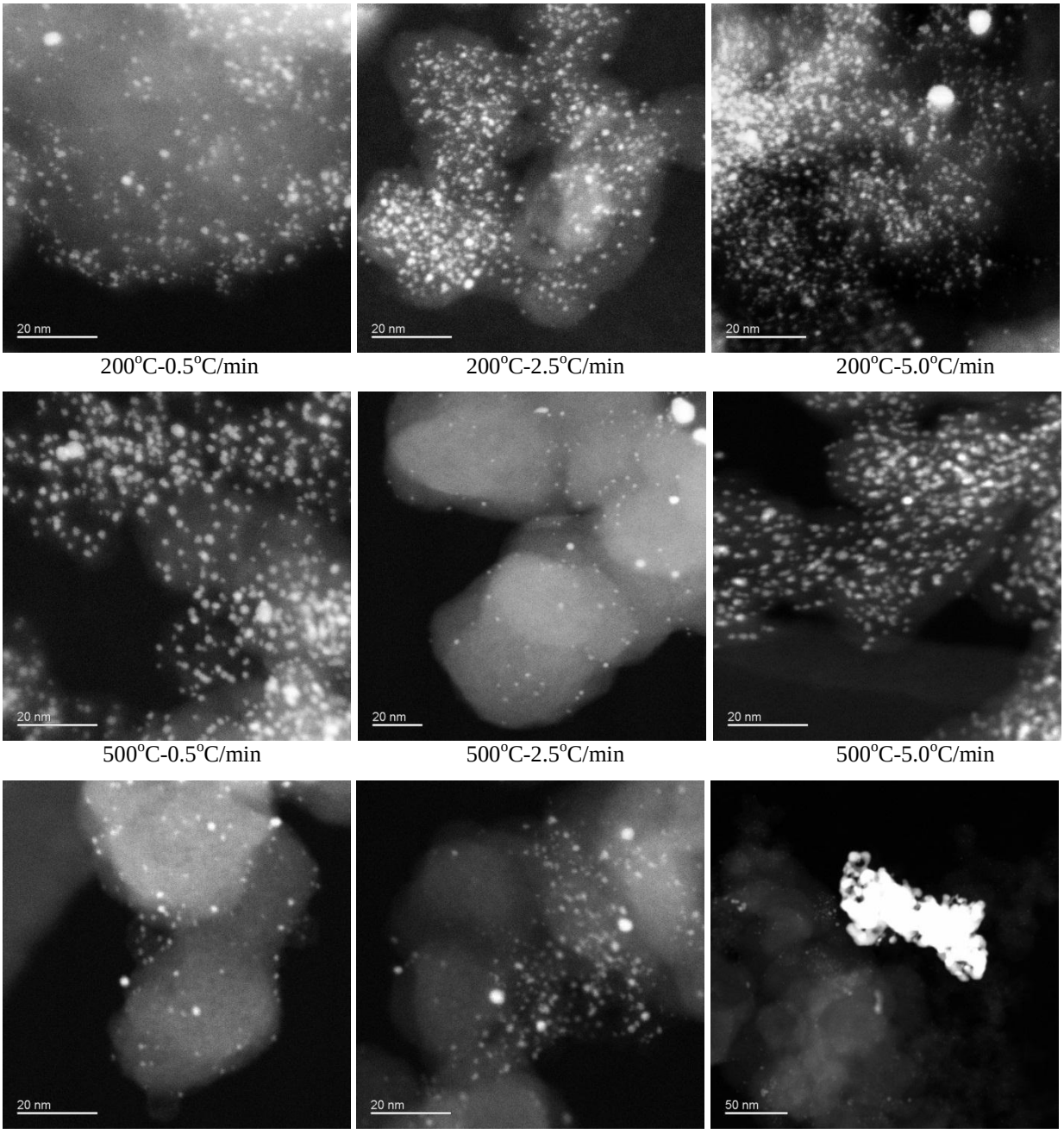

Figure A.7 STEM image examples for XC72-CPA-DI catalysts.

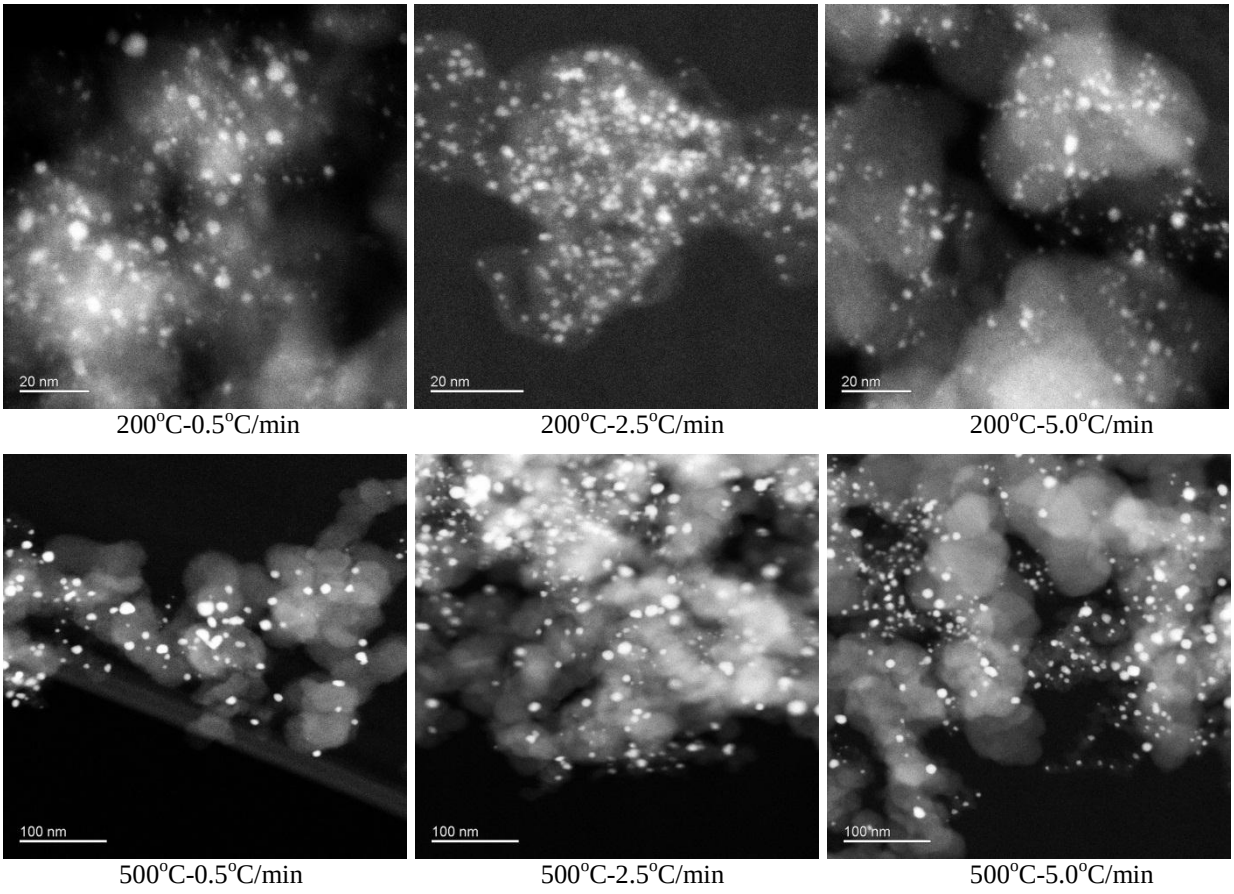

200°C-0.5°C/min | 200°C-2.5°C/min | 200°C-5.0°C/min

500°C-0.5°C/min | 500°C-2.5°C/min | 500°C-5.0°C/min

Figure A.8 STEM image examples for XC72-PdTC-DI catalysts.

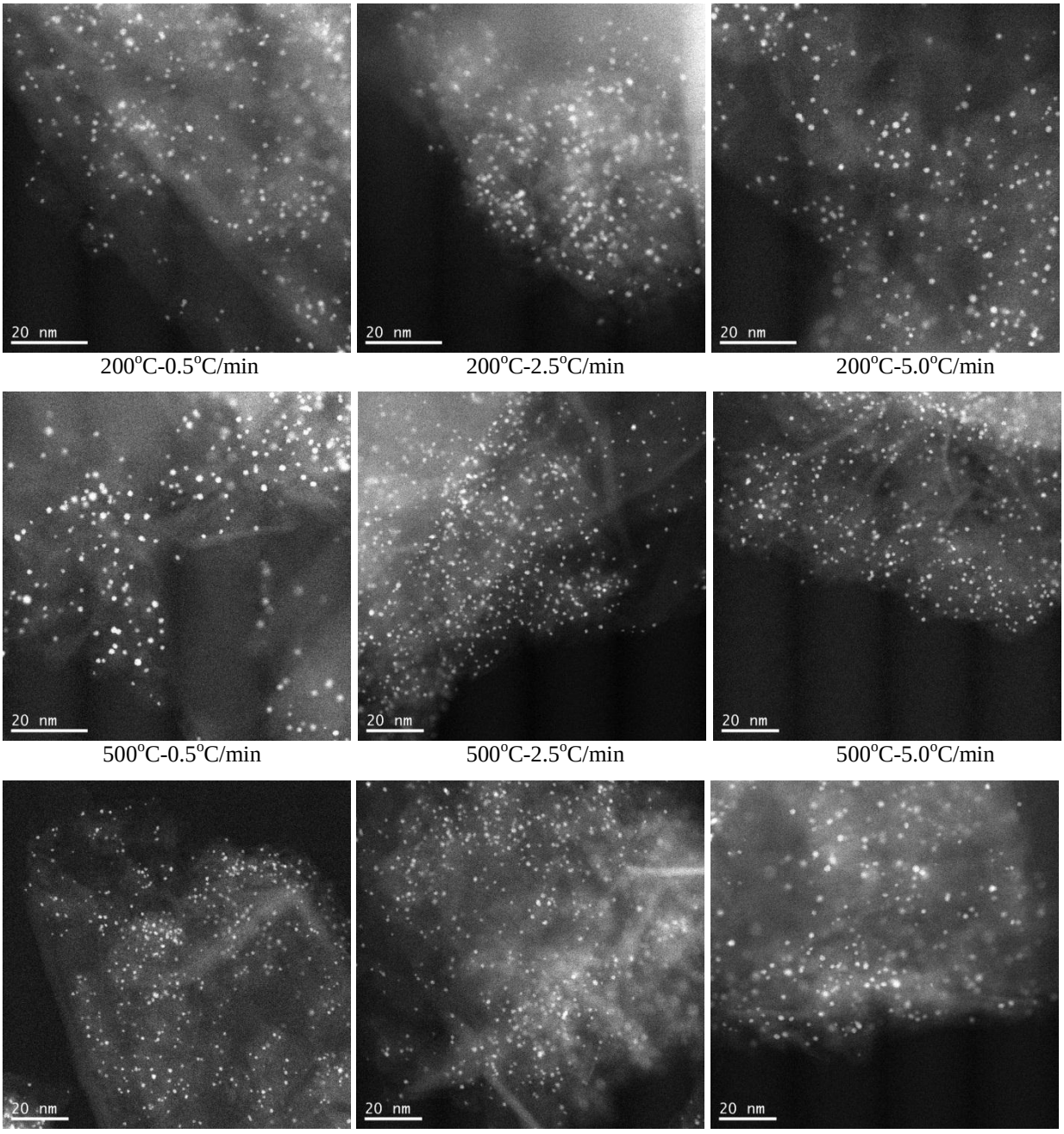

Figure A.9 STEM image examples for HSAG300-PTA-SEA catalysts.

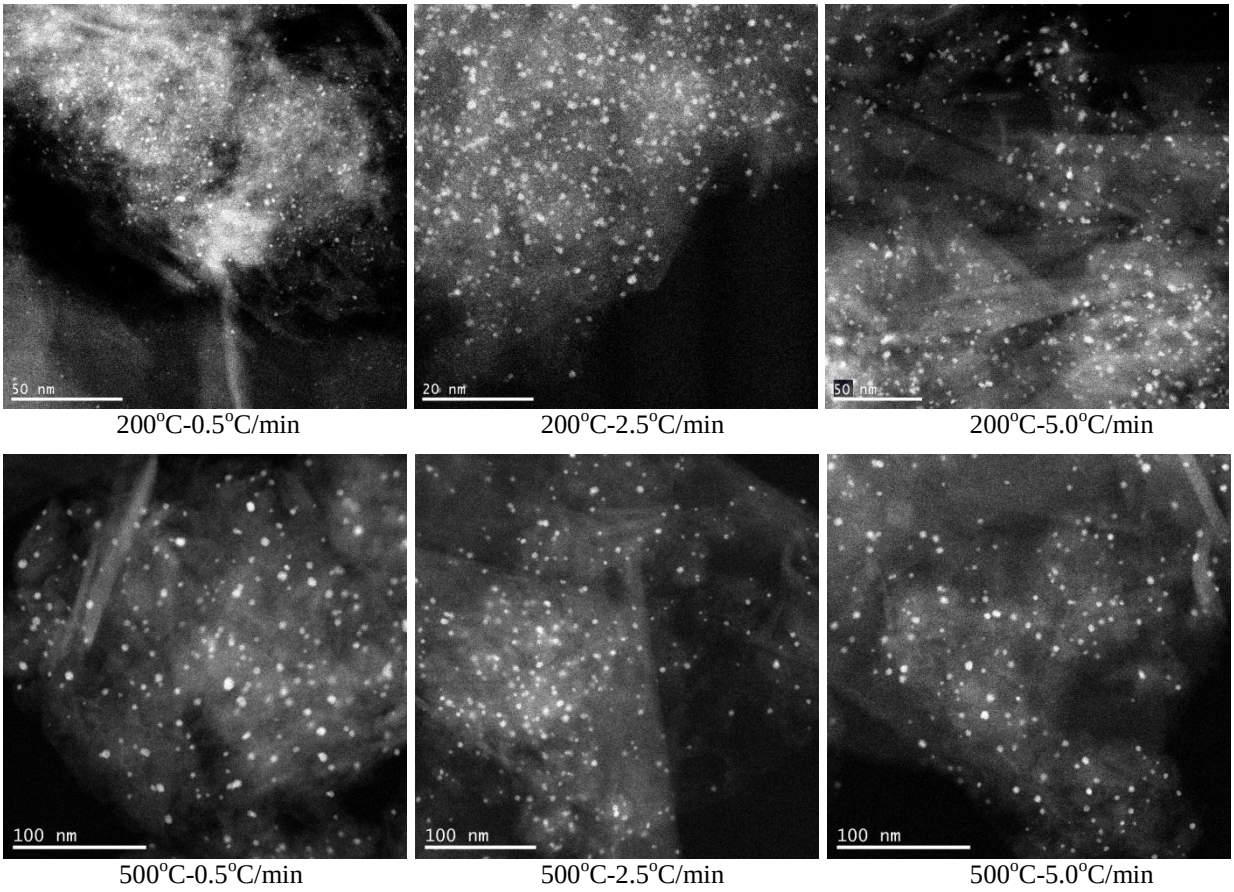

200°C-0.5°C/min | 200°C-2.5°C/min | 200°C-5.0°C/min

500°C-0.5°C/min | 500°C-2.5°C/min | 500°C-5.0°C/min

Figure A.10 STEM image examples for HSAG300-PdTA-SEA catalysts.

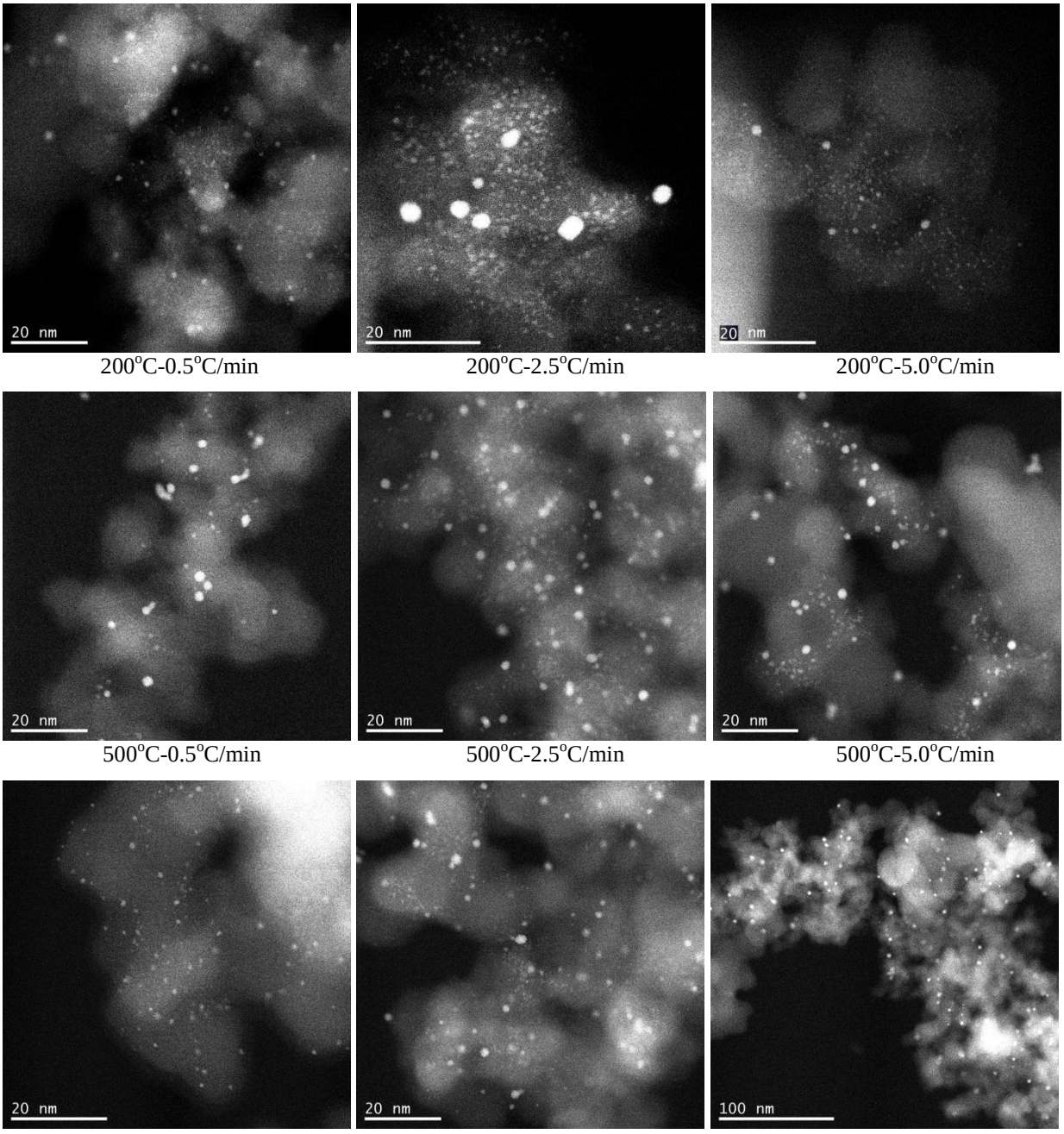

200°C-0.5°C/min | 200°C-2.5°C/min | 200°C-5.0°C/min

500°C-0.5°C/min | 500°C-2.5°C/min | 500°C-5.0°C/min

150He | ice | water

Figure A.11 STEM image examples for SiO2-PTA-SEA catalysts.

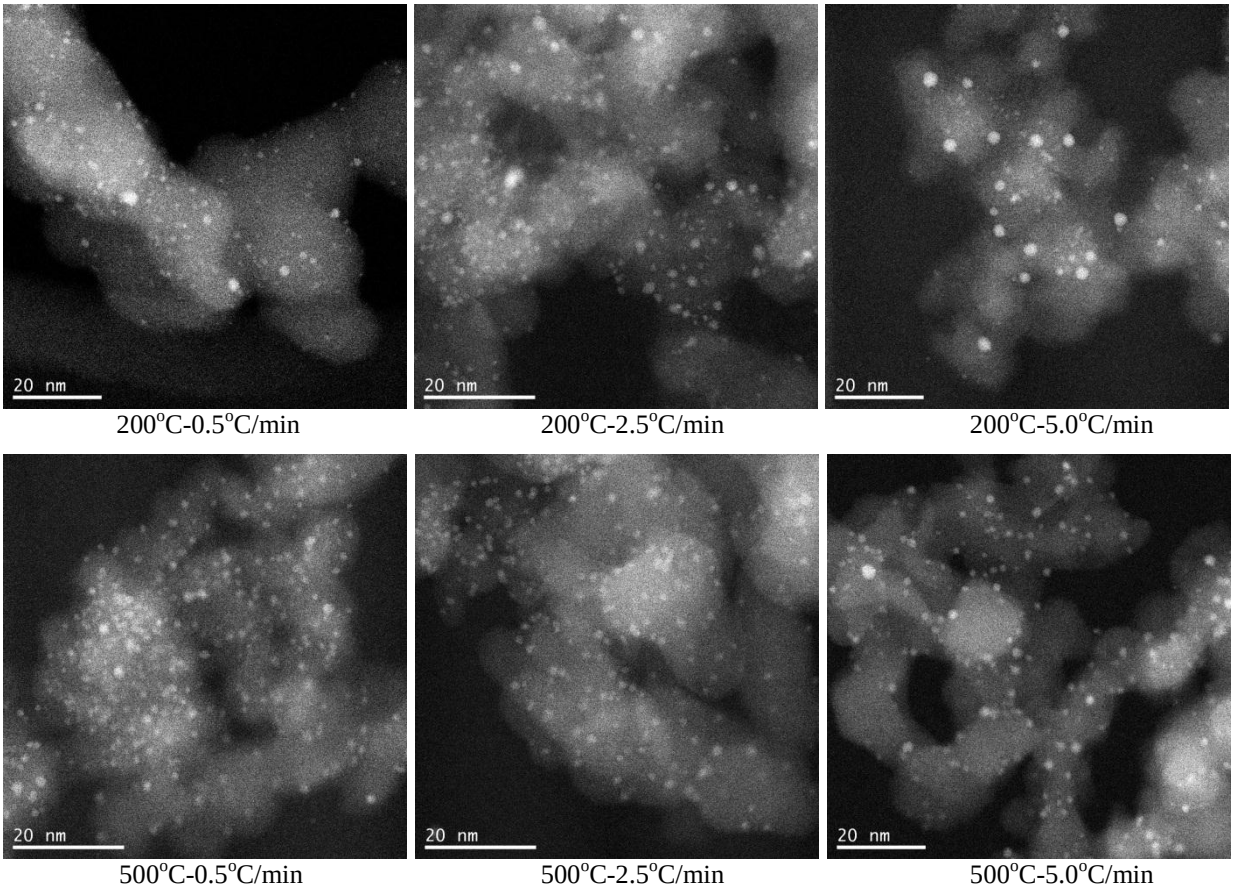

200°C-0.5°C/min | 200°C-2.5°C/min | 200°C-5.0°C/min

500°C-0.5°C/min | 500°C-2.5°C/min | 500°C-5.0°C/min

Figure A.12 STEM image examples for SiO2-PdTA-SEA catalysts.

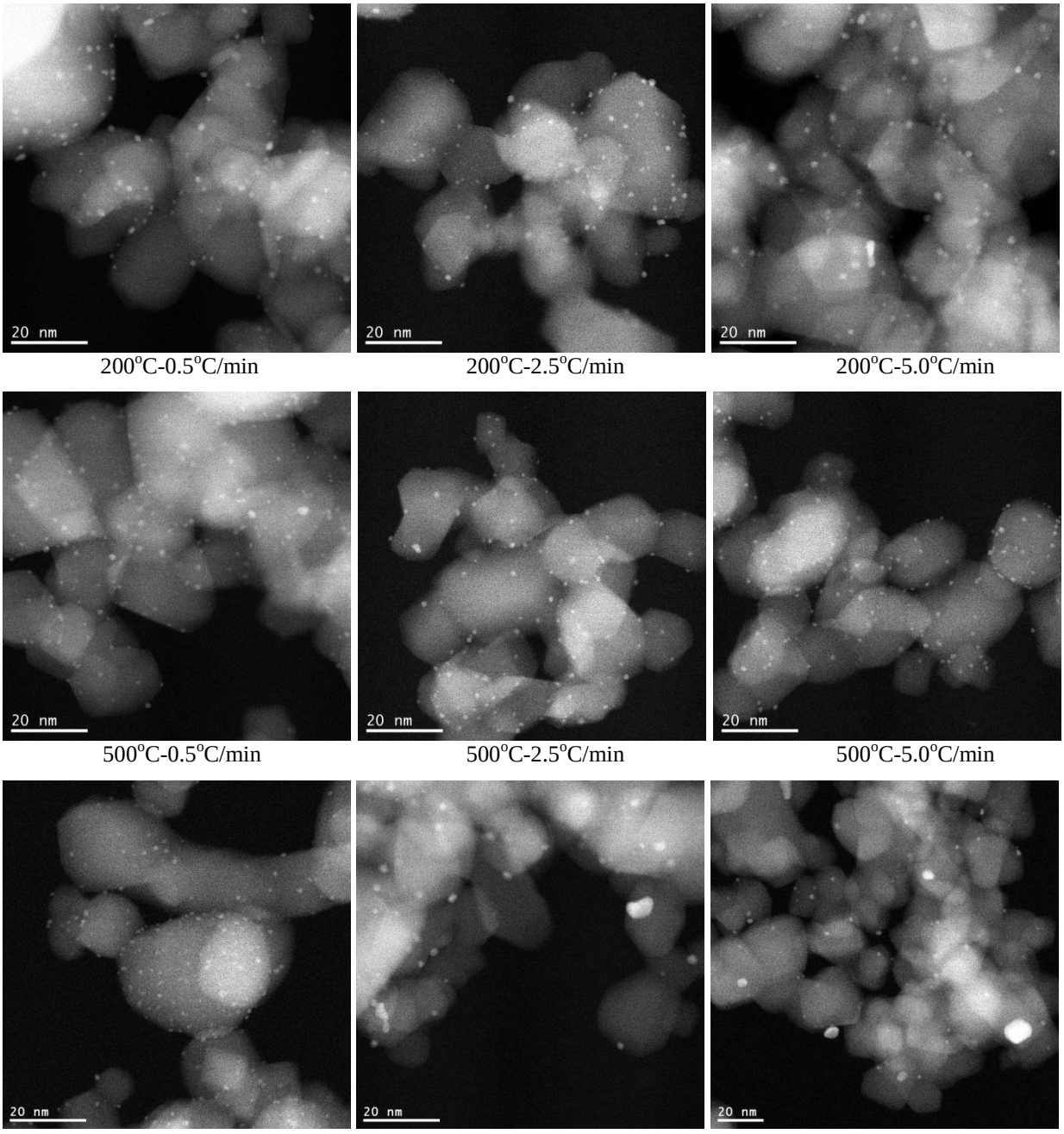

Figure A.13 STEM image examples for TiO2-PTA-SEA catalysts.

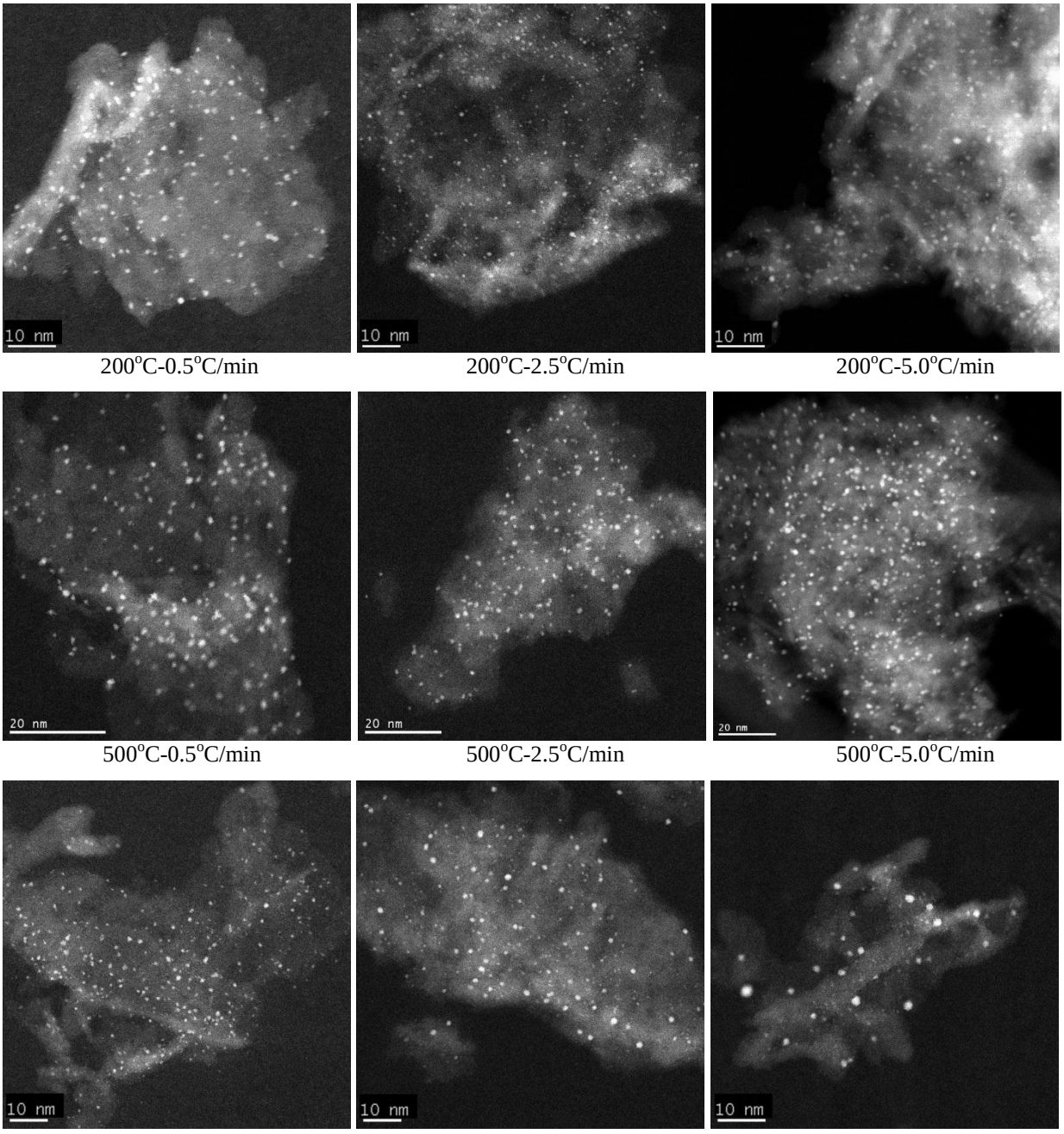

Figure A.14 STEM image examples for Al2O3-CPA-SEA catalysts.

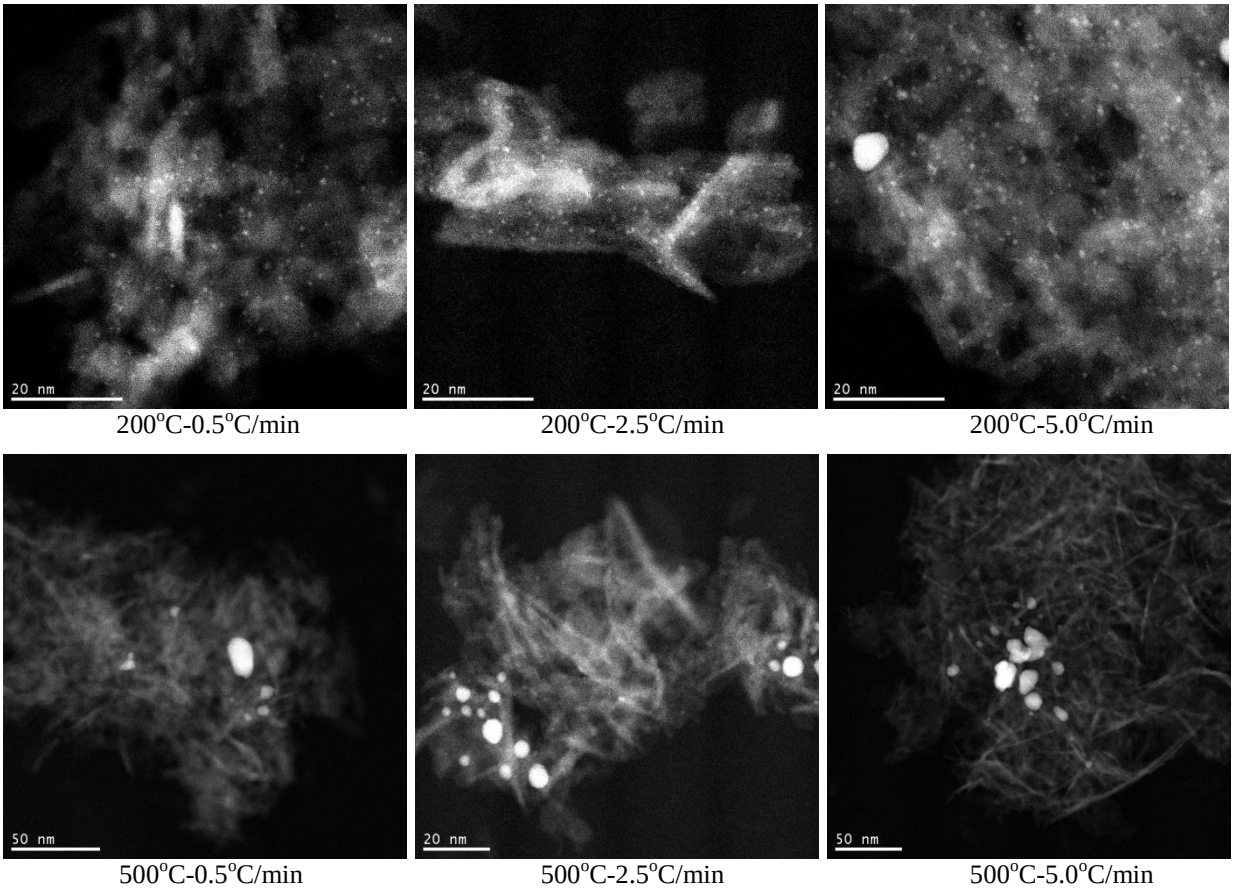

Figure A.15 STEM image examples for Al2O3-PdTC-SEA catalysts.

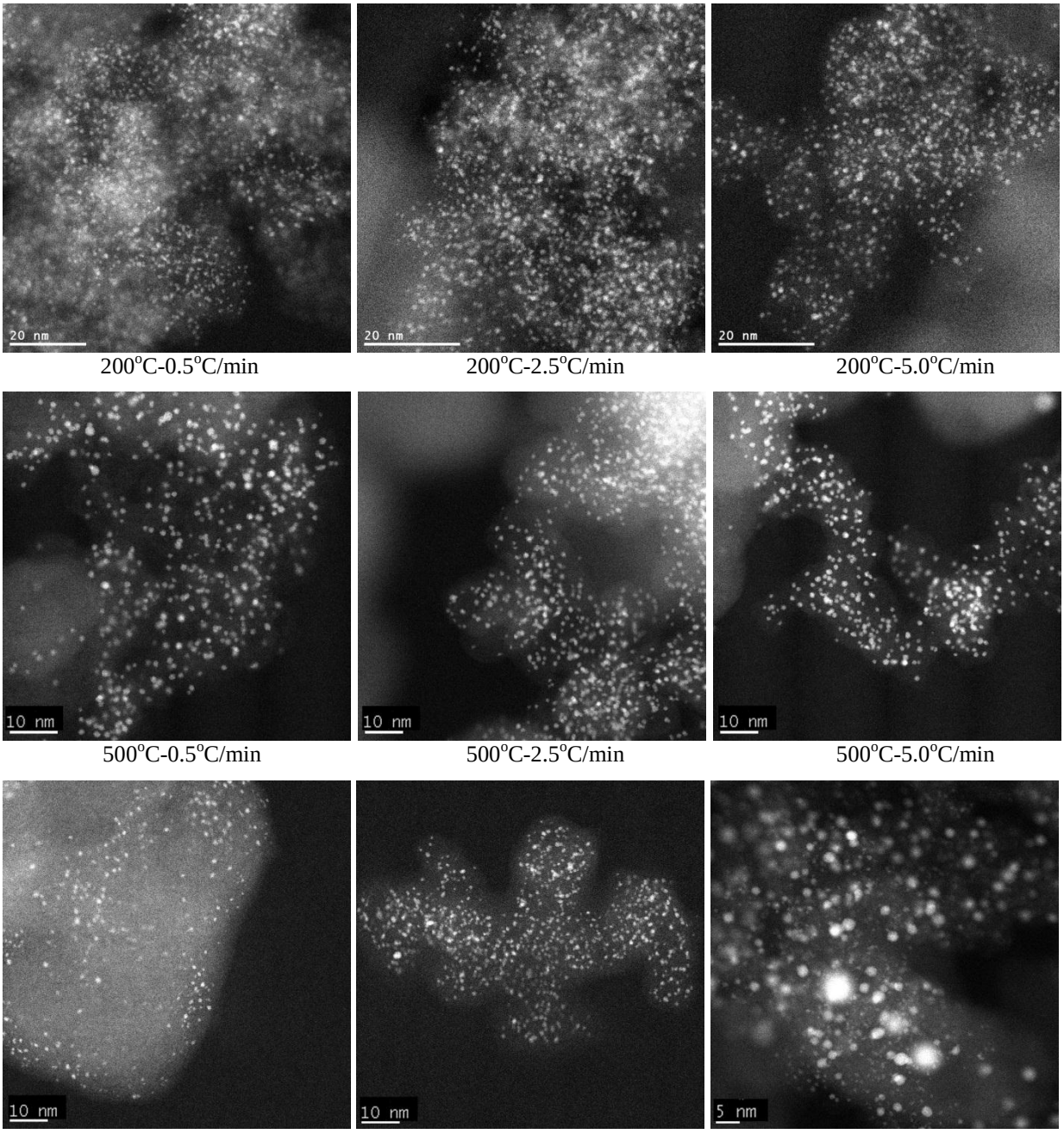

Figure A.16 STEM image examples for XC72-CPA-SEA catalysts.

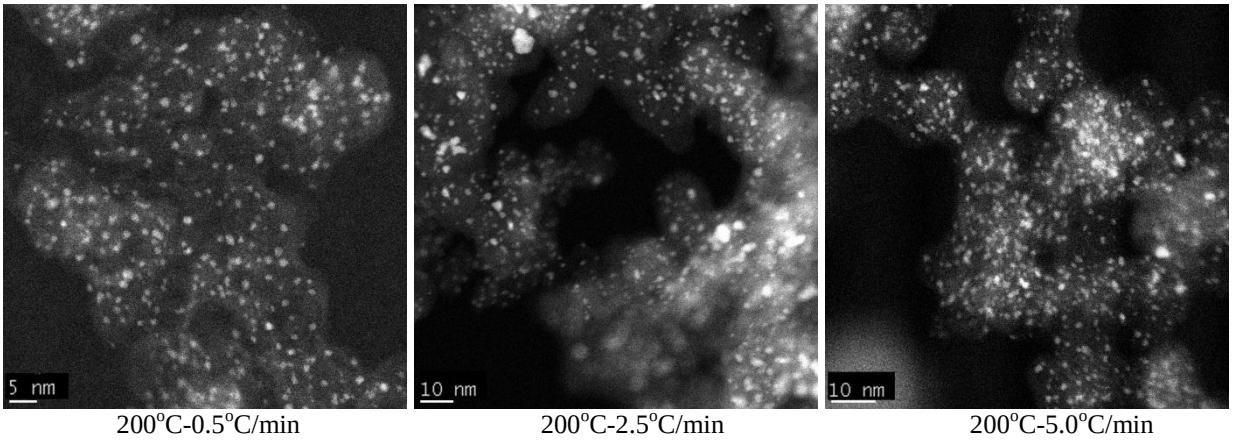

200°C-0.5°C/min | 200°C-2.5°C/min | 200°C-5.0°C/min

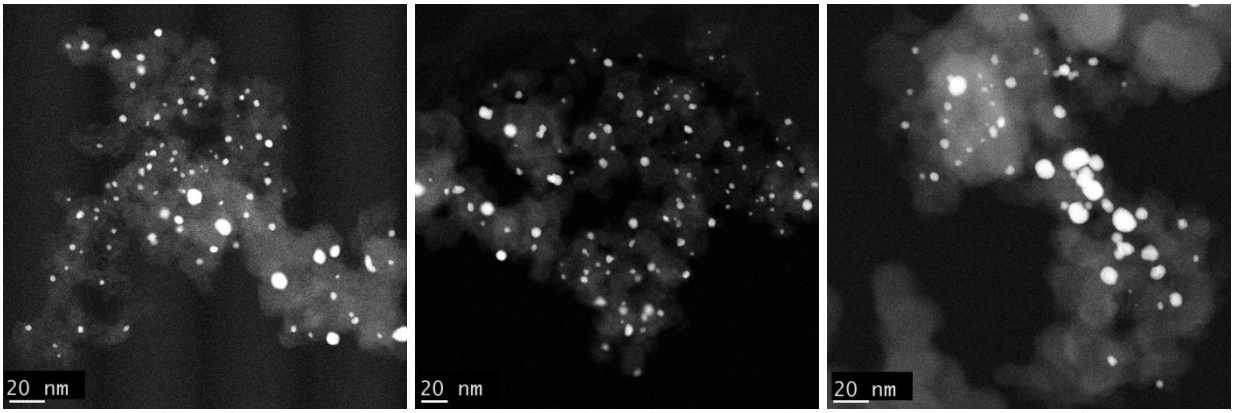

500°C-0.5°C/min | 500°C-2.5°C/min | 500°C-5.0°C/min

Figure A.17 STEM image examples for XC72-PdTC-SEA catalysts.

VITA

Manuel A. Nieto

6201 N Kenmore Ave. Apt 412 Phone: 312-813-8136
Chicago, IL 60660 Email: manuelnieto99@hotmail.com

Education

B.S. Chemical Engineering, 2006
- Minor in Chemistry.

University of Houston.
Houston, TX.

M.S. Chemical Engineering, 2012
University of Illinois at Chicago
Chicago, IL.

Skills

Design:	MATLAB, CHEMCAD, LABVIEW, STATGRAPHICS, X-Rite Color Formulation.
Programming:	FORTRAN 2003.
Analysis:	X-ray Diffraction, Scanning Transmission Electron Microscopy, Inductively Coupled Plasma Spectroscopy, Temperature Programmed Reduction, Surface Area and Porosity, Chemisorption.
Quality Control:	ISO 9001:2008 Quality Management Certified Auditor.

Research

- **University of Illinois at Chicago**, August 2010 – June 2012
  Department of Chemical Engineering
  Disstertation: The Effect of Pretreatment on Metal Dispersion on Carbon and Oxide Supported Catalysts.

Internships

Quimica Comercial Cia. Ltda. Quito, Ecuador.
Summer 2004.
Summer 2005.
- Worked in Product Research and Development division in elaboration of new products such as: cosmetics, anti-foam agents, acrylic resins, polymer coatings, silicones, and fragrances.

Employment

Quimica Comercial Cia. Ltda. Quito, Ecuador.
Position: Production Manager
August 2006 – August 2010.

- Directly involved in the construction and setup of a Masterbatch (polymer pigment concentrates) production plant in 2006.
- Responsible for: complete planning and operation of all Masterbatch productions, laboratory color matching and spectrophotometer measurements, product research and development, raw materials testing, inventory keep-up, final product costing, machinery maintenance, and attendance control of all production plant employees.
- Participated in the development of all operation and security procedures and quality control methods and standards in accordance with the ISO 9001:2008 quality management system.
- Designed and implemented a waste-water treatment and recycling system compliant with all local environmental protection laws and standards.

Training

X-RiteColor Formulation.
X-Rite. Grandville, MI.
October 9-12, 2006.

- Learned all principles of color theory, color formulation, color matching, and spectrophotometer operation focused to polymer pigmentation.

Twin Screw Extrusion Workshop.
American Leistritz Extruder Corp. Somerville, NJ.
November 29-30, 2006.

- Seminary on general theory and operation of Twin Screw Extruders.

Masterbatch Extrusion Technology.
Arco Colores S.A. de C.V. Mexico City, Mexico.
October 16-26, 2006.

- Two week training on Masterbatch production technology. Training included real time operation, troubleshooting, and quality control testing and standardization.

Conferences

Catalysis Club of Chicago Spring Symposium (Poster), Chicago, IL, May 2011.

Memberships

North American Catalysis Society (NACS)/Catalysis Club of Chicago (CCC).